Enzymatic Fischer-Tropsch-Type Reactions

Yilin Hu,[1,*] Chi Chung Lee,[1] Mario Grosch,[1] Joseph B. Solomon,[2] Wolfgang Weigand,[3] Markus W. Ribbe[1,2*]

[1] Department of Molecular Biology and Biochemistry, University of California, Irvine, Irvine 92697-3900, USA

[2] Department of Chemistry, University of California, Irvine, CA 92697-2025, USA

[3] Institute of Inorganic and Analytical Chemistry, Friedrich Schiller University Jena, 07743 Jena, Germany

* To whom correspondence should be addressed: yilinh@uci.edu; mribbe@uci.edu

Abstract

The Fischer-Tropsch (FT) process converts a mixture of CO and H_2 into liquid hydrocarbons as a major component of the gas-to-liquid technology for the production of synthetic fuels. Contrary to the energy-demanding chemical FT process, the enzymatic FT-type reactions catalyzed by nitrogenase enzymes, their metalloclusters and synthetic mimics utilize H^+ and e^- as the reducing equivalents to reduce CO, CO_2 and CN^- into hydrocarbons under ambient conditions. The C_1 chemistry exemplified by these FT-type reactions is underscored by the structural and electronic properties of the nitrogenase-associated metallocenters, and recent studies have pointed to the potential relevance of this reactivity to nitrogenase mechanism, prebiotic chemistry and biotechnological applications. This review will provide an overview of the features of nitrogenase enzymes and associated metalloclusters, followed by a detailed discussion of the activities of various nitrogenase-derived FT systems and plausible mechanisms of the enzymatic FT reactions, highlighting the versatility of this unique reactivity while providing perspectives onto its mechanistic, evolutionary and biotechnological implications.

Contents

1. Introduction

1.1. Fischer-Tropsch process

The Fischer-Tropsch (FT) process converts syngas, or a mixture of carbon monoxide (CO) and hydrogen (H_2), into liquid hydrocarbons at a few hundred degrees Celsius (150-300^oC) and under atmospheric pressure or above (one to several tens of atmospheres). Developed by German chemists Franz Fischer and Hans Tropsch in the 1920s, the FT process is a key component of gas-to-liquid technology for the production of synthetic lubrication oil and synthetic fuels, including natural gas, biomass or coal.

The FT process employs a variety of catalysts to hydrogenate CO into hydrocarbons of varying lengths in a multi-step reaction. The most common catalysts for the FT process are transition metals, such as Co, Fe, Ru and Ni.[1-3] Conversion of CO to hydrocarbons takes place on the surface of these catalysts, proceeding through hydrogenation of CO, hydrogenolysis of the C–O bond, and formation of C–C bonds in a reaction (equation 1) [1-3] usually depicted as follows:

$$(2n + 1)\ H_2 + n\ CO \rightarrow C_nH_{(2n+2)} + n\ H_2O \qquad (1)$$

where n = integer

Depending on the type of catalyst, the temperature and other reaction parameters, hydrocarbons ranging from methane (n=1) to alkanes of higher molecular weight (n=10-20) can be generated through the FT process, although methane is an unwanted byproduct in most gas-to-liquid applications of FT synthesis. Competing reactions also yield small quantities of alkenes, as well as low-molecular-weight oxygenates like alcohols and organic acids.

While the FT process mainly uses CO as the C_1 substrate, it can also convert CO_2 as an atypical substrate to hydrocarbons in an analogous series of reactions.[4,5] Substitution of the typical CO/H_2 feedstock with a CO_2/H_2 mixture in the FT process results in the formation of gaseous C_1-C_4 hydrocarbons.[3] However, longer-chain hydrocarbons are not produced in this reaction, consistent with the additional steps required to convert the more oxidized CO_2 molecule to hydrocarbons via hydrogenation. Complicating matters further is the water-gas-shift (WGS) reaction (equation 2), a prominent side reaction of the FT process, particularly when the reaction is catalyzed by Fe catalysts:

$$CO + H_2O \rightleftharpoons H_2 + CO_2 \quad (2)$$

Additionally, CO and CO_2 compete for absorption by catalysts, which reduces the selectivity of products generated by the FT process.

Regardless, the unique C_1 chemistry with both CO and CO_2 has gained importance over the years for the FT process as an alternative means for the production of low-sulfur diesel fuels. Recently, this process has received renewed attention as an effective, carbon-neutral method to recycle CO (a toxic pollutant) and CO_2 (a greenhouse gas) into liquid hydrocarbon fuels, which could simultaneously combat the environmental impact of these one-carbon compounds and the supply shortage in petroleum-derived hydrocarbons. Optimization of the FT process has focused on improving the thermal efficiency and reducing the costs of syngas production, with cellulosic biomass explored in the recent years as carbon sources for the thermal production of syngas to produce second-generation biofuels in a so-called biomass-to-liquid (BTL) process. In the meantime, alternative strategies are sought to allow conversion of C_1 substrates to hydrocarbons under ambient conditions and thereby mitigate the high energy expenditure of the chemical FT process.

1.2. Enzymatic Fischer-Tropsch-type reactions

One alternative approach to the activation and reduction of C_1 substrates relies on identifying enzyme systems capable of such chemical transformations, as the enzymatic processes can occur in water at ambient temperatures and pressures.[6] Nature has devised a variety of strategies to activate and reduce CO_2, the atypical substrate for the FT process, to fulfill various biological functions. Perhaps the best-known example in this genre is the transformation of atmospheric CO_2 into a biologically useful carbon source by ribulose-1,5-bisphosphate carboxylase/oxygenase (RuBisco), a key enzyme in the Calvin-Benson cycle.[7] Additionally, carbon monoxide dehydrogenase (CODH),[8-13] another enzyme involved in carbon fixation, is known for its ability to catalyze the interconversion of CO_2 and CO; whereas formate dehydrogenase, a key enzyme in the anaerobic respiration, can catalyze the reversible conversion between CO_2 and formate ($HCOO^-$).[14] Interestingly, most of these enzymes employ transition metals, including Fe, Ni, Mo and W, at their active sites to enable the multielectron transformations of the C_1 substrates at ambient conditions. Yet, none of these transformations involve more than two electrons and,

consequently, they do not generate hydrocarbons as further reduced products of CO_2. Additionally, the ability to convert CO to hydrocarbons had not been associated with any enzyme until such a reactivity was discovered in nitrogenase about a decade ago.

The enzymatic FT-type reactivity was first reported for the 'alternative' V-nitrogenase from a diazotrophic microorganism, *Azotobacter vinelandii*, in 2011.[15] The initial report described the ability of the V-nitrogenase to reduce CO to C_1-C_3 hydrocarbons at ambient conditions. This finding was surprising as CO had long been considered an inhibitor for the reactions catalyzed by nitrogenase, yet the V-nitrogenase was shown to reduce CO to hydrocarbons in an ambient, ATP-dependent reaction, using protons (H^+)/electrons (e^-) instead of H_2 as the reducing agent.[15,16] Subsequently, it was demonstrated that the product profile of the V-nitrogenase could be expanded to include C_4 hydrocarbons upon a scale-up of the reaction and that the 'conventional' Mo-nitrogenase, like its V-counterpart, was also capable of converting CO to hydrocarbons, albeit at a much lower efficiency;[17] further, it was illustrated that an *A. vinelandii* culture expressing the V-nitrogenase could also convert CO to hydrocarbons,[18] a feature adapted later for the continuous production of C_2H_4 from the reduction of CO by the whole cells of *A. vinelandii*.[19] Other than the complete nitrogenase enzyme, each of the two components of nitrogenase,[20-24] as well as the cofactors extracted from these components,[25-27] were shown to support the ATP-independent reduction of CO, CO_2 and CN^- to C_1-C_7 hydrocarbons in the presence of artificial electron donors. In addition, the V-nitrogenase was adapted for the electrocatalytic reduction of the atypical FT substrate, CO_2, to C_1-C_3 hydrocarbons;[28] and the whole cells of *Rhodopseudomonas palustris*, a phototrophic microorganism expressing both V- and Fe-only nitrogenases, was shown to reduce CO_2 to CH_4.[29]

The discovery of nitrogenase-based FT-type reactivity is exciting, as it provides an alternative route to the conversion of C_1 substrates into high-value hydrocarbon products in H_2O-based, enzymatic reactions, where hydrogenation of the C_1 substrate is facilitated by H^+/e^- under ambient conditions.[30] Interestingly, reduction of dinitrogen (N_2) to ammonia (NH_3)—the typical reaction catalyzed by nitrogenase[31-34]—mirrors the Haber-Bosch (HB) process that is used for the industrial production of ammonia.[35,36] However, unlike the HB process that combines N_2 and H_2 into NH_3 at high temperatures and pressures, the nitrogenase-catalyzed, HB-type reaction combines N_2 with

H^+/e^- to produce NH_3 and H_2 under ambient conditions (equation 3), much like what occurs in the nitrogenase-catalyzed, FT-type reaction.

$$N_2 + 8H^+ + 8e^- + 16\ MgATP \rightarrow 2NH_3 + H_2 \qquad (3)$$

This review will provide an overview of three homologous nitrogenase enzymes and their associated metalloclusters, followed by a discussion of the reactivities of various nitrogenase-derived FT-type systems, as well as the biochemical, spectroscopic, and structural studies that provide mechanistic insights into the enzymatic FT-type reaction by nitrogenase. The final sections will examine the plausible evolutionary relevance of the ability of nitrogenase to reduce C_1 substrates and the possibility to develop future applications on the basis of the enzymatic FT-type reactivity.

2. Nitrogenase enzymes and their associated metalloclusters

Three homologous nitrogenase enzymes have been identified to date.[31-34,37-43] Designated Mo, V and Fe-only nitrogenases, the three variants are structurally similar and distinguished mainly by the presence (Mo, V) or absence (Fe only) of a heterometal at their active site cofactors. All three nitrogenases consist of two components: a reductase component (collectively termed the Fe protein) and a catalytic component (designated the MoFe, VFe or FeFe protein). Moreover, they adopt the same mode-of-action during catalysis. All of them form a complex between the reductase component and the catalytic component to enable ATP-dependent electron transfer from the $[Fe_4S_4]$ cluster of the former, via a so-called P-cluster, to the cofactor of the latter (designated the M-, V- or Fe-cluster), where substrate reduction occurs upon accumulation of a sufficient number of electrons. These homologous nitrogenase systems will be discussed in detail in this section.

2.1. Mo-nitrogenase

2.1.1. Fe protein (NifH)

Encoded by the *nifH* gene, the Fe protein (or NifH) of Mo-nitrogenase is a homodimer of ~60 kDa. Crystallographic analysis reveals that the NifH protein from *A. vinelandii* (designated *Av*NifH) has each of its subunits folded as a single α/β-type domain (**Figure 1A**), and, together, the two subunits ligate a $[Fe_4S_4]$ cluster at the subunit interface by four Cys ligands, two from each subunit (Cys^{97} and Cys^{132}) (**Figure 1B**)[44,45] Additionally, each subunit contains a nucleotide-

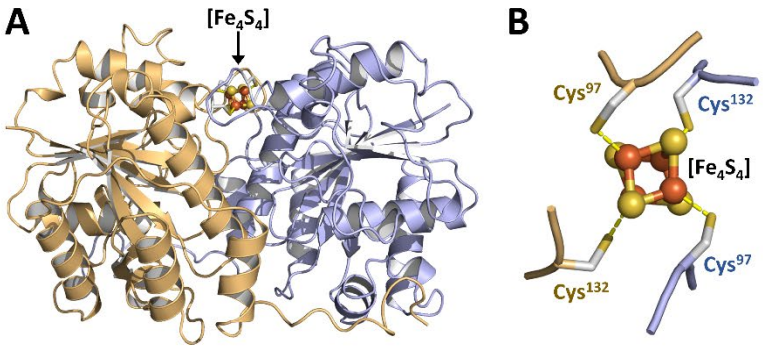

Figure 1. The Fe protein of the Mo-nitrogenase. Crystal structures of (A) the homodimeric Fe protein of *A. vinelandii* Mo-nitrogenase (*Av*NifH) in the nucleotide-free state (PDB entry 2NIP) and (B) its associated [Fe_4S_4] cluster, along with the ligands coordinating the cluster. The two subunits of *Av*NifH are shown as ribbons and colored light yellow and light blue, respectively (A). The ligands of the cluster are presented as sticks, and the cluster is shown in ball-and-stick presentation, with the atoms colored as follows: Fe, orange; S, yellow (B).

binding site ~20 Å away from the [Fe_4S_4] cluster, which comprises a Walker's motif A formed by residues 9-16.[44,46] In the presence of MgATP, the EPR spectrum of NifH broadens[22,31] concomitant with an increased accessibility of the Fe atoms of the [Fe_4S_4] cluster of NifH to chelators (*e.g.*, 2,2'-bipyridine and bathophenanthroline disulfonate),[47-49] indicative of a change in the conformation of NifH upon MgATP binding. Consistent with this suggestion, small angle scattering experiments demonstrate a structural change of the MgATP-bound NifH relative to its MgADP-bound or nucleotide-free counterparts.[50] The crystal structure of a catalytically relevant, MgATP-bound conformation of NifH, on the other hand, is yet to be obtained, largely due to the instability of the crystals in the presence of MgATP. What is available, however, is the crystal structure of a MgADP-bound conformation of wildtype NifH,[45,51] as well as that of a MgATP-bound, ΔLue127 variant of *Av*NifH that is incapable of hydrolyzing ATP,[52] with both showing little structural change compared to the nucleotide-free NifH. Despite the lack of crystallographic data on the binding of MgATP, combined biochemical and SAXS studies point strongly to a long-distance signal transduction between the nucleotide-binding site and the [Fe_4S_4] cluster of NifH, which is likely required for this protein to carry out its function during nitrogenase catalysis.

The capacity of NifH as an efficient electron donor for its catalytic partner is underscored by the versatile redox properties of its [Fe_4S_4] cluster. Unlike most [Fe_4S_4] clusters that adopt only two

oxidation states to enable redox conversions, the [Fe4S4] cluster of NifH is capable of adopting three oxidation states: the oxidized state ($[Fe_4S_4]^{2+}$), the reduced state ($[Fe_4S_4]^{+}$), and the super-reduced, all-ferrous state ($[Fe_4S_4]^{0}$).[31,53-56] The oxidized, $[Fe_4S_4]^{2+}$ state is EPR silent (**Figure 2A**) and determined by Mössbauer spectroscopy as a diamagnetic species with an $S = 0$ ground spin state.[53] In comparison, the reduced, $[Fe_4S_4]^{1+}$ state consists of a mixture of rhombic $S = 1/2$ (g = 2.05, 1.94, 1.88) and axial $S = 3/2$ (g = 5.80, 5.15) species (**Figure 2A**),[53,56] and the distribution of the two species can be altered by additives or solvents, such as urea and glycerol,[53] which shift the

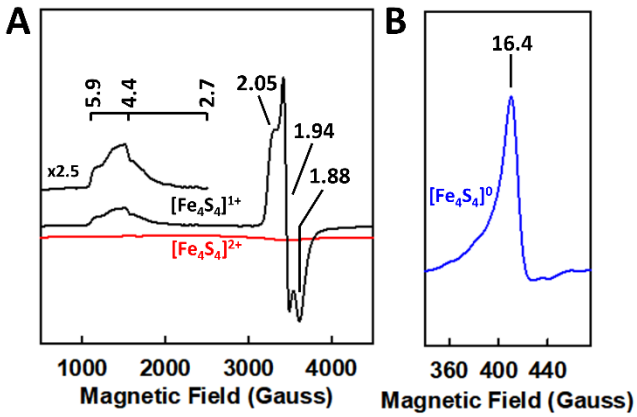

Figure 2. The three oxidation states adopted by NifH. (A) Perpendicular-mode EPR spectra of the reduced ($[Fe_4S_4]^{1+}$) and oxidized ($[Fe_4S_4]^{2+}$) states of *Av*NifH. (B) Parallel-mode EPR spectra of the super-reduced, all-ferrous ($[Fe_4S_4]^{2+}$) state of *Av*NifH. The g values are indicated (in A, B) and the $S = 3/2$ signal of the $[Fe_4S_4]^{1+}$ cluster is enlarged in the inset (in A).

mixture toward the $S = 3/2$ and $S = 1/2$ species, respectively. In the *in vitro* assays, the oxidized $[Fe_4S_4]^{2+}$ and reduced $[Fe_4S_4]^{1+}$ states of NifH can be generated by treating the protein with redox-active dyes (*e.g.*, indigo disulfonate or methyl viologen) and reducing agents (*e.g.*, dithionite), respectively.[31] Perhaps more relevantly, NifH is believed to utilize the $[Fe_4S_4]^{2+/1+}$ redox couple under *in vivo* conditions to perform successive one-electron transfer steps to its catalytic partner during catalysis, with ferredoxins and/or flavodoxins serving as its physiological electron donor in the cell.[57-59] Potentiometric titration experiments have assigned the midpoint potential (E_m) of the $[Fe_4S_4]^{2+/1+}$ redox couple of *Av*NifH as –300 mV *vs.* SHE (standard hydrogen electrode) at pH 8, and binding of MgATP and MgADP have been shown to lower the E_m value of this redox couple by more than 100 mV to –430 mV and –440 mV *vs.* SHE, respectively.[60,61] Similar values have also been reported for the NifH protein from *A. chroococcum* (designated *Ac*NifH), with an E_m of

–450 mV *vs.* NHE (normal hydrogen electrode) assigned to its $[Fe_4S_4]^{2+/1+}$ redox couple upon binding of MgADP. The midpoint potentials of the $[Fe_4S_4]^{2+/1+}$ redox couple are readily achievable under physiological conditions, supporting the notion that NifH uses this redox couple to mediate a one-electron transfer during catalysis. However, the question of whether NifH to mediate a two-electron transfer event was raised when it was discovered that NifH was also capable of adopting the super-reduced, all-ferrous $[Fe_4S_4]^0$ state.[54,55,62-64]

With all its Fe atoms present in the +2-oxidation state, the all-ferrous $[Fe_4S_4]^0$ state of NifH was the first example discovered in this genre. Under *in vitro* conditions, this super-reduced state can be generated upon treatment of NifH with various reductants, yielding two types of all-ferrous species with distinct color hues. One of them, generated with methyl viologen, is characterized by a brown color;[65] the other, generated with stronger reducing agents like Ti(III) citrate, Cr(II) EDTA and Eu(II) chelates [*e.g.*, Eu(II) DTPA, Eu(II) EGTA, Eu(II) DOTAM], is typified by a reddish-pink hue.[54-56,64,66,67] The brown species is EPR-silent and determined by the Evans method as an $S = 0$ ground spin state;[63,65] whereas the pink species shows a characteristic $g = 16.4$ parallel-mode EPR signal (**Figure 2B**) and has been assigned by Mössbauer spectroscopy and DFT calculations as an $S = 4$ ground spin state.[55,68-70] Results from redox titration experiments point to the possibility for both all-ferrous species to exist under *in vivo* conditions: the brown species can be generated for *Av*NifH with flavodoxin hydroquinone (E_m = -515 mV *vs.* NHE), a physiological electron donor;[63] and the reddish-pink species can be generated for an *Av*NifH variant containing a $[Fe_4Se_4]$ cluster (designated *Av*NifH^{Se}) in place of its native $[Fe_4S_4]$ counterpart, as well as the VnfH protein from *M. acetivorans* (designated *Ma*VnfH) (also see section 2.2.1 below), with Eu(II) DOTAM at a solution potential of −0.59 V, which is well within the range of the reduction potentials in the cell.[67] The observation of two different all-ferrous species is intriguing, particularly given that the pink all-ferrous species is achieved at an E_m value that is >300 mV more negative than that used to generate the brown all-ferrous species. One plausible explanation for this phenomenon is that the super-reduced $[Fe_4S_4]^0$ state of NifH comprises a mixture of the brown ($S = 0$) and pink ($S = 4$) species, much like that observed for the reduced, $[Fe_4S_4]^{1+}$ state of NifH, which comprises a mixture of $S = 3/2$ and $S = 1/2$ species. Furthermore, it is possible that only one of the two spin states contributes primarily to the reactivity of the all-ferrous NifH in the cell; however, it is unclear which one is the primary contributor given the easier accessibility but weaker reducing power of the brown species that contrasts the lesser accessibility but stronger reducing power of

the pink species. While this hypothesis is yet to be tested, the scenario of having NifH cycling between the all-ferrous. $[Fe_4S_4]^0$ state and the oxidized, $[Fe_4S_4]^{2+}$ state is significant from the perspective of cellular energy conservation, as it would enable a two-electron transfer event–contrary to a one-electron transfer event supported by the $[Fe_4S_4]^{1+/2+}$ redox couple—upon hydrolysis of two MgATP molecules, thereby reducing the cellular energy consumption by half. Moreover, the all-ferrous state is intimately associated with the activity of C_1 substrate reduction by NifH (see below), although the spin state of the all-ferrous state ($S = 0$ *vs*. $S = 4$) that is responsible for this FT-type reactivity is yet to be conclusively established.

2.1.2. MoFe protein (NifDK)

The MoFe protein (or NifDK) of Mo-nitrogenase is an $\alpha_2\beta_2$-heterotetramer of ~220 kDa, with its α- and β-subunit encoded by the *nifD* and *nifK* gene, respectively.[71,72] Crystallographic analysis reveals that the NifDK protein from *A. vinelandii* (designated *Av*NifDK) adopts a pseudo-twofold axis of symmetry, with two αβ-subunit pairs comprising three domains of alternating α-helices and parallel β-sheets per subunit (**Figure 3A**).[73-75] Each αβ-dimer of NifDK contains a pair of highly

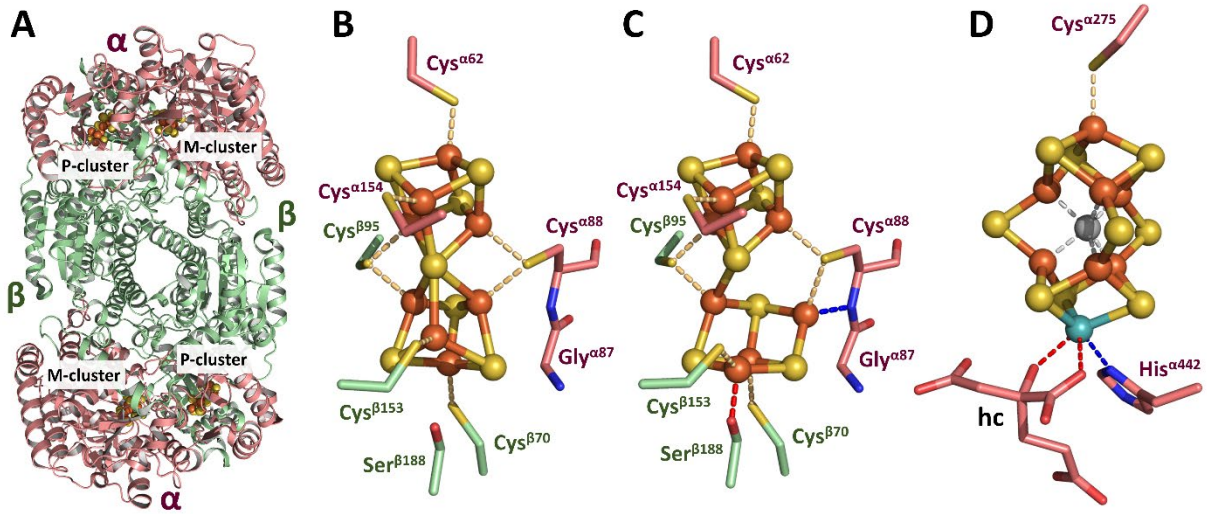

Figure 3. The MoFe protein of the Mo-nitrogenase. Crystal structures of (A) the heterotetrameric MoFe protein from *A. vinelandii* (*Av*NifDK) (PDB entry 3U7Q); (B, C) its P-cluster ($[Fe_8S_7]$) in the reduced, P^N state (B) and the oxidized, P^{OX} (or P^{2+}) state (C); and (D) its M-cluster (or cofactor; [*R*-homocitrate)$MoFe_7S_9C$]) in the reduced, resting-state conformation, along with ligands coordinating the P- and M-clusters (B–D). The α- and β- subunits of *Av*NifDK are shown as ribbons and colored deep salmon and pale green, respectively (A). The ligands of the P- and M-clusters are presented as sticks, and the clusters are shown in ball-and-stick presentation, with the atoms colored as follows: Fe, orange; Mo, cyan; S, yellow; C, light gray (B). hc, homocitrate

complex metalloclusters that have thus far evaded successful chemical synthesis. One of them, termed the P-cluster, is a [Fe_8S_7] that is located at the α/β-subunit interface, ~10 Å beneath the protein surface (**Figure 3B and C**). The other, designated the M-cluster (also known as FeMoco or cofactor), is an [(*R*-homocitrate)-$MoFe_7S_9C$][76,77] cluster that is 'buried' within the α-subunit, ~19 Å beneath the protein surface (**Figure 3D**). During catalysis, NifDK undergoes repeated association and dissociation with its reductase partner NifH, which permits ATP-dependent electron transfer from the [Fe_4S_4] cluster of NifH, through the P-cluster, to the M-cluster, where substrate reduction eventually takes place (**Figure 4**).[78]

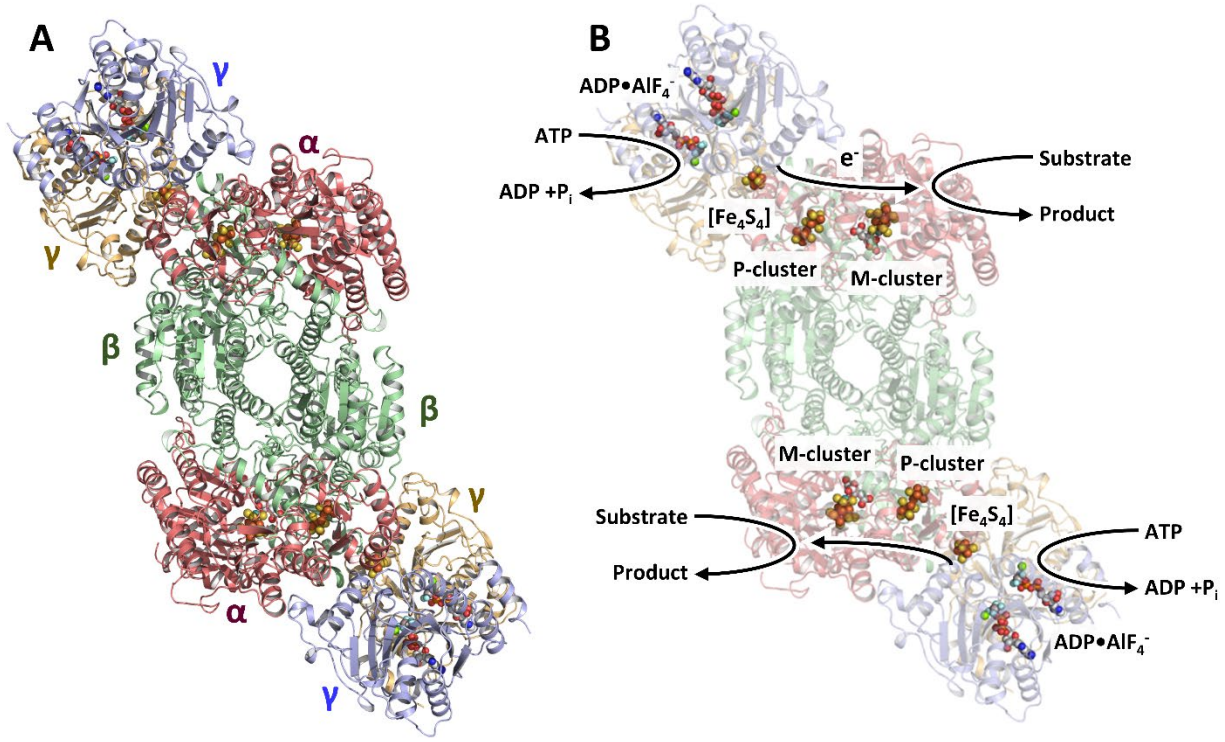

Figure 4. The Mo-nitrogenase complex. (A) Crystal structure of the MgADP•AlF_4^-–stabilized complex that consists of *Av*NifH (γ_2) and *Av*NifDK ($\alpha_2\beta_2$) at a molar ratio of 2:1 (PDB entry 1N2C); and (B) the electron pathway within the *Av*NifH/*Av*NifDK complex that allows electrons to flow from the [Fe_4S_4] cluster of *Av*NifH, via the P-cluster ([Fe_8S_7]), to the M-cluster ([*R*-homocitrate)$MoFe_7S_9C$]) of *Av*NifDK, where substrate reduction occurs. The protein subunits, the clusters and their ligands are presented and colored as those in Figures 1 and 3. MgADP•AlF_4^- is shown in ball-and-stick presentation, with the atoms colored as follows: Mg, green; O, red; C, light gray; N, blue; Al, dark gray; F, light blue; P, dark orange.

2.1.2.1. P-cluster

The P-cluster of the dithionite-reduced, 'resting-state' Mo-nitrogenase is ligated by six Cys residues, three from the α-subunit ($Cys^{\alpha62}$, $Cys^{\alpha88}$, $Cys^{\alpha154}$) and three from the β-subunit ($Cys^{\beta70}$,

$Cys^{\beta 95}$, $Cys^{\beta 153}$), between the α- and β-subunits of NifDK (**Figure 3B**).[73-75,79] Designated P^N, the resting-state P-cluster can be viewed as two [Fe_4S_3] partial cubanes bridged by a μ_6-sulfide. EPR and Mössbauer studies have led to the assignment of P^N as a diamagnetic species with an $S = 0$ spin state, with all of its eight Fe atoms present in the ferrous state.[80,81] The P^N cluster can undergo one- and two-electron oxidation to assume the P^{1+} and P^{2+} (or P^{OX}) state, respectively; additionally, a three-equivalent oxidized form of the P-cluster pair, designated P^{3+}, can be generated upon oxidation with solid thionine.[80,82] However, it is unclear which redox couple of the P-cluster is utilized for catalysis under physiological conditions. There are contradictory assignments of the redox couples of the P-cluster, with a midpoint potential of –307 mV derived from potentiometric titrations of the solution-state NifDK and assigned to the P^{OX}/P^N redox couple,[80] and a somewhat similar value of –230 mV determined by voltammetry experiments of the electrode-attached NifDK and assigned to the P^{1+}/P^N couple.[83] These disparate results in midpoint potential determination, coupled with the question of whether the P-cluster receives one or two electrons from NifH during catalysis (see above), renders the nature of the physiologically relevant oxidation states of the P-cluster elusive.

What is known, however, is that the P^{OX} state can be achieved *in vitro* by treating NifDK with IDS,[84-86] or by allowing the NifDK protein that is isolated and crystallized with dithionite to undergo a slow self-oxidation process in the crystalline state.[87] Recently, the P^{OX} state was also achieved concomitant with binding of N_2 to the cofactor in a NifDK protein species that was directly isolated from an N_2-fixing culture of *A. vinelandii* under anaerobic, but dithionite-free conditions (also see section 4.1.1.3 for more discussion).[88,89] Compared to the P^N state (**Figure 3B**),[73-75] the two-electron oxidized P^{OX} state (**Figure 3C**) undergoes significant structural rearrangements, with two Fe atoms of one of its subcubanes losing ligation to the 'central' sulfide and coordinated respectively by the O^γ atom of $Ser^{\alpha 188}$ and a backbone N atom of $Cys^{\alpha 88}$.[87] Such a structural change upon oxidation, which renders one half of the P^{OX} cluster in a more 'open' conformation, is accompanied by a clear change in the electronic properties of the cluster. EPR and Mossbauer experiments have led to the assignment of an $S = 3$ or 4 spin state to the P^{OX} cluster, which gives rise to a characteristic EPR signal at $g = 11.9$ (**Figure 5A**); moreover, these experiments have established a reversible conversion between the P^{OX} and P^N states upon treatment of NifDK with an oxidant (*e.g.*, IDS) or a reductant (*e.g.*, dithionite).[80,90]

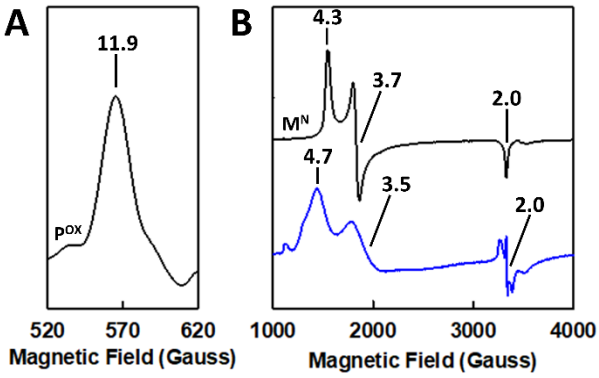

Figure 5. EPR features of the *Av*NifDK-associated clusters. Shown are the characteristic EPR signals of (A) the P^{OX} (or P^{2+}) cluster (parallel mode) and (B) the M^N-cluster in the protein-bound (black) and solvent-extracted (blue) states (perpendicular mode). The *g* values are indicated.

The P^{1+} state can be generated under turnover conditions, by redox titration, and electrochemically.[86,91,92] The spin state of the P^{1+} cluster has been determined by EPR and MCD studies as a mixture of $S = 1/2$ ($g = 2.06, 1.95, 1.81$) and $S = 5/2$ ($g = 6.7, 5.3$, or $g = 7.3$.[81,93] It is interesting to note that an intermediate state of the P-cluster was reported alongside the P^N state based on a crystallographic study of the dithionite-reduced NifDK protein from *Klebsiella pneumoniae*.[94] This so-called $P^{semi\text{-}OX}$ state could be modeled with mixed conformations of P^N and P^{OX}, leading to the proposal that it might represent the structure of the P^{1+} state. Contradictory to this proposal, however, was the observation from MCD studies of *Av*NifDK, which suggested that the P^{1+} species could comprise a $[Fe_4S_4]^{1+}$ cluster pair.[80,95] The structure of the elusive P^{1+} cluster, as well as the relevance of the various oxidation states of the P-cluster to catalysis, requires further investigation.

2.1.2.2. M-cluster

The M-cluster of the dithionite-reduced, 'resting-state' Mo-nitrogenase is coordinated by only two protein ligands from NifDK: $Cys^{\alpha 275}$ and $His^{\alpha 442}$ (**Figure 3D**).[73-77] Designated M^N, the resting-state M-cluster can be viewed as $[MoFe_3S_3]$ and $[Fe_4S_3]$ partial cubanes ligated by three μ_2 'belt' sulfides and a μ_6 interstitial carbide; additionally, its Mo-end is coordinated by the 2-hydroxy and 2-carboxy groups of *R*-homocitrate, an organic moiety that is further ligated by $Lys^{\alpha 426}$.[73-75,96] The M^N state is characterized by a rhombic $S = 3/2$ EPR signal ($g = 4.3, 3.7, 2.0$) (**Figure 5B**),[31,97] and it can undergo one-electron oxidation and reduction, respectively, to yield the M^{OX} and M^N

states.[80,95] EPR studies has assigned this one-electron oxidized state as a diamagnetic species with an $S = 0$ spin state, [80,95] and potentiometric titration experiments have determined the midpoint potentials of the M^{OX}/M^{N} redox couples of the NifDK proteins from *A. vinelandii* (*Av*NifDK), *A. chrococcum* (*Ac*NifDK) and *Rhodobacter capsulatus* (*Rc*NifDK) as –42 mV *vs.* NHE, –42 mV *vs.* NHE and –50 mV *vs*. SHE, respectively.[98,99] The M^{R} state, on the other hand, can be generated under turnover conditions (*i.e.*, in the presence of NifH, MgATP and dithionite), and a midpoint potential of –465 mV *vs*. NHE has been determined for the M^{N}/M^{R} redox couple of *Av*NifDK.[100-102]

Interestingly, a square wave voltammetry study of *Av*NifDK, which was immobilized on a pyrene-modified hydrogel film and directly attached to the electrode, led to the assignment of –590 mV *vs.* NHE to the M^{N}/M^{R} redox couple, a potential much more negative than that determined indirectly with redox mediators for the same protein in the presence of its reductase partner, *Av*NifH.[83] Similarly, it was observed that upon extraction of the M-cluster as an intact entity into an organic solvent (*e.g.*, NMF and DMF), the midpoint potentials of the cofactor became more negative, with values of –320 to –270 mV *vs.* SHE and –1 V *vs.* SHE, respectively, reported for the M^{OX}/M^{N} and M^{N}/M^{R} redox couples.[103-105] Moreover, the change in the potential of the extracted cofactor was shown to be accompanied by a broadening of the cofactor-specific $S = 3/2$ EPR signal (g = 4.7, 3.5, 2.0) (**Figure 5B**).[106,107] Apparently, immobilization of NifDK without NifH on an electrode, or extraction of the cofactor from NifDK into solvents, renders the electronic and redox properties of the M-cluster different than those of its counterpart in the complete nitrogenase system. Nevertheless, both the isolated NifDK protein and the extracted M-cluster are capable of C_1 substrate reduction on their own (see section 3 below), highlighting the catalytic versatility of the various components of nitrogenase.

2.1.3. Mo-nitrogenase complex (NifH/NifDK)

A number of crystal and cryo-EM structures have been obtained for the Mo-nitrogenase complexes from *A. vinelandii*, which were generated by mixing *Av*NifH and *Av*NifDK in the absence of nucleotide or in the presence of MgADP, nonhydrolyzable MgATP analogs (*e.g.*, MgADP· AlF_4^-, MgAMPPCP) or MgATP under turnover conditions (**Figures 4 and 6**).[78,108-110] The complexes generated with MgADP or nonhydrolyzable MgATP analogs (**Figures 4A, 6B and 6C**) contain NifH and NifDK at a molar ratio of 2:1, with one NifH dimer bound to each αβ-dimer

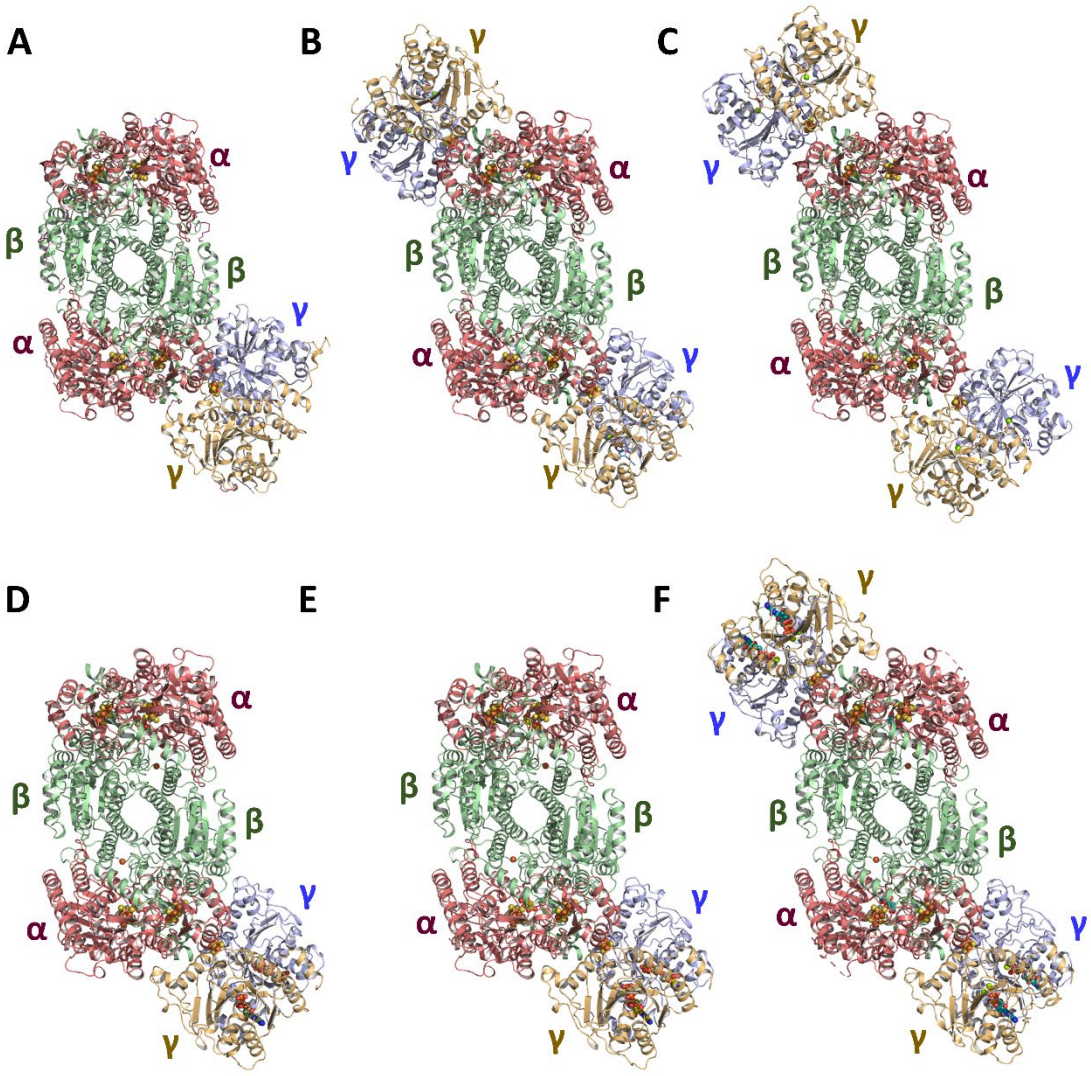

Figure 6. Variations of the composition of the Mo-nitrogenase complex. (A–C) Crystal structures of complexes generated (A) without nucleotide (PDB entry 2AFH); (B) with MgADP (PDB entry 2AFI); and (C) with MgAMPPCP, a non-hydrolyzable ATP analog (PDB entry 2AFK). (D–F) CryoEM structures of (D) TO complex I (PDB entry 7UT8) and (E) TO complex II (PDB entry 7UT9), generated with MgATP; and (F) the complex generated with BeFx, a non-hydrolyzable ATP analog (F). The complexes shown in panels A, D and E consist of *Av*NifH (γ_2) and *Av*NifDK ($\alpha_2\beta_2$) at a molar ratio of 1:1; whereas the complexes shown in panels B, C and F consist of *Av*NifH (γ_2) and *Av*NifDK ($\alpha_2\beta_2$) at a molar ratio of 2:1. The protein subunits, the clusters and their ligands, and nucleotides are presented and colored as those in Figures 1, 3, and 4.

of NifDK;[78,109] whereas those generated without nucleotide (**Figure 6A**)[109] or with MgATP under turnover conditions (**Figure 6D, E**)[110] contain NifH and NifDK at a molar ratio of 1:1.[109,110] Interestingly, while the overall structures of NifH are mostly conserved in the various complexes,

there is a notable movement of the [Fe_4S_4] cluster by ~3 Å toward the surface of the protein, with the cluster located most outwardly and, consequently, in the closest proximity to the P-cluster of NifDK within the complex, in the crystal structures of the 'transition-state' complexes stabilized by MgATP analogs (**Figure 4A and 6C**).[78,109] This observation signifies a conformational change induced by nucleotide binding at a remote site of NifH that relocates its [Fe_4S_4] cluster towards its catalytic partner NifDK to facilitate the interprotein electron transfer between the two proteins during catalysis.

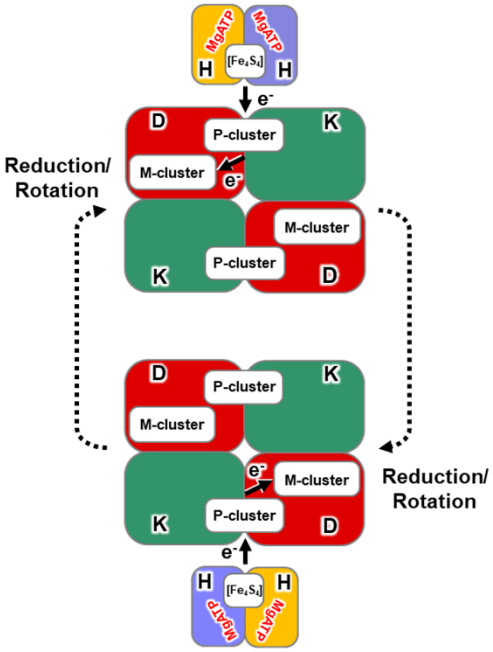

Figure 7. Proposed asynchronous rotation of the two cofactors of *Av*NifDK. The proposed mechanism involves an alternate binding of *Av*NifH to the two αβ-dimers of *Av*NifDK that drives rotation of the M-cluster via ATP-dependent electron transfer from *Av*NifH to one αβ-dimer of *Av*NifDK while allowing the substrate reduction to take place in the other αβ-dimer of *Av*NifDK that is temporarily 'idling' prior to the binding of the next *Av*NifH. Such an asynchronous rotation of the two cofactors allows stepwise reduction of N_2 to occur a step apart in the two αβ-dimers of *Av*NifDK (also see Figure 27).

Recently, a solution-state Mo-nitrogenase complex was generated under turnover conditions and its structure subsequently analyzed by cryo-EM. Contrary to the complexes stabilized by non-hydrolyzable MgATP analogs, this turnover-state complex contains NifH and NifDK at a molar ratio of 1:1 (**Figures 6D and E**).[110] The observation of a 1:1 complex between *Av*NifH and *Av*NifDK is important, as it could reflect the real-time, dynamic interactions between NifH and

NifDK under actual turnover conditions in solutions that have thus-far escaped capture in the crystalline state of the complexes generated with non-hydrolyzable MgATP analogs. Consistent with this observation, a recent crystallographic study has led to the hypothesis of a stepwise reduction of N_2 that occurs via an asynchronous rotation of the two cofactors in NifDK, which is driven by an alternate binding of NifH to the two αβ-halves of this protein (**Figure 7**).[88,89] Such a mode-of-action could account for the cryo-EM observation of a 1:1 complex between NifH and NifDK, particularly given the transient nature and rapid time scale of the alternate interaction between NifH and the two αβ-halves of NifDK; however, further evidence is required to substantiate this hypothesis.

Consistent with the structural observation of the formation of a functional complex between NifH and NifDK during catalysis, combined kinetic, spectroscopic and structural studies of the Mo-nitrogenases have led to the proposal of a mechanistic model of nitrogenase comprising two key components.[31,33,111-116] One component, termed the 'Fe protein cycle' (**Figure 8A**),[31] depicts

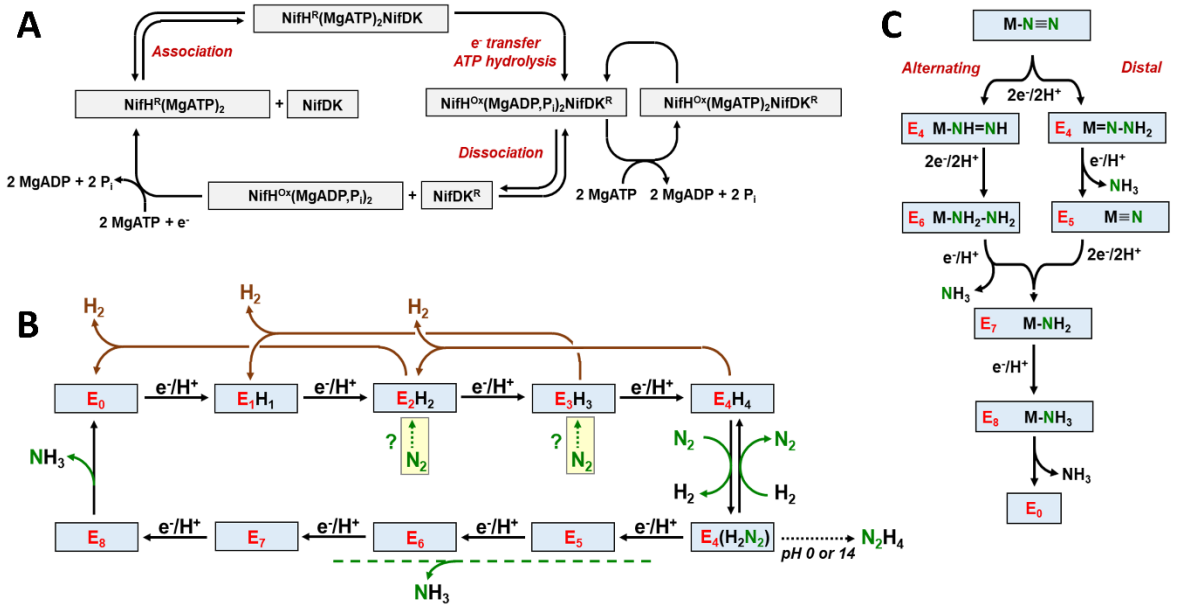

Figure 8. Mechanistic model of the Mo-nitrogenase. Shown are (A) the Fe protein cycle; (B) the MoFe protein cycle (or the Lowe-Thorneley model); and (C) the alternating (left) and distal (right) pathways. $NifH^R$, reduced NifH; $NifH^{Ox}$, oxidized NifH; $NifDK^R$, reduced NifDK

binding of the reduced, MgATP-bound NifH to NifDK, which allows inter-protein electron transfer from the former to the latter concomitant with hydrolysis of MgATP. This step is followed by dissociation of the oxidized, MgADP/P_i-bound NifH from the reduced NifDK, and release of

MgADP and P_i from NifH. Subsequently, NifH is re-reduced and 'loaded' with a 'new' MgATP, which initiates the next round of complex formation and inter-protein electron transfer. The 'Fe protein cycle' must repeat multiple times to enable substrate reduction by NifDK via the 'MoFe protein cycle', the second component of the mechanistic model of nitrogenase. Better known as the Lowe-Thorneley model and updated over the years (**Figure 8B**),[31,33,111,112] the 'MoFe protein cycle' describes the intra-protein delivery of protons and electrons to the M-cluster of NifDK for the binding, activation and reduction of substrate. In this model, each state is designated E_n, where n represents the number of electrons added to one M-cluster in one αβ-dimer of NifDK during catalysis. The resting-state enzyme at the beginning of the catalytic cycle is designated E_0, and stepwise additions of electrons/protons lead to the sequential formation of the E_1–E_4 states with binding of N_2 occurring *latest* at the E_4 state, though E_2 or E_3 has also been suggested for N_2 binding. [31,33,111,112] Subsequently, E_5–E_8 states are generated upon further addition of electrons/protons, whereby N_2 is reduced to two NH_3, followed by the release of NH_3 and the return of enzyme to the E_0 state.

Of all steps depicted in the 'MoFe protein cycle', binding of N_2 is the first critical juncture for catalysis. ENDOR analyses of a putative E_4 state ($E_4(H_4)$) suggested the presence of two Fe-bridging hydride (H^-) units and two S-bound protons in this intermediate (designated 'Janus intermediate'). It was further proposed that binding of N_2 to a core Fe atom could trigger a formal reductive elimination of H_2, thereby generating an $E_4(N_2H_2)$ species for further reduction to NH_3 (**Figure 8B**).[117] Two main pathways have been proposed to account for this process: the distal and alternating pathways (**Figure 8C**).[111] Both pathways begin with binding of N_2 in an end-on fashion to a metal center (M–N_2) and converge at the formation of a terminal amido (M–NH_2) species, which then undergoes two successive hydrogenation steps to yield the second NH_3 while returning the enzyme to the resting state. However, the two pathways are distinct in the sites of hydrogenation, intermediates formed, and the steps at which the first NH_3 is released. In the distal pathway, the successive hydrogenation of the distal N atom results in the sequential formation of a hydrazido (M=NNH_2) intermediate, a terminal nitrido (M≡N) species concomitant with the release of the first NH_3, and a terminal imido (M=N) intermediate prior to the formation of a terminal amido (M–NH_2) species. In the alternating pathway, the alternating hydrogenation of the proximal and distal N atoms leads to the sequential formation of diazene (M–HN=NH) and hydrazine (M–H_2NNH_2) species, and further hydrogenation of the hydrazine intermediate results

in the release of the first NH_3 concomitant with the formation of the terminal amido ($M–NH_2$) species.

It should be noted that the assignment of E_4 as the critical step for N_2 binding during the 'MoFe protein cycle' is based on the assumption that the 'belt sulfurs' of the cofactor remain intact during catalysis and that the two cofactors of NifDK act in synchrony in substrate reduction.[118,119] However, recent structural and biochemical studies have revealed binding of ligands (including the isoelectronic N_2 and CO) to the cofactor of NifDK via belt-sulfur displacement,[88,89,120-123] as well as release of products of the reaction products via belt-sulfur replacement[89] and an overall dynamic movement of the belt-sulfurs during nitrogenase catalysis.[88,89,124] Moreover, DFT calculations have led to the proposal of a more reduced state than E_4, coupled with belt-sulfur displacement, as the prerequisite for N_2 binding.[125]

2.2. V-nitrogenase

2.2.1. Fe protein (VnfH)

The reductase components of the V-nitrogenases from a number of organisms, including those from *A. vinelandii* (designated *Av*VnfH), *A. chrococcum* (designated *Ac*VnfH), *C. pneumoniae* (designated *Cp*VnfH) and *M. acetivorans* (designated *Ma*VnfH),[39,56,67,126] have been characterized by structural, spectroscopic and biochemical methods. Sharing a sequence homology of 91% with its *nifH*-encoded counterpart, *Av*VnfH is a homodimer of ~60 kDa (**Figure 9A**). [126]

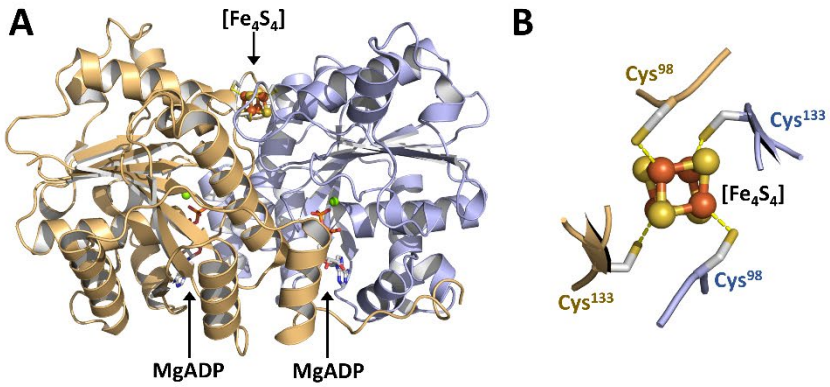

Figure 9. The Fe protein of the V-nitrogenase. Crystal structures of (A) the homodimeric Fe protein of *A. vinelandii* V-nitrogenase (*Av*VnfH) in the MgADP-bound state (PDB entry 6Q93) and (B) its associated $[Fe_4S_4]$ cluster, along with the ligands coordinating the cluster. The protein subunits, the cluster and its ligands are presented and colored as those in Figure 1. MgADP is colored as described in Figure 4.

Crystallographic analysis reveals that *Av*VnfH is highly homologous to its *Av*NifH counterpart in structure, with a [Fe_4S_4] cluster bridged at the subunit interface by a pair of Cys residues (Cys^{98} and Cys^{133}) from each subunit (**Figure 9B**), and two nucleotide-binding sites—one per subunit—that consists of a Walker A motif formed by residues 11 and 17.[126] Like *Av*NifH, *Av*VnfH can adopt the oxidized ($[Fe_4S_4]^{2+}$), reduced ($[Fe_4S_4]^{1+}$) and super-reduced, all-ferrous ($[Fe_4S_4]^{0}$) states upon *in vitro* treatment with IDS, dithionite and Ti(III) citrate/Eu(II) compounds, respectively, as observed for the AvNifH and *Ma*NifH.[22,56] The EPR characteristics of *Av*VnfH and *Ma*VnfH closely resemble those of their NifH counterparts, with the oxidized state being EPR silent, and the reduced and super-reduced states showing a mixture of $S = 3/2$ and $S = 1/2$ signals and a unique parallel-mode feature at $g = 16.4$, respectively (**Figure 10**).[22,56,127] Moreover, the EPR spectra of

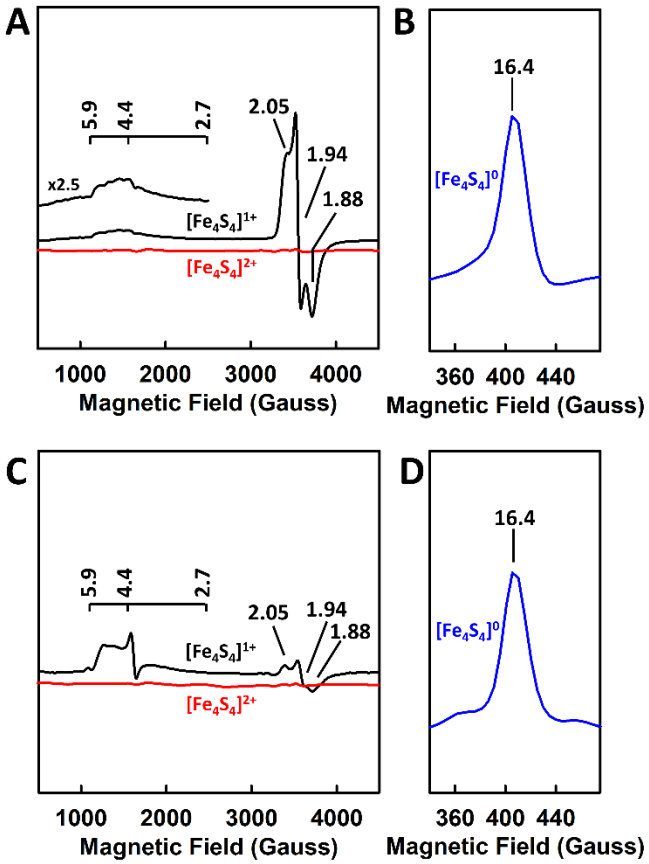

Figure 10. Oxidation states adopted by VnfH. (A, C) Perpendicular-mode EPR spectra of the reduced ($[Fe_4S_4]^{1+}$) and oxidized ($[Fe_4S_4]^{2+}$) states of VnfH from *A. vinelandii* (A; *Av*VnfH) and *M. acetivorans* (C; *Ma*VnfH). (B, D) Parallel-mode EPR spectra of the super-reduced, all-ferrous ($[Fe_4S_4]^{2+}$) states of VnfH from *A. vinelandii* (B; *Av*VnfH) and *M. acetivorans* (D; *Ma*VnfH). The *g* values are indicated (in A–D) and the $S = 3/2$ signal of the $[Fe_4S_4]^{1+}$ cluster is enlarged in the inset (in A).

these VnfH proteins are broadened upon binding of nucleotides, pointing to a long-distance 'crosstalk' between the [Fe_4S_4] cluster near the protein surface and the nucleotide binding site that is buried within the protein.[22,56,97,128,129] The midpoint potential of the $[Fe_4S_4]^{2+/1+}$ redox couple of *Av*VnfH (E_m = –346 mV) was shown to be more negative than that of *Av*NifH (E_m = –301 mV); whereas binding of nucleotides resulted in a decrease in this value, as illustrated by the potentiometric titrations of the MgADP-bound form of *Ac*VnfH (E_m = –463 mV).

2.2.2. VFe protein (VnfDGK)

The VFe protein (or VnfDGK) of the V-nitrogenase, like the MoFe protein (or NifDK) of the Mo-nitrogenase, contains an $\alpha_2\beta_2$ core, with the α- and β-subunit encoded by the *vnfD* and *vnfK* gene, respectively;[38,39] additionally, it has an additional δ-subunit, which is encoded by the *vnfG*

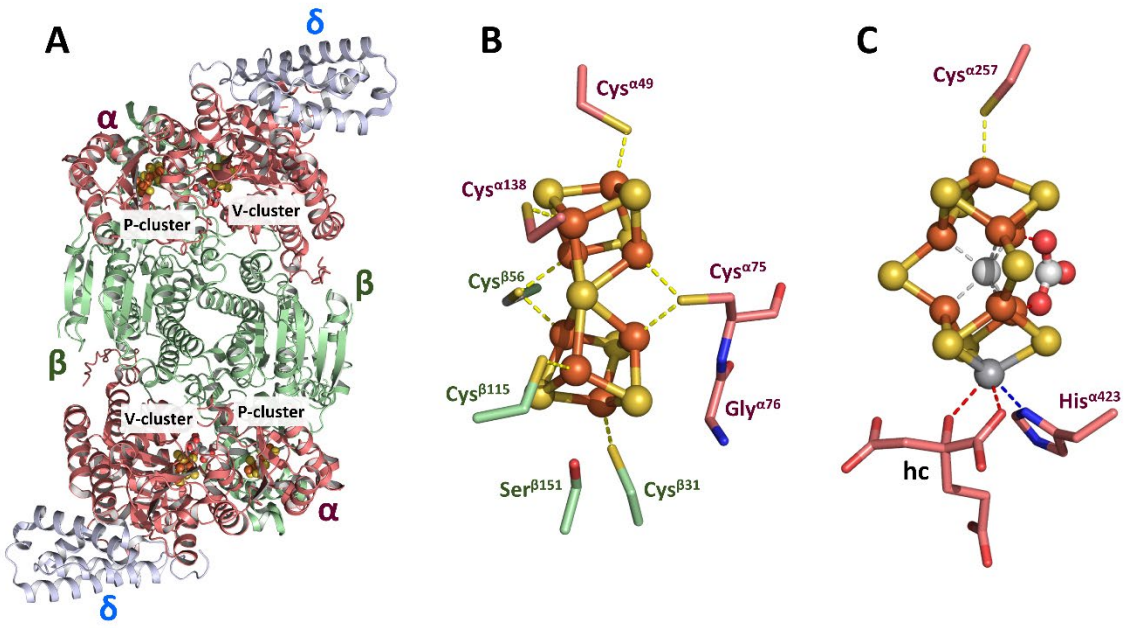

Figure 11. The VFe protein of V-nitrogenase. Crystal structures of (A) the hexatetrameric VFe protein from *A. vinelandii* (*Av*VnfDGK) (PDB entry 5N6Y) and its (B) P-cluster ([Fe_8S_7]) and (C) V-cluster (or cofactor; [(*R*-homocitrate)$VFe_7S_8C(CO_3^{2-})$]) in the reduced state, along with ligands coordinating the P- and V-clusters (B, C). The α-, β- and δ-subunits of *Av*VnfDGK are shown as ribbons and colored deep salmon, pale green and greyish blue, respectively (A). The ligands of the clusters are presented as sticks, and the clusters are shown in ball-and-stick presentation, with the atoms colored as follows: Fe, orange; V, dark gray; S, yellow; C, light gray; O, red (B). hc, homocitrate

gene. Different subunit compositions have been reported for the VnfDGK protein from *A. vinelandii* (designated *Av*VnfDGK), including an $\alpha\beta_2(\delta)$ trimer and an $\alpha_2\beta_2(\delta)$ tetramer with varying amounts of the δ-subunit, as well as an $\alpha_2\beta_2\delta_2$ hexamer of ~240 kDa and an $\alpha_2\beta_2\delta_4$ octamer of ~270 kDa, highlighting a good degree of structural variability of VnfDGK as compared to its NifDK counterpart.[39.130,131] The crystal structure of *Av*VnfDGK—derived from the $\alpha_2\beta_2\delta_2$ hexameric form of this protein—contains an $\alpha_2\beta_2$ core of ~230 kDa that is very similar to NifDK; additionally, the δ-subunit—a small, globular protein of 13 kDa—consists of four helices and is exclusively associated with the α-subunit (**Figure 11A**).[132] Like *Av*NifDK, *Av*VnfDGK contains a pair of complex metalloclusters per αβ-dimer: a P-cluster that is situated at the α/β-subunit interface and a V-cluster (also known as FeVco) that is situated within the α-subunit. However, the composition, structure and electronic properties of these clusters have remained a topic of debate (see below).

2.2.2.1. P-cluster

Crystallographic analysis of the dithionite-reduced, $\alpha_2\beta_2\delta_2$ form of *Av*VnfDGK[132] has led to the assignment of a P-cluster of the same $[Fe_8S_7]$ composition as that in NifDK, which apparently adopts the structure of the P^N state and is bridged between the α- and β-subunits by six Cys residues: three from the α-subunit ($Cys^{\alpha49}$, $Cys^{\alpha75}$, $Cys^{\alpha138}$) and three from the β-subunit ($Cys^{\beta31}$, $Cys^{\beta56}$, $Cys^{\beta115}$) (**Figure 11B**). However, there is extra electron density indicating movement of one Fe atom (Fe6) of the P-cluster towards $Ser^{\beta153}$ in a manner similar to that observed for Fe6 in the P^{OX} state. This observation resulted in the assignment of a mixed P^N/P^{1+} oxidation state for this cluster in the $\alpha_2\beta_2\delta_2$-hexameric VnfDGK, although there was no spectroscopic evidence in support of either proposal.[132]

There is, however, a plethora of EPR, MCD, XAS and Mossbauer data collected on the $\alpha\beta_2(\delta)$, $\alpha_2\beta_2(\delta)$ and $\alpha_2\beta_2\delta_4$ forms of *Av*VnfDGK, which provides important insights into the electronic and structural properties of its associated P-cluster species.[33] Consistent with earlier reports on the VnfDGK protein from *A. chroococcum* (designated *Ac*VnfDGK)[133] and the $\alpha_2\beta_2(\delta)$ form of *Av*VnfDGK,[134,135] the $\alpha_2\beta_2\delta_4$ form of *Av*VnfDGK displays a mixture of $S = 5/2$ ($g = 6.68$), $S = 3/2$ ($g = g = 5.50, 4.32, 3.77$) and $S = 1/2$ ($g = 2.03, 1.92$) EPR signals in the dithionite-reduced state (**Figure 12**).[131] Among these EPR features, the $S = 3/2$ signal has been attributed to the V-cluster (see below), whereas the $S = 1/2$ signal has remained a subject of different interpretations as to its

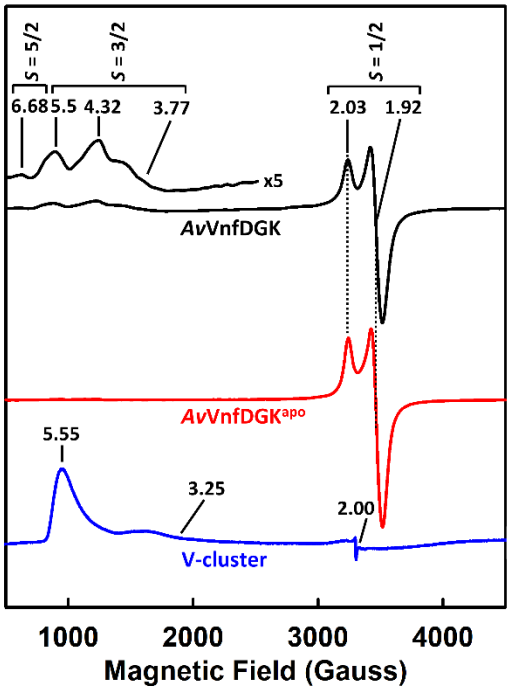

Figure 12. EPR features of the *Av*VnfDGK-associated clusters. Shown are the perpendicular-mode EPR spectra of (A) the reduced, resting-state *Av*VnfDGK; (B) the cofactor-deficient *Av*VnfDGK (*Av*VnfDGK^{apo}); and (C) the solvent-extracted V-cluster. The *g* values are indicated (in A–C). The $S = 5/2$ and $S = 3/2$ signals are enlarged in the inset (in A).

origin. Previous Mössbauer analysis assigned the $S = 1/2$ signal to the V-cluster of *Av*VnfDGK;[136] yet, the same $S = 1/2$ signal was observed for a cofactor-deplete, but P-cluster-replete form of *Av*VnfDGK,[137,138] pointing to the P-cluster as the origin of this signal (**Figure 12**). Notably, the ratio of signal intensity remains constant between the $S = 1/2$ signal and the V-cluster-originated $S = 3/2$ signal in *Av*VnfDGK preparations of varying activities, and the signal intensities of both $S = 1/2$ and $S = 3/2$ signals are proportional to the activity of the protein; moreover, both signals are attenuated under turnover conditions (*i.e.*, In the presence of *Av*VnfH, MgATP, dithionite and substrates).[131] Taken together, these observations suggest that the $S = 1/2$ signal is intimately associated with a catalytically active form of *Av*VnfDGK.

The fact that *Av*NifDK does not display the $S = 1/2$ signal of *Av*VnfDGK in the dithionite-reduced state, as well as the observation that the P^{OX}-specific, $g = 11.8$, parallel-mode EPR signal of *Av*NifDK is nearly absent from the spectrum of *Av*VnfDGK in the IDS-oxidized state, [131] suggests a difference in the oxidation state and/or structural properties of the P-clusters in these

proteins. In support of this notion, the $S = 1/2$ signal of the dithionite-reduced *Av*VnfDGK bears resemblance to the $S = 1/2$ signal ($g = 2.06$ and 1.95) of the P^{1+} state of *Av*NifDK;[80,93,139] additionally, the $S = 5/2$ feature of the $\alpha_2\beta_2\delta_4$-hexameric *Av*VnfDGK, which shows the same temperature dependency and response to oxidation as the $S = 1/2$ signal of the same protein, is very similar to that reported for the $\alpha_2\beta_2(\delta)$-tetrameric *Av*VnfDGK, which has also been assigned to a P^{1+} state.[135] XAS analysis of the cofactor-deficient, yet P-cluster-containing form of *Av*VnfDGK points to the P-cluster in this protein as a $[Fe_4S_4]$ cluster-like pair, much like the P-cluster precursor of *Av*NifDK that has been identified as a $[Fe_4S_4]$ cluster-like pair.[137] Such a 'modular' structure of P-cluster (*i.e.*, with two 4Fe units instead of a fused 8Fe entity) would account for the instability at the α/β-subunit interface and, consequently, the variability in the subunit composition of the VnfDGK species attained so far. More importantly, it renders the P-cluster in *Av*VnfDGK distinct in its redox and structural properties from the P-cluster in *Av*NifDK, which could—at least in part—differentiate V-nitrogenase from its Mo-counterpart in reactivity.

2.2.2.2. V-cluster

Crystallographic analysis of the $\alpha_2\beta_2\delta_2$ form of *Av*VnfDGK reveals an overall structural similarity and coordination pattern of the V-cluster to those of its M-cluster counterpart in NifDK.[132] Notably, the V atom occupies the same position in the V-cluster as the Mo atom in the M-cluster, although the average V-Fe distance from V to the three nearby Fe atoms (2.77 Å) is longer than the corresponding Mo-Fe distance (2.69 Å), rendering the V-cluster more elongated than its M-cluster counterpart. Like the M-cluster, the V-cluster is anchored within the α-subunit by only two protein ligands: $Cys^{\alpha 257}$ and $His^{\alpha 423}$ (**Figure 11C**). However, contrary to the M-cluster that has a composition of [(*R*-homocitrate)$MoFe_7S_9C$], the V-cluster in the crystallized, $\alpha_2\beta_2\delta_2$ form of *Av*VnfDGK has a composition of [(*R*-homocitrate)$VFe_7S_8C(CO_3^{2-})$], with one belt sulfide (S3A) of the V-cluster displaced by a carbonate (CO_3^{2-}) entity. This observation is somewhat puzzling as the presence of carbonate has never been reported for any nitrogenase cofactor, and the function and origin of this moiety remain elusive.

EPR and XAS studies have been conducted on the $\alpha\beta_2(\delta)$, $\alpha_2\beta_2(\delta)$ and $\alpha_2\beta_2\delta_4$ forms of *Av*VnfDGK to probe the electronic properties of the cofactor of this protein.[130,131,134,136,140] The V-cluster has been associated with an $S = 3/2$ system in the cases of both $\alpha_2\beta_2(\delta)$ and $\alpha_2\beta_2\delta_4$ *Av*VnfDGK proteins; however, the assignment of g values differ, with $g = 5.68$ and 5.45 assigned

to the former and g = 5.50, 4.32 and 3.77—which overlaps with the g values of = 4.3, 3.7 and 2.0 assigned to the S = 3/2 signal of M-cluster—assigned to the latter.[134] Importantly, the S = 3/2 signal of the $\alpha_2\beta_2\delta_4$ *Av*VnfDGK behaves like that of *Av*NifDK, with its intensity correlated linearly with the substrate-reducing activities and its three g values attenuated under turnover conditions.[131] Moreover, this S = 3/2 signal is attenuated concomitantly with S = 1/2 signal and S = 5/2 features upon turnover, analogous to that observed for the decrease of the S = 3/2 signal of *Av*NifDK under turnover conditions.[131] Interestingly, the EPR features of the $\alpha_2\beta_2\delta_4$-form of *Av*VnfDGK at g = 5.50 and g = 4.32, 3.77 display different temperature dependencies, as well as different responses to treatment with an oxidant: the feature at g = 5.50 disappears upon oxidation with IDS; whereas the features at g = 4.32, 3.77 remain largely unchanged.[131] These observations led to the assignment of two different S = 3/2 species in this protein, consistent with the proposal derived from earlier studies of other forms of VnfDGK.[39,131,140]

Other than the protein-bound form, the V-cluster has also been characterized upon extraction into the organic solvent, NMF.[141-143] The solvent-extracted V-cluster from the $\alpha_2\beta_2\delta_4$-form of *Av*VnfDGK displays an EPR spectrum with g values of 5.55, 3.25 and 2.00, with the g = 3.25 feature being very broad and the g = 5.55 feature aligning well with the g = 5.5-5.7 resonance that is assigned to the protein-bound V-cluster (**Figure 12**). The g = 2.00 feature, on the other hand, resembles that observed at $g \approx 2$ region of the S = 3/2 signal in the spectra of both solvent-extracted and protein-bound M-clusters (**Figure 5B**), and the absence of an intense S = 1/2 signal (g = 2.03, 1.92) from the spectrum of the isolated V-cluster provides strong support for the assignment of this signal to the P-cluster of *Av*VnfDGK. XAS/EXAFS analysis of the extracted V-cluster[143] yielded fits comparable to those of the protein-bound V-cluster[144] and, despite an inclusion of Fe-O and Fe-C scatters from the associated solvent molecules, none of these data pointed to the presence of a carbonate ligand as observed in the crystal structure.[132]

2.3. Fe-only nitrogenase

2.3.1. Fe protein (AnfH)

Encoded by the *anfH* gene, the reductase component (or AnfH) of the *A. vinelandii* Fe-only nitrogenase shares sequence homology with its counterparts from both Mo- and V-nitrogenases, although it is the most distinct member in this family that shares only ~60% similarity in sequence

with the other two Fe proteins. However, such a difference is not apparent when the crystal structure of the AnfH protein from *A. vinelandii* (designated *Av*AnfH) is compared to those of *Av*NifH and *Av*VnfH, as all three Fe proteins are structurally nearly identical to one another.[44,126,145] Like its *Av*NifH and *Av*VnfH counterparts, *Av*AnfH is a ~60 kDa homodimer with the same Rossmann-type βαβ-fold; moreover, it contains a subunit-bridging [Fe_4S_4] cluster ligated by Cys^{97} and Cys^{131} from each subunit (**Figure 13**), as well as a nucleotide-binding site that consists of a

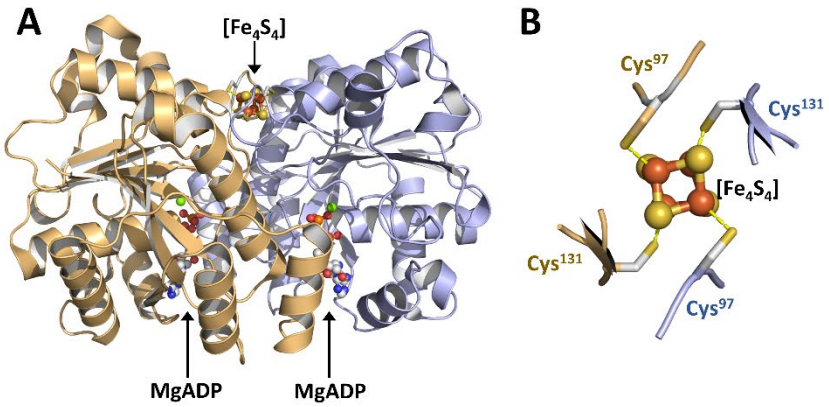

Figure 13. The Fe protein of the Fe-only nitrogenase. Crystal structures of (A) the homodimeric Fe protein of *A. vinelandii* Fe-only nitrogenase (*Av*AnfH) in the MgADP-bound state (PDB entry 7QQA) and (B) its associated [Fe_4S_4] cluster, along with the ligands coordinating the cluster. The protein subunits, the cluster and its ligands, and MgADP are presented and colored as those in Figure 9.

Walker A motif in each subunit. [145] Interestingly, while Fe K-edge XAS/EXAFS analysis agrees with crystallography in assigning nearly indistinguishable conformations to the $[Fe_4S_4]^{1+}$ clusters of *Av*NifH, *Av*VnfH and *Av*AnfH, it indicates a slightly different conformation adopted by the *Av*NifH associated cluster, with its two [Fe_2S_2] rhomboids bent to a greater degree out-of-plane relative to each other than those of its counterparts in *Av*VnfH and *Av*AnfH.[127] This is surprising given the higher sequence identity between *Av*NifH and *Av*VnfH (91%) than that between *Av*VnfH and *Av*AnfH (61%). Clearly, more work is required to provide answers to questions arising from these observations.

2.3.2. FeFe protein (AnfDGK)

The FeFe protein (or AnfDGK) of the Fe-only nitrogenase, like the VFe protein (or VnfDGK) of the V-nitrogenase, is encoded by three structural genes, with the *anfD*, *anfK* and *anfG* genes encoding its α (~59 kDa), β (~51 kDa) and δ (~14 kDa) subunits, respectively. While the crystal

structure of AnfDGK has not been reported to date, it is believed to be structurally similar to its counterparts in both V- and Mo-nitrogenases in the $\alpha_2\beta_2$ core structure, with a pair of homologous metalloclusters—the P-cluster and the Fe-cluster (also called FeFeco)—that are homologous to their respective counterparts in V- and Mo-nitrogenases within each αβ-dimer. The AnfDGK protein has been isolated from *A. vinelandii* (designated *Av*AnfDGK), *R. capsulatus* (designated *Rc*AnfDGK), *R. palustris* (designated *Rp*AnfDGK) and *R. rubrum* (designated *Rr*AnfDGK) and, as described for VnfDGK, various subunit compositions have been reported for *Av*AnfDGK and *Rc*AnfDGK, including an $\alpha\beta_2$ trimer, an $\alpha_2\beta_2$ tetramer and an $\alpha_2\beta_2\delta_2$ hexamer of ~250 kDa, highlighting a structural variability of AnfDGK much like that of its VnfDGK counterpart.[39,140,146,147] EPR and Mössbauer studies of partially purified *Rc*AnfDGK led to the observation of a featureless EPR spectrum of this protein in the dithionite-reduced state, as well as the assignment of both the P- and Fe-clusters as a diamagnetic $S = 0$ state.[99,146,148,149] Additionally, an $S = 1/2$ ($g = 1.96, 1.92, 1.77$) appeared in the spectrum of *Rc*AnfDGK under turnover conditions, which was assigned to the one-electron-reduced Fe-cluster; whereas two $S = 1/2$ signals ($g = 2.00, 1.09, 1.96$; $g = 2.07, 2.06$) were observed upon potentiometric titrate of *Rc*AnfDGK at E_m values of –80 mV and +80 mV *vs*. SHE, and associated with the three-electron-oxidized P^{3+} cluster and the one-electron-oxidized Fe-cluster, respectively.[99] Fe K-edge XAS analysis revealed a structural analogy between *Rc*AnfDGK and *Rc*NifDK; in particular, the necessity to include an Fe---Fe distance of 3.68 Å, a characteristic feature of the cofactor core comprising six Fe atoms—for the best fit of EXAFS data implies the presence of the core structure in the Fe-cluster of AnfDGK.[148] Together, these studies provided valuable initial insights into the elusive Fe-only nitrogenase, though further studies are required to fully elucidate the structural and electronic properties of this nitrogenase.

3. Reactivities of nitrogenase-based Fischer-Tropsch-type reactions

Consistent with a difference in their structural and redox properties, the three homologous nitrogenases display differential reactivities with a given substrate. However, while the specific activities of the three nitrogenases in reducing the 'standard' substrates (N_2, C_2H_2, H^+) rank in a decreasing order of Mo-nitrogenase > V-nitrogenase > Fe-only nitrogenase (**Figure 14A**),[33] the V-nitrogenase displays a substantially higher activity than both Mo- and Fe-only nitrogenases in the FT-type reactions wherein CO or CO_2 is reduced to hydrocarbons (**Figure 14B**).[33] The FT-

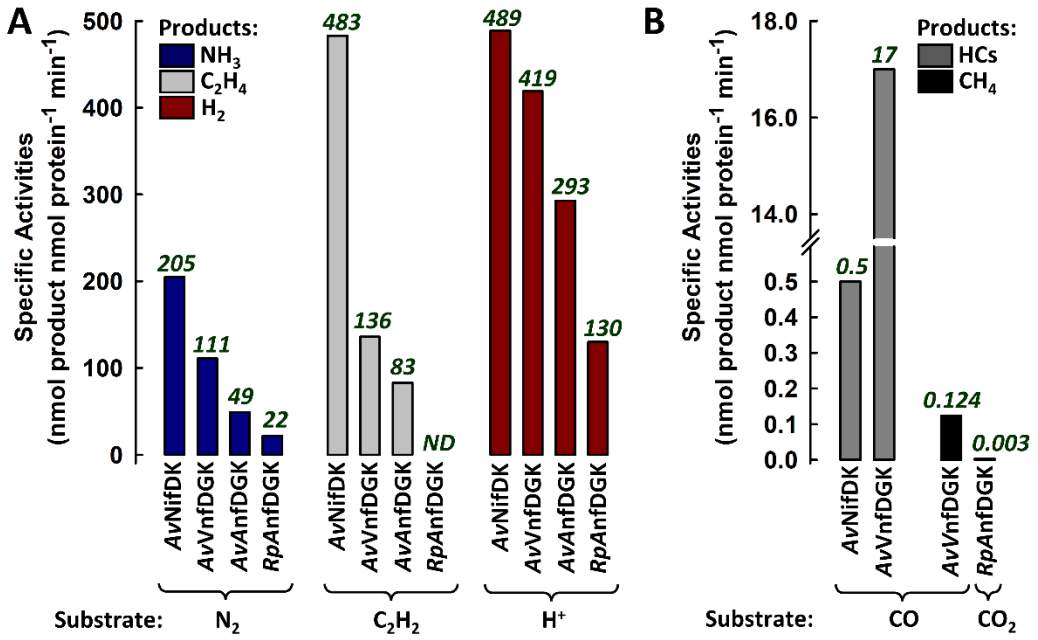

Figure 14. Comparison of the substrate-reducing activities of Mo-, V- and Fe-only nitrogenases. Shown are the specific activities of the Mo- and V-nitrogenases from *A. vinelandii* (*Av*NifDK and *Av*VnfDGK) and the Fe-only nitrogenase from *R. palustris* (*Rp*AnfDGK) in reducing (A) the 'conventional' substrates (N_2, C_2H_2 and H^+) and (B) the 'unconventional' C_1 substrates (CO, CO_2).

type reactivities can be accomplished by the complete two-component nitrogenase systems in ATP-dependent reactions, as well as each of its component proteins in ATP-independent reactions. Additionally, the extracted cofactors and their synthetic mimics are also capable of enabling ATP-independent FT-type reactivities. The FT-type reactivities of these various nitrogenase-based systems will be discussed in detail in this section.

3.1. Enzyme-based Fischer-Tropsch-type reactions

3.1.1. Two-component Fischer-Tropsch-type systems

The two-component FT-type systems catalyze the reduction of CO or CO_2 to hydrocarbons in an *in vitro* assay comprising both components of the purified nitrogenase enzyme alongside MgATP and dithionite. The enzymatic FT-type reactivity was first observed for the wildtype V-nitrogenase in such a reaction system, which was capable of reducing CO to C_1-C_4 alkanes (CH_4, C_2H_6, C_3H_8, C_4H_{10}) and alkenes (C_2H_4, C_3H_6, C_4H_8).[15,17] Subsequent GC-MS analysis led to the

observation of expected mass shifts upon substitution with ^{13}CO and D_2O in this reaction, confirming CO as the source of the reduced C atoms in the hydrocarbon products while establishing protons/electrons as the reducing equivalents in the enzymatic FT-type reactions.[15-17] Moreover, comparative analysis revealed distinctions and similarities between the FT-type reactivities of the wildtype V- and Mo-nitrogenases.[17] The biggest difference between the two homologous nitrogenases is their efficiencies in CO reduction, with the former generating C_1-C_4 alkanes (CH_4, C_2H_6, C_3H_8, C_4H_{10}) and alkenes (C_2H_4, C_3H_6, C_4H_8) at a specific activity of ~8300 nmol total reduced C atoms per μmol cofactor per min in an H_2O-based reaction, nearly 800- and 25-fold, respectively, more active than the wildtype and $Val^{\alpha 70}$-substituted variants of Mo-nitrogenase (**Table 1**).[153]

It should be noted, however, that the activities of the $Val^{\alpha 70}$-substituted variants were not compared with those of the wildtype Mo-nitrogenase under the same reaction conditions and, additionally, the activities of the $Val^{\alpha 70}$ variants were measured in the presence of a substantially higher concentration of the reductant (200 mM dithionite)[153] than that used in the comparative activity analysis of the wildtype V- and Mo-nitrogenases (20 mM dithionite).[17] Recently, we performed the CO-reduction assay with the wildtype Mo-nitrogenase at 200 mM dithionite, which revealed an increased activity compared to that observed in the assay containing 20 mM dithionite (**Table 1**). This observation suggests that more work is needed to directly compare the activities of the wildtype and variant Mo-nitrogenases under the same assay conditions in order to thoroughly evaluate the impact of $Val^{\alpha 70}$ on CO reduction.

Interestingly, both V- and Mo-nitrogenases display an inverse KIE effect in CO reduction. A comparison of the CO-reducing activities in D_2O with those in H_2O reveals average KIEs of ~0.1 and ~0.5, respectively, for the Mo- and V-nitrogenases. Overall, the specific activity of the Mo-nitrogenase is increased by 21-fold upon substitution of H_2O with D_2O, and the increase in activity is accompanied by a notable expansion of product profile to allow inclusion of longer, C_4 products (C_4H_8, C_4H_{10}); in comparison, the specific activity of the V-nitrogenase is increased by only ~12% following such a substitution, and the product profile remains largely unchanged (**Table 1**).[17] Other than showing a clear difference in the deuterium isotope effect, the reaction catalyzed by the V-nitrogenase has a considerably higher C_2H_4:C_2H_6 ratio (31:1 in H_2O; 23:1 in D_2O) than that catalyzed by the Mo-nitrogenase (2:1 in H_2O; 7:1 in D_2O) (**Table 1**).[17] A common trait shared by

Table 1. Activities of two-component FT-type systems of nitrogenase

Substrate (CO)		Products (nmol product x µmol cofactor^{-1} x min^{-1})									
Protein	**Solvent**	**CH_4**	**C_2H_4**	**C_2H_6**	**C_3H_6**	**C_3H_8**	**C_4H_8**	**C_4H_{10}**	**Activities**	**TON**	**refs**
*Av*VnfDGK	H_2O	62	3868	123	6	69	0.3	0.4	8272	461	17
*Av*VnfDGK	D_2O	145	4205	187	27	71	0.8	1.2	9231	487	17
*Av*VnfDGK [a]	H_2O		4608	151	51	7			9635		This work
*Av*VnfDGK^{M} [b]	H_2O		1300	42	5.4	22	3.4		2780		150
*Av*VnfDGK^{Cit}	H_2O		2128	58					4372		138
*Av*NifDK	H_2O		2.8	1.4	0.3	0.7			11	1	17
*Av*NifDK	D_2O		80	12	6	7	0.8	0.8	229	13	17
*Av*NifDK [a]	H_2O		8.2	3.4	2.1	0.9			29		This work
*Av*NifDK^{M} [c]	H_2O		3	2	0.3	0.5			12		151
*Av*NifDK^{M} [c]	D_2O	11	45	8	5	3	0.7	0.8	147		151
*Av*NifDK^{V} [c]	H_2O		4	1	0.4	0.3			12		151
*Av*NifDK^{V} [c]	D_2O	9	40	10	5	2	0.7	1	137		151
*Av*NifDK^{Cit}	H_2O		14	4					36		152
*Av*NifDK^{V70A} [a, d]	H_2O		65	20	40	7			311	36	153
*Av*NifDK^{V70G} [a ,d]	H_2O		65	20	60	7			371	43	153

Substrate (CO_2)		Products (nmol product x µmol cofactor^{-1} x min^{-1})						
Protein	**Solvent**	**CO**	**CH_4**	**C_2H_4**	**C_2H_6**	**Activities***	**TON***	**refs**
*Av*VnfDGK [e]	H_2O	1		<0.01		1	0.14	154
*Av*VnfDGK [e]	D_2O	2	0.1	0.2	<0.01	2.5	0.33	154
*Av*NifDK [e]	H_2O	0.4	0.1 [f]	<0.01		0.4 [f]	0.08 [f]	154
*Av*NifDK [e]	D_2O	2			<0.01	2	0.26	154
*Rp*AnfDGK [g]	H_2O		1.5			1.5	0.6	29

The specific activities are expressed as total nmol of reduced carbons in products per µmol cofactor per min. TON refers to the turnover number calculated based on total nmol of reduced carbons in products per nmol cofactor.

[a] Assays contained 200 mM dithionite.

[b] The V-cluster of *Av*VnfDGK was replaced by the M-cluster (as indicated by the superscript) *in vivo* via deletion of *nifV*, the gene encoding homocitrate synthase.

[c] The cofactor-deficient *Av*NifDK was reconstituted with the isolated M- or V-cluster (as indicated by the superscript) *in vitro*.

[d] The specific activities and TONs were calculated based on the values shown in Fig. 1 of ref 153 at 20 and 90 min, respectively. The *Av*NifDK variants wherein the Val$^{\alpha 70}$ residue were mutated to Ala and Gly, respectively, are designated *Av*NifDK^{V70A} and *Av*NifDK^{V70G}.

[e] The specific activities and TONs were calculated based on the values shown in Fig. 2 of ref 154 at 60 and 180 min, respectively.

[f] The isotopic mass shift for $^{13}CH_4$ was not observed when ^{13}CO was used as substrate. Therefore, the values were not included for the calculations of the total C and TON.

[g] The reported activity for CH_4 formation was ~1.1 nmol/nmol protein based on Fig. 2 of ref 29. The product was quantified after 6 h.

the two homologous nitrogenases, however, is that C_2H_4—a product representing the formation of the first C-C bond via reductive coupling—is the predominant product of CO reduction in the H_2O- and D_2O-based reactions catalyzed by both V- and Mo-nitrogenases; in contrast, CH_4, a product generated via direct hydrogenation of CO, is only a minor product for the V-nitrogenase and undetected for the Mo-nitrogenase under the same reaction conditions (**Table 1**).[17] Moreover, both nitrogenases favor formation of the unsaturated C_2 product (*i.e.*, a higher C_2H_4:C_2H_6 ratio) but

saturated ≥C_3 products (*i.e.*, higher C_3H_8:C_3H_6 and C_4H_{10}:C_4H_8 ratios) (**Table 1**).[17] Taken together, these observations point to a preferred formation of the first C-C bond over a complete reduction of CO, as well as a plausible mechanistic switch from the C_2 stage to events beyond C_2 concerning the conversion rate between alkene and alkane that is absent from any other FT-type system that do not rely on the intricate, ATP-dependent mode of action of the two-component nitrogenase enzyme (see below).

The difference between the FT-like reactivities of the V- and M-nitrogenases was further tackled by 'swapping' their cofactors and generating an M-cluster-substituted V-nitrogenase hybrid (designated V-nitrogenase^M, with its catalytic component designated as *Av*VnfDGK^M)[150] or a V-cluster-substituted Mo-nitrogenase hybrid (designated Mo-nitrogenase^V, with its catalytic component designated as *Av*NifDK^V).[151] Strikingly, the M-cluster in V-nitrogenase^M displays an $S = 3/2$ EPR signal (g = 5.36, 4.48, 3.46) that is very similar to that of the V-cluster in the native V-nitrogenase (g = 5.50, 4.32, 3.77), but clearly distinct from that of the M-cluster in the native Mo-nitrogenase (g = 4.31, 3.67) (**Figure 15**).[150] Consistent with their spectral similarities, the V-

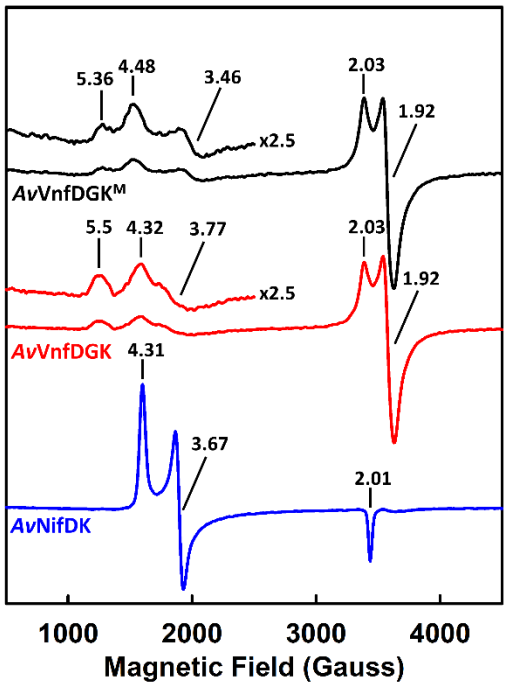

Figure 15. EPR features of an M-cluster-substituted V-nitrogenase hybrid. Perpendicular-mode EPR spectra of (A) the M-cluster-substituted *Av*VnfDGK (*Av*VnfDGK^M); (B) the wildtype *Av*VnfDGK; and (C) the wildtype *Av*NifDK. The g values are indicated. The S = 5/2 and S = 3/2 regions of the spectra of *Av*VnfDGK^M (black) and *Av*VnfDGK (red) are enlarged in the insets.

nitrogenase^{M} hybrid resembles the native V-nitrogenase in the reactivity with CO, showing a substantially higher activity of hydrocarbon formation (by ~250-fold) than that achieved by the Mo-nitrogenase, as well as a significantly increased C_2H_4:C_2H_6 ratio (31:1 in H_2O) that is indistinguishable from that observed for the V-nitrogenase (**Table 1**). [150] The observation of catalytic traits of the V-nitrogenase upon incorporation of an M-cluster into a V-nitrogenase protein scaffold highlights a significant impact of the protein environment on the FT-like reactivity of nitrogenase. On the other hand, the V-nitrogenase^{M} hybrid is still ~3-fold less active than its native V-counterpart in CO reduction, and it does not generate detectable amounts of CH_4 (**Table 1**), both of which are reminiscent of the characteristics of the native Mo-nitrogenase in the enzymatic FT-type reaction. Such a combined contribution from the cofactor and the protein environment to the FT-like reactivity of nitrogenase is further illustrated by the observation that although the Mo-nitrogenase^{V} hybrid resembles the Mo-nitrogenase in having a ~750-fold lower CO-reducing activity than the V-nitrogenase, its associated V-cluster transfers certain traits associated with the V-nitrogenase, such as the formation of more C_2H_4, upon incorporation into the protein scaffold of Mo-nitrogenase (**Table 1**).[151] The impact of cofactor properties on the FT-type reactivity was also probed by altering the homocitrate ligand in the cofactor and generating a citrate-substituted variant of V-nitrogenase (designated V-nitrogenase^{Cit}, with its catalytic component designated as *Av*VnfDGK^{Cit}) or Mo-nitrogenase (designated Mo-nitrogenase^{Cit}, with its catalytic component designated as *Av*NifDK^{Cit}).[138,152] Interestingly, while the V-nitrogenase^{Cit} variant displays a decreased hydrocarbons:H_2 ratio (under CO) concomitant with an increased NH_3:H_2 ratio (under N_2), the Mo-nitrogenase^{Cit} variant displays an increased hydrocarbons:H_2 ratio (under CO) concomitant with a decreased NH_3:H_2 ratio (under N_2) (**Figure 16**). The mechanistic details of such an opposite impact of citrate substitution on the FT reactivities of the V- and Mo-nitrogenases, however, await further investigation.

Unlike CO that has long been regarded as a potent inhibitor of N_2 reduction by the Mo-nitrogenase, CO_2 was previously shown to be reduced by the wildtype Mo-nitrogenase to CO and H_2O at a rate of 0.8 nmol product/mg protein/min.[155] The discovery of nitrogenase-catalyzed reduction of CO to hydrocarbons led to the question of whether CO_2, an atypical FT substrate, could also be reduced by nitrogenase to hydrocarbon products. Subsequent studies provided answer to this question, showing reduction of CO_2 to hydrocarbons by the V- and Mo-nitrogenases from *A. vinelandii*[154] and the Fe-only nitrogenase from *R. palustris*,[29] with the *A. vinelandii*

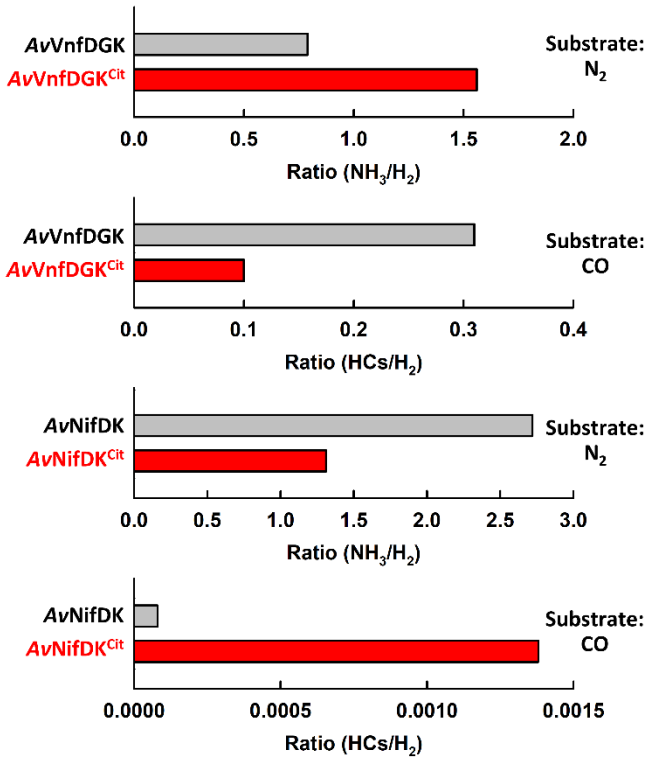

Figure 16. Impact of citrate substitution on the substrate reducing activities of V- and Mo-nitrogenases. Shown are the NH_3/H_2 and hydrocarbons (HCs)/H_2 ratios of the reactions of N_2- and CO-reduction, respectively, by citrate-substituted *Av*VnfDGK (*Av*VnfDGK^{Cit}) and *Av*NifDK (*Av*VnfDGK^{Cit}) as compared to with those by their respective wildtype *Av*VnfDGK and *Av*NifDK counterparts. HCs, hydrocarbons

enzymes producing up to C_2 hydrocarbons alongside CO and the *R. palustris* enzyme generating CH_4 as the sole product of CO_2 reduction (**Table 1**). The two *A. vinelandii* nitrogenases behave similarly in the formation of CO from CO_2 reduction, generating comparable amounts of CO in H_2O- or D_2O-based reactions and showing the same inverse KIE that is increased by one order of magnitude in the D_2O-based reaction (2 nmol CO/μmol cofactor/min) relative to that in the H_2O-based reaction (**Table 1**).[154] However, the two *A. vinelandii* nitrogenases behave differently in the formation of hydrocarbons from CO_2 reduction: the V-nitrogenase generates CD_4, C_2D_4 and C_2D_6 at 0.1, 0.2, and <0.01 nmol CO/μmol cofactor/min, respectively, in D_2O, but no detectable amounts of hydrocarbons in H_2O; whereas the Mo-nitrogenase shows a general lack of ability to generate hydrocarbons in H_2O and D_2O except for the formation of a small amount of CH_4 in H_2O (**Table 1**).[154]Curiously, while GC-MS analysis with $^{13}CO_2$ conclusively assigned CO_2 as the carbon source of all hydrocarbons (include CH_4) generated by the V-nitrogenase, the expected mass shift was not

observed in CH_4 generated by the Mo-nitrogenase, suggesting that a carbon source other than CO_2 was responsible for this product.[154] Similarly, a $Val^{\alpha 70}$ variant of the Mo-nitrogenase was shown to generate CH_4 in the presence of CO_2, but the GC-MS data attained with $^{13}CO_2$ was inconclusive to assign CO_2 as the source of C in CH_4.[153] Taken together, the observation that the V- and Mo-nitrogenases display the same inverse KIE effect in CO formation points to a common mechanism used by both nitrogenases to reduce CO_2 to CO, whereas the observation of disparate isotope effects on the formation of hydrocarbons by the two nitrogenases implies distinct properties of these enzymes that underlie their differential FT-type reactivities.

3.1.2. Single-component Fischer-Tropsch-type systems

3.1.2.1. Systems comprising the catalytic component

The single-component FT-type system comprising the catalytic component of the purified nitrogenase enzyme supports the reduction of CO or CO_2 to hydrocarbons in an *in vitro* assay wherein the reducing equivalents are supplied either chemically (*i.e.*, by strong reductants like Eu(II) compounds) or electrochemically. Contrary to the two-component nitrogenase enzyme, the reaction is carried out in the absence of the reductase component (*i.e.*, the Fe protein, an ATPase) and is therefore ATP-independent. Driven directly by Eu(II) DTPA ($E_m = -1.14$ V *vs.* SHE at pH 8), *Av*VnfDGK can reduce CO_2 to CO and C_1-C_4,[23] showing a wider product profile than that accomplished by the two-component V-nitrogenase in the presence of dithionite,[154] where only C_1 and C_2 hydrocarbons are formed alongside CO as the products of CO_2 reduction (**Table 2**). The behavior of *Av*VnfDGK in the ATP-independent reaction of CO_2 reduction is clearly distinct from that of the complete V-nitrogenase in the ATP-dependent reaction with respect to CH_4 formation. In the case of the former, CH_4 is formed in the H_2O-based reaction, but absent from the D_2O-based reaction; whereas in the case of the latter, CH_4 is absent from the H_2O-based reaction but produced in the D_2O-based reaction (**Tables 1** and **2**).[23,154] Other than CH_4, however, substitution of H_2O with D_2O has an inverse KIE effect on the formation of all other products (including CO and C_2-C_4 hydrocarbons) in the ATP-independent CO_2 reduction by *Av*VnfDGK (**Table 2**),[23] much like that observed for all products in the ATP-dependent CO_2- and CO-reduction by the two-component V-nitrogenase (**Table 1**).[17,154] The disparate isotope effects may imply a different route to CH_4 formation undertaken by *Av*VnfDGK upon substitution of the reductase component with chemical reductants.

Table 2. Activities of single-component FT-type systems comprising the catalytic component of nitrogenase

Substrate (CO)			**Products (nmol product x µmol cofactor^{-1} x min^{-1})**											
Protein	**Solvent**	**Reductant**	**CH_4**	**C_2H_4**	**C_2H_6**	**C_3H_6**	**C_3H_8**	**C_4H_8**	**C_4H_{10}**	**C_5H_{10}**	**C_5H_{12}**	**Activity**	**TON**	**refs**
*Av*NifDK$^{\Delta nifB}$	H_2O	Eu(II) DTPA	0.1	0.02	0.01							0.1	0.01	24
*Av*NifDK$^{\Delta nifB\Delta nifZ}$	H_2O	Eu(II) DTPA	0.2	0.1	0.03	0.01	0.04					0.6	0.1	24
*Av*NifDK$^{\Delta nifH}$	H_2O	Eu(II) DTPA	0.7	0.2	0.1	0.01	0.02					1.5	0.2	24
Substrate (CO_2)			**Products (nmol product x µmol cofactor^{-1} x min^{-1})**											
Protein	**Solvent**	**Reductant**	**CO**	**CH_4**	**C_2H_4**	**C_2H_6**	**C_3H_6**	**C_3H_8**	**C_4H_8**	**C_4H_{10}**		**Activity***	**TON***	**refs**
*Av*VnfDGK [a]	H_2O	Eu(II) DTPA	0.8	0.2	0.02	0.02	0.01	0.01	0.002	0.003		1.1	0.2	23
	D_2O	Eu(II) DTPA	1		0.04	0.03	0.03	0.01	0.01	0.01		1.3	0.3	23
*Av*VnfDGK [b]		Echem		0.02	0.01		0.02					0.1	0.2	28
Substrate (CN^-)			**Products (nmol product x µmol cofactor^{-1} x min^{-1})**											
protein	**solvent**	**reductant**	**CH_4**	**C_2H_4**	**C_2H_6**	**C_3H_6**	**C_3H_8**	**C_4H_8**	**C_4H_{10}**	**C_5H_{10}**	**C_5H_{12}**	**Activity***	**TON***	**refs**
*Av*NifDK$^{\Delta nifB}$	H_2O	Eu(II) DTPA	0.8	0.7	0.2	0.2	0.02					3	0.4	24
*Av*NifDK$^{\Delta nifB\Delta nifZ}$	H_2O	Eu(II) DTPA	4	4	1	1.5	0.3	0.6	0.1	0.02		23	3	24
*Av*NifDK$^{\Delta nifH}$	H_2O	Eu(II) DTPA	11	10	2	4	0.6	1.3	0.2	0.5	0.1	58	7	24
*Av*NifDK^{Fe6} [c]	H_2O	Eu(II) DTPA	356	59	30	15	4					589	37	157
*Av*NifDK^{Mo} [d]	H_2O	Eu(II) DTPA	107	16	9	6	1.5					179	28	158

The specific activities and TONs are expressed as described in Table 1.

[a] The specific activities for the generation of C_1 products were calculated based on values shown in Fig. 2 of ref 23 at 60 min. The specific activities for the generation of $\geq C_2$ products were calculated based on values shown in Fig. 3 of ref 23 at 120 min. TONs were calculated based on the values shown at the end of the time courses in these figures.

[b] The reported activities for the generation of CH_4, C_2H_4 and C_2H_6 were ~35, 25, and 42 nmol product x µmol protein^{-1}. The products of the bulk bioelectrosynthesis were reported to be quantified after 20 h. Echem, electrochemically driven reaction

[c] The specific activities and TONs were calculated based on the values shown in Fig. 3A of ref 157 at 15 and 90 min, respectively.

[d] The specific activities and TONs were calculated based on the values shown in Fig. 4A of ref 158 at 15 and 90 min, respectively.

The ability of *Av*VnfDGK to perform ATP-independent reduction of CO_2 was also examined in an electrochemical setup, wherein cobaltocene derivatives were used as electron mediators.[28] Application of potential to *Av*VnfDGK in an electrolyte solution containing $NaHCO_3$ as the source of CO_2 resulted in the formation of CH_4, C_2H_4 and C_3H_6 in an approximately equimolar ratio (**Table 2**); however, CO, the major product of CO_2 reduction by VnfDGK in ATP-dependent and ATP-independent reactions,[23,154] was not detected in this case.[28] In a similar study, CO_2 was shown to be reduced electrochemically by *Av*NifDK and *Av*AnfDGK to formate (HCO_2^-), although this reaction resembles the characteristics of formate dehydrogenase rather than those of a FT-type system.[156]

Interestingly, the cofactor-deficient variants of the catalytic component of Mo-nitrogenase have also been shown to catalyze the reduction of CO_2, CO and CN^- to hydrocarbons in an ATP-independent manner (**Table 2**).[24] Driven by Eu(II) DTPA, a *Av*NifDK variant (designated *Av*NifDK$^{\Delta nifH}$), which is cofactor-deficient and contains a [Fe_4S_4]-like cluster pair in place of the [Fe_8S_7] P-cluster per αβ-dimer, can reduce a CO_2/HCO_3^- mixture to C_2 and C_3 hydrocarbons, and CO to C_1-C_4 hydrocarbons.[24] When CN^-, an isoelectronic analog of CO, is supplied as a substrate, *Av*NifDK$^{\Delta nifH}$ can generate C_1-C_7 hydrocarbons alongside NH_3 as the products of CN^- reduction (**Table 2**).[24] The specific activities of *Av*NifDK$^{\Delta nifH}$ in CO- and CN^--reduction are 1.5 and 58 nmol total reduced C atoms per μmol cofactor per min, respectively (**Table 2**); whereas the specific activities of this *Av*NifDK variant in CO_2 reduction was too low to be accurately determined.[24] Strikingly, the ability of *Av*NifDK$^{\Delta nifH}$ to generate hydrocarbons from CO or CN^- reduction seems to be associated with the [Fe_4S_4] cluster pair—a biosynthetic precursor to the P-cluster—at its P-cluster site, as the rates of product formation by several *A. vinelandii* NifDK variants containing varying amounts of this P-cluster precursor are ranked in the order of *Av*NifDK$^{\Delta nifH}$ (containing two [Fe_4S_4]-like cluster pairs) > *Av*NifDK$^{\Delta nifB\Delta nifZ}$ (containing one [Fe_4S_4]-like cluster pair) > *Av*NifDK$^{\Delta nifB}$ (containing two P-clusters), with the activity of the P-cluster-containing *Av*NifDK$^{\Delta nifB}$ variant hardly detectable in these reactions (**Table 2**).[24] This observation aligns well with the more recent finding that the reductase component of nitrogenase (*i.e.*, the Fe protein), which contains a subunit-bridging [F_4S_4] cluster, is capable of reducing CO and CO_2 to hydrocarbons (**Table 3**) (see section 3.1.2.2 below).

3.1.2.2. Systems comprising the reductase component

The single-component FT-type system comprising the reductase component of the purified nitrogenase enzyme supports the reduction of CO or CO_2 to hydrocarbons in an *in vitro* assay wherein the reducing equivalents are supplied by chemical reductants (*i.e.*, Eu(II) compounds). Such a system catalyzes the reduction of CO or CO_2 at the [Fe_4S_4] center of the reductase component, taking advantage of the redox versatility of this unique FeS protein. The initial observation of this reactivity was made for *Av*NifH and *Av*VnfH, both of which demonstrated an ability to reduce CO_2 to CO in the nucleotide-free and ATP-bound states when dithionite was supplied as a reductant (**Table 3**).[22] The yields of CO from CO_2 reduction were 37 and 47 nmol total reduced C atoms per μmol cofactor, respectively, for the nucleotide-free *Av*NifH and *Av*VnfH in the presence of dithionite (**Table 3**). In the presence of ATP, however, the yields of CO by *Av*NifH and *Av*VnfH increased by 50% and 30% (**Table 3**), respectively, likely due to a decrease in the reduction potentials of their associated [Fe_4S_4] clusters by ~100 mV upon binding of ATP.[22] Substitution of dithionite with a stronger reductant, Eu(II) DTPA ($E^{0\prime}$ = –1.14 V *vs.* SHE at pH 8), resulted in a 25-fold increase in product yield to 916 and 1127 nmol total reduced C atoms per μmol cofactor, respectively, for the nucleotide-free *Av*NifH and *Av*VnfH (**Table 3**); moreover, a replenishment of Eu(II) DTPA 're-ignited' the reactions of CO_2 reduction by these proteins, yielding a total turnover number of 8 for both *Av*NifH and *Av*VnfH (**Table 3**).[22] The reactivities of these Fe proteins with CO_2 have been associated with their [Fe_4S_4] centers, as incubation of CO_2 with dithionite- or Eu(II) DTPA-reduced *Av*NifH or *Av*VnfH resulted in a decrease in the magnitude of the characteristic EPR signal of the reduced, $[Fe_4S_4]^{1+}$ state (the S = 1/2 signal at g = 2.95, 1.94, 1.89; perpendicular mode) or the super-reduced, all-ferrous $[Fe_4S_4]^0$ state (the g = 16.4 feature; parallel mode), consistent with oxidation of the cluster to an EPR-silent state following transfer of electrons to the substrate, CO_2.[22] Additionally, a new EPR signal at g = 1.99 (perpendicular mode) appeared in the spectra of both dithionite-reduced and Eu(II) DTPA-reduced *Av*NifH and *Av*VnfH, which likely resulted from an interaction between the cluster and the substrate, CO_2.[22] Interestingly, despite their ability to interact with CO_2 and reduce it to CO, the two Fe proteins from *A. vinelandii* were unable to generate hydrocarbons as products of CO_2 reduction, nor were they able to reduce CO into hydrocarbons; instead, both Fe proteins were capable of oxidizing CO to CO_2 in the presence of IDS at a considerably higher rate than that of the reduction of CO_2 to CO.[22] The ability to enable an ambient interconversion between CO_2 and CO makes the Fe protein a functional mimic of the Ni-containing CO-dehydrogenase, with the

Table 3. Activities of single-component FT-type systems comprising the reductase component of nitrogenase

Substrate (CO)		**Products (nmol product x µmol cofactor^{-1})**									
Protein	**Reductant**	**CH_4**	**C_2H_4**	**C_2H_6**	**C_3H_6**	**C_3H_8**	**C_4H_8**	**C_4H_{10}**	**Total C**	**TON**	**refs**
*Av*NifH [a]	100 mM Eu(II) DTPA									0	21
*Ma*NifH [a]	100 mM Eu(II) DTPA	7726	2730	1557	1728	989	744	483	29359	29	21
*Ma*VnfH [a]	100 mM Eu(II) DTPA	964	253	193	115	169	48	54	3114	3.1	67
Substrate (CO_2)		**Products (nmol product x µmol cofactor^{-1})**									
Protein	**Reductant**	**CO**	**CH_4**	**C_2H_4**	**C_2H_6**	**C_3H_6**	**C_3H_8**	**C_4H_8**	**C_4H_{10}**	**Total C***	**TON***	**refs**
*Av*NifH [b,c]	15 mM Dithionite	37								37	0.04	22
*Av*NifH [b,c]	15 mM Dithionite/ATP	55								55	0.06	22
*Av*NifH [b,c]	15 mM Eu(II) DTPA	916								916	0.9	22
*Av*NifH [c,d]	15 mM Eu(II) DTPA	7735								7735	8	22
*Av*NifH [c,d]	15 mM Eu(II) DTPA /ATP	7605								7605	8	22
*Av*NifH [a]	100 mM Eu(II) DTPA	7934								7934	8	21
*Av*NifH^{Se} [a]	100 mM Eu(II) DTPA	4678								4678	5	66
*Ma*NifH [a]	100 mM Eu(II) DTPA	1145	1985	257	204	172	83	32	27	5053	5	21
*Av*VnfH [b,c]	15 mM Dithionite	47								47	0.05	22
*Av*VnfH [b,c]	15 mM Dithionite/ATP	61								61	0.06	22
*Av*VnfH [b,c]	15 mM Eu(II) DTPA	1127								1127	1.1	22
*Av*VnfH [c,d]	15 mM Eu(II) DTPA	7849								7849	8	22
*Av*VnfH [c,d]	15 mM Eu(II) DTPA /ATP	7556								7556	8	22

Total C refers to total nmol of reduced carbons in products per µmol cofactor. TON is expressed as described in Table 1.

[a] Assays were run for 300 min with 0.5 mg protein.

[b] Assays were run for 360 min.

[c] Assays contained 20 mg protein.

[d] Values were determined after 7 repeated additions of Eu(II) DTPA. The assay time for each repetition was 360 min.

[Fe_4S_4] center of the former representing a simplified analog of the [$NiFe_4S_4$] cluster (or C-cluster) of the latter.[9-12,22]

Unlike *Av*NifH and *Av*VnfH, the *Ma*NifH was shown to reduce CO_2 past CO into C_1-C_3 hydrocarbons, or directly reduce CO into C_1-C_4 hydrocarbons, but it was incapable of oxidizing CO to CO_2 (**Table 3**).[21] The yield of hydrocarbons generated by *Ma*NifH from CO_2 reduction increased concomitantly with a decrease in the yield of CO with increasing Eu(II) DTPA concentrations, reaching a maximum yield of 3908 nmol reduced C/μmol cluster at 100 mM Eu(II) DTPA (**Table 3**).[21] Similarly, the yield of hydrocarbons generated by *Ma*NifH from CO reduction increased with increasing concentrations of Eu(II) DTPA, reaching a maximum yield of 29359 nmol reduced C/μmol cluster at 100 mM Eu(II) DTPA (**Table 3**).[21] *Ma*VnfH, on the other hand, behaved differently than its *Ma*NifH counterpart in its reaction with C_1 substrates.[67] Contrary to *Ma*NifH, *Ma*VnfH was unable to reduce CO_2, and it reduced CO to C_1-C_4 hydrocarbons at a yield of 3114 nmol reduced C/μmol cluster in the presence of 100 mM Eu(II) DTPA, a magnitude lower than the yield of hydrocarbons generated by *Ma*NifH under the same reaction conditions (**Table 3**).

The disparate C_1 substrate reactivities of the various Eu(II) DTPA-reduced Fe proteins point to a possible difference in their abilities to access the all-ferrous $[Fe_4S_4]^0$ state for the reduction of CO_2 and CO. To address this question, the parallel-mode, g = 16.4 EPR signals of the all-ferrous *Ma*NifH and *Ma*VnfH were titrated against increasing solution potentials generated by 20 mM dithionite (E_m = –0.44 V *vs.* SHE), 2 mM dithionite (E_m = –0.47 V *vs.* SHE), 10 mM Eu(II)-DOTAM (E_m = –0.59 V *vs.* SHE), 10 mM Eu(II)-DOTA (E_m = –0.92 V *vs.* SHE) and 10 mM Eu(II)-DTPA (E_m = –1.14 V *vs.* SHE).[67] Interestingly, while the g = 1.64 EPR signals of both *Ma*VnfH and *Ma*NifH reach the maximum intensity at –1.14 V, the signal intensity of *Ma*VnfH is substantially stronger than that of *Ma*NifH at a more positive potential, with *Ma*VnfH and *Ma*NifH reaching 50% and 14.8%, respectively, of the maximum signal intensity at –0.59 V (**Figure 17**). This observation implies a more easily accessible, yet 'weaker' all-ferrous state of *Ma*VnfH at a more positive reduction potential than that accessed by its *Ma*NifH counterpart. A similar observation was made for an *Av*NifH variant containing a [Fe_4Se_4] cluster in place of the native [Fe_4S_4] cluster.[66] The Se-substituted *Av*NifH variant (designated *Av*NifH^{Se}), generated by reconstituting apo *Av*NifH with a water-soluble, synthetic $[PPh_4]_2[Fe_4S_4(SCH_2CH_2OH)_4]$

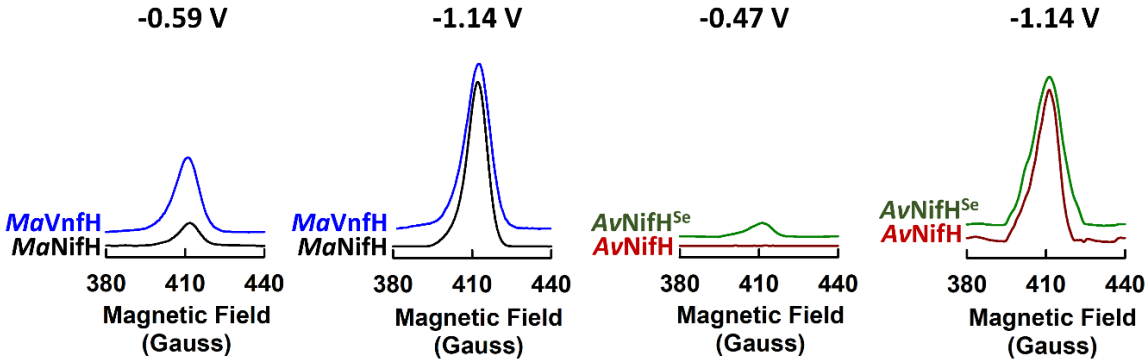

Figure 17. Variations among different Fe protein species in the redox potentials required to generate the all-ferrous state. Shown are the comparison between *Ma*VnfH and *Ma*NifH, and between Se-substituted *Av*NifH (*Av*NifH^{Se}) and wildtype *Av*NifH, in the intensities of the $[Fe_4S_4]^0$ specific, g = 16.4 EPR signal at different solution potentials (indicated on top).

compound, readily displays the parallel-mode, g = 16.4 EPR signal at a reduction potential of –0.47 V, and the appearance of such a signal can be further correlated with the ability of this protein to reduced CO_2 to CO at this potential; whereas in comparison, such a signal is absent from the EPR spectrum of its native *Av*NifH counterpart at –0.47 V (**Figure 17**) and, accordingly, reduction of CO_2 to CO by *Av*NifH cannot occur under these conditions.[66] Taken together, the C_1 substrate reactivity of the Fe protein species examined so far seems to be intimately associated with the 'pink' all-ferrous species with the characteristic g = 16.4 parallel-mode EPR signal; however, more Fe proteins need to be tested in order to substantiate this argument, particularly given the EPR-silent nature of the 'brown' all-ferrous species.

3.2. Cofactor-based Fischer-Tropsch-type reactions

As described in section 2, the cofactors can be isolated from the nitrogenase enzymes to allow characterization of their properties without the interference of the protein scaffolds. Several methods of cofactor extraction have been developed over the years,[107,159,160] with the general strategy involving denaturation of a large quantity of the catalytic component of nitrogenase with acids and organic solvents, followed by neutralization of the solution, pelleting of the denatured protein, and washing of the pellet with organic solvents prior to extraction of the cofactor with basified NMF (*N*-methylformamide), DMF (dimethylformamide) or MeCN (acetonitrile). To date,

the M- and V-clusters (**Figures 18A and B**) have been isolated from the Mo- and V-nitrogenases of *A. vinelandii*[107,143,159,160] and, although the Fe-cluster has not been isolated from the Fe-only

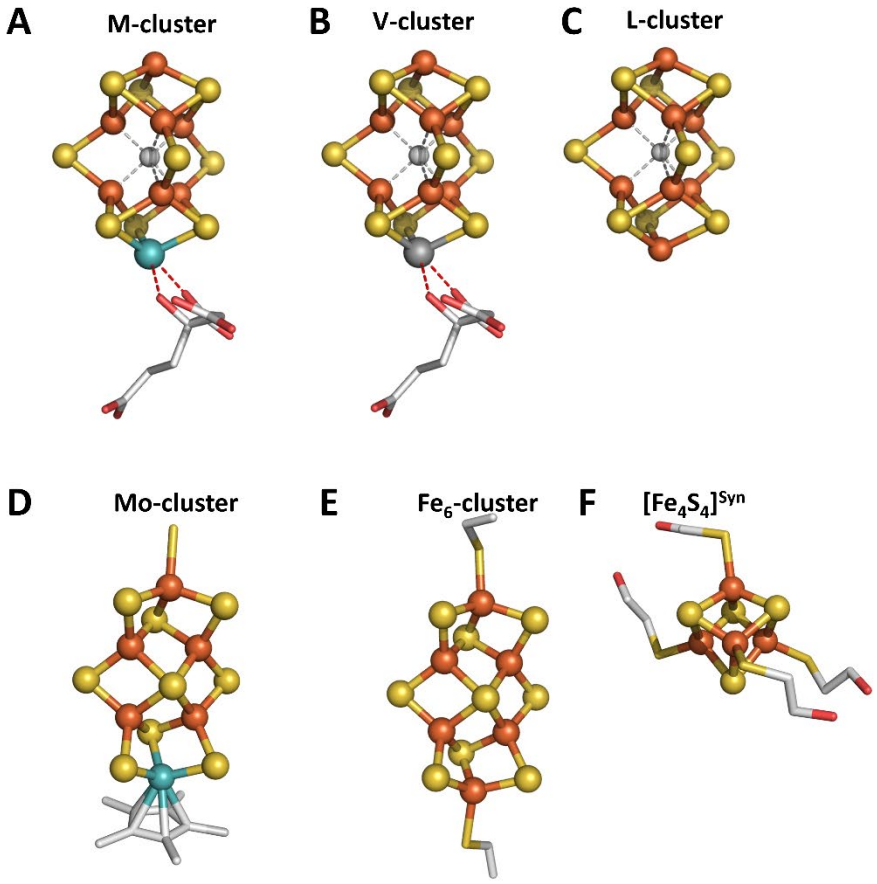

Figure 18. The native cofactors and synthetic mimics capable of reducing C_1 substrates. Shown are the biogenic (A) M-cluster ([(*R*-homocitrate)$MoFe_7S_9C$]), (B) V-cluster ([(*R*-homocitrate)VFe_7S_9C]) and (C) L-cluster ([Fe_8S_9C]) extracted from *Av*NifDK, *Av*VnfDGK and *Av*NifEN, respectively; and the synthetic (D) Mo-cluster ([Cp*$MoFe_5S_9(SH)$]$^{3-}$; Cp*, η^5-pentamethylcyclopentadienyl), (E) Fe_6-cluster ([$Fe_6S_9(SEt)_2$]$^{4-}$) and (F) $[Fe_4S_4]^{Syn}$ cluster ([$Fe_4S_4(SCH_2CH_2OH)^{4-}$).

nitrogenase of any species, a biosynthetic precursor to the M-cluster (designated the L-cluster; [Fe_8S_9C]) has been successfully isolated from a key protein involved in cofactor assembly, which closely resembles the core structure of the M-cluster and can thus be considered as a homocitrate-free, all-iron analog of the Fe-cluster (**Figure 18C**).[161] The FT-type reactivities of the native cofactors and their biogenic analog, as well as those of two high-nuclearity synthetic mimics of the nitrogenase cofactor (**Figure 18D, E**)[162,163] and a synthetic [Fe_4S_4] compound (**Figure 18F**),[21] will be discussed in detail below.

3.2.1. Solvent-extracted M-, V-, and L-clusters

In reactions driven by Eu(II)-DTPA in a Tris-HCl (pH 8) buffer, the extracted M- and L-clusters were shown to reduce CO and CN^- to C_1-C_4 hydrocarbons, with NH_3 formed alongside hydrocarbons in the reaction of CN^- reduction (**Table 4**).[27] The origin of carbon in all products were verified by GC-MS analysis using ^{13}CO or $^{13}CN^-$ as the substrate. Moreover, the stability of the isolated cofactors in this aqueous reaction mixture was established through the observation of a largely unchanged H^+-reducing activity over the course of one hour upon incorporation of the isolated cofactors into the cofactor-deficient NifDK from *A. vinelandii*. The turnover number (TON), calculated on the basis of nmol total reduced C in products per nmol cofactor, is ~0.3 for both M- and V-clusters in CO reduction; and 16 and 17, respectively, for the M- and V-clusters, in CN^- reduction (**Table 4**).[27] The comparable activities of the two cofactors in CO or CN^- reduction illustrate a 'normalizing' effect of their reactivities with C_1 substrates upon extraction into an organic solvent; whereas the considerably higher activities of the isolated M- and V-clusters in CN^- reduction than those in CO reduction, similar to those observed for the protein-bound cofactors in the respective reactions, may reflect a stabilizing effect conferred upon binding of the CN^- ion to the cofactor.[104] Interestingly, in the same aqueous, Eu(II)-DTPA driven reaction, the extracted L-cluster showed comparable activities to those of the extracted M- and V-clusters, with C_1-C_4 hydrocarbons formed at TON of 0.3 and 20, respectively, in CO and CN^- reduction (**Table 4**).[27] However, the percentages of CH_4 generated by the L-cluster from the reactions of CO and CN^- reduction were notably higher than those generated by the M- and V-clusters in the same reactions, highlighting an impact of the homocitrate ligand and the heterometal—both absent from the L-cluster—on the reactivity of the nitrogenase cofactor with C_1 substrates.

The FT-type reactivities of all three cofactor species were improved when the reactions were conducted in a triethylamine buffer system, in which 2,6-lutidinium triflate and SmI_2 were used as the respective electron and proton sources, and the solvent was substituted with dry DMF.[26] Substitution of Eu(II)-DTPA with a stronger reductant, SmI_2 ($E^{0\prime}$ = –1.55 V *vs.* SCE in tetrahydrofuran), resulted in a notable increase in the activities of CO reduction by the M-, V- and L-clusters, allowing the three cofactor species to achieve TON values of 3, 2.7 and 4.5, respectively, in C_1-C_4 hydrocarbon production, an order of magnitude higher than those accomplished by these cofactors in the Eu(II)-DTPA-driven reactions (**Table 4**).[26] Additionally, the M-, V- and L-clusters

Table 4. Activities of FT-type systems based on nitrogenase cofactors and synthetic mimics

					Products (nmol product x µmol cofactor^{-1})														
Cluster	**Sol.**	**Red.**	**H^+ Source**	**Substrate**	**CO**	**CH_4**	**C_2H_4**	**C_2H_6**	**C_3H_6**	**C_3H_8**	**C_4H_8**	**C_4H_{10}**	**C_5H_{10}**	**C_5H_{12}**	**C_6H_{12}**	**C_6H_{14}**	**Total C**	**TON**	**refs**
M	H_2O	Eu^{II}	H_2O	CO		81	50	21	18	6	7	3					335	0.34	27
M	D_2O	Eu^{II}	D_2O	CO		112	60	16	39	12	20	7					527	0.53	25,27
M	H_2O	Eu^{II}	H_2O	CN^-		379	5454	87	1278	57	245	30	101	17	51	5	17490	17	27
M	D_2O	Eu^{II}	D_2O	CN^-		333	5642	104	2831	104	650	72	351	43	196	18	26766	27	25,27
M	H_2O	Eu^{II}	H_2O	CH_2O		59400	1425	2355	67	30	10	3					67300	67	164
M	H_2O	Eu^{II}	H_2O	CH_3CHO			5050	40950		5333	1105						112420	112	164
M	DMF	SmI_2	Lut-H	CO		1297	148	365	61	102	10	27					2960	3	26
M	DMF	SmI_2	Lut-H	CN^-		7157	1592	1373	182	226	41	52					14683	15	26
M	DMF	SmI_2	Lut-H	CO_2	545	806	13	20	0.7	1							1422	1.4	26
M	DMF	SmI_2	$Et_3NH(BF_4)$	CO		149000	3000	23000	1600	4700	300	800	80	130			225350	225	162
M	DMF	SmI_2	$Et_3NH(BF_4)$	CN^-		577000	42000	56000	22000	13000	5300	2500	560	430			914150	914	162
M	DMF	SmI_2	$Et_3NH(BF_4)$	CO_2		43000	1500	7600	700	1300	90	170					68240	68	162
V	H_2O	Eu^{II}	H_2O	CO		55	46	14	13	5	5	1.4					257	0.26	27
V	D_2O	Eu^{II}	D_2O	CO		74	54	17	31	12	14	6					423	0.42	25,27
V	H_2O	Eu^{II}	H_2O	CN^-		759	4809	126	1103	42	306	29	124	11	65	4	16494	16	27
V	D_2O	Eu^{II}	D_2O	CN^-		663	4316	151	2027	88	768	63	289	32	180	13	22021	22	25,27
V	DMF	SmI_2	Lut-H	CO		1223	165	291	48	84	9	25					2667	2.7	26
V	DMF	SmI_2	Lut-H	CN^-		6173	1437	1149	143	197	51	67					12837	13	26
V	DMF	SmI_2	Lut-H	CO_2	580	1166	17	29	1.2	1.3							1846	1.8	26
V	DMF	SmI_2	$Et_3NH(BF_4)$	CO		250000	2300	20000	830	2800	140	360	46	14			307790	300	33
V	DMF	SmI_2	$Et_3NH(BF_4)$	CO_2		44000	570	3600	340	390	200	28					55442	55	33
L	H_2O	Eu^{II}	H_2O	CO		118	35	12	14	6	5	2					300	0.30	27
L	D_2O	Eu^{II}	D_2O	CO		296	74	30	44	18	12	9					779	0.78	25,27
L	H_2O	Eu^{II}	H_2O	CN^-		3401	3753	780	1068	202	320	89	159	44	67	31	19516	20	27
L	D_2O	Eu^{II}	D_2O	CN^-		5927	3734	1200	1893	453	693	191	341	102	122	74	29760	30	25,27
L	DMF	SmI_2	Lut-H	CO		2414	124	501	66	151	17	24					4479	4.5	26
L	DMF	SmI_2	Lut-H	CN^-		8276	884	1205	68	149	7	13					13185	13	26
L	DMF	SmI_2	Lut-H	CO_2	664	1523	21	40	1.7	2.3							2321	2.3	26
L	DMF	SmI_2	$Et_3NH(BF_4)$	CO		112000	2200	19000	1400	4200	220	590	30	90			175040	175	163
L	DMF	SmI_2	$Et_3NH(BF_4)$	CN^-		392000	27000	33000	16000	8100	3700	1700	650	330			610800	611	163
L	DMF	SmI_2	$Et_3NH(BF_4)$	CO_2		21000	400	2800	300	480	30	70					30140	30	163
Mo	DMF	SmI_2	$Et_3NH(BF_4)$	CO		42000	2000	7800	1100	1900	200	300	30	40			72950	73	162
Mo	DMF	SmI_2	$Et_3NH(BF_4)$	CN^-		172000	16000	19000	6400	3800	1300	700	170	120			282050	282	162
Mo	DMF	SmI_2	$Et_3NH(BF_4)$	CO_2		13000	900	2700	400	700	40	70					23940	24	162
Fe_6	DMF	SmI_2	$Et_3NH(BF_4)$	CO		49000	2700	10000	2000	2800	200	480	30	70			92020	92	163
Fe_6	DMF	SmI_2	$Et_3NH(BF_4)$	CN^-		240000	23000	24000	13000	5600	2600	1200	400	300			408500	409	163
Fe_6	DMF	SmI_2	$Et_3NH(BF_4)$	CO_2		7600	500	1500	400	400	20	80					14400	14	163
$[Fe_4S_4]^{Syn}$	H_2O	Eu^{II}	H_2O	CO		221	67	34									423	0.4	21

$[Fe_4S_4]^{Syn}$	H_2O	Eu^{II}	H_2O	CO_2		140	54	15									280	0.3	21
$[Fe_4S_4]^{Syn}$	DMF	SmI_2	$Et_3NH(BF_4)$	CO		46386	9868	2878	2748	2071	522	308					89653	90	21
$[Fe_4S_4]^{Syn}$	DMF	SmI_2	$Et_3NH(BF_4)$	CO_2		9786	1585	390	344	224	58	35					15813	16	21

Sol., solvent; Red., reductant; Eu^{II}, Eu(II) DTPA; Lut-H, 2,6-lutidinium triflate

were also capable of reducing CO_2 to CO and C_1-C_3 hydrocarbons in the presence of SmI_2, achieving TON of 1.4, 1.8 and 2.3, respectively (**Table 4**).[26] The activities of CN^- reduction by the three cofactor species, on the other hand, were comparable in the reactions driven by SmI_2 and Eu(II)-DTPA, with TON of 15, 13 and 13, respectively, achieved by the M-, V- and L-clusters, in the presence of SmI_2. Strikingly, upon substitution of Eu(II)-DTPA with SmI_2, there was a strong shift toward formation of the C_1 product (CH_4) concomitant with a decrease in the formation of $\geq C_2$ products in the reactions of CO and CN^- reduction by all three cofactor species, with the highest percentage of CH_4 formation observed for the L-cluster. Similarly, formation of C_1 products (CO and CH_4) was strongly favored by all three cofactor species in the SmI_2-driven reduction of CO_2 (**Table 4**). These observations would be consistent with a tendency of the isolated cofactors to release the reduced C_1 products instead of promoting C-C coupling when the reaction is driven by a stronger reductant.

The cofactor-based FT-type reactivity was further improved by replacing 2,6-lutidinium triflate with another proton source, triethylammonium tetrafluoroborate [$Et_3NH(BF_4)$], in the organic buffer system and optimizing other parameters of the SmI_2-driven reactions.[33,162,163] Such refinements led to dramatically increased C_1 substrate reactivities of the isolated cofactors, as well as an expansion of their product profiles. The isolated M-, V- and L-clusters achieved TON values of 225, 308 and 175, respectively, in CO reduction; and TON values of 68, 55 and 30, respectively, in CO_2 reduction (**Table 4**). The increase in the activities of these cofactor species in CN^- reduction was even more evident, with TON values of 914 and 611 achieved by the isolated M- and L-clusters, respectively (**Table 4**). The optimized reaction conditions resulted in the formation of longer hydrocarbons, allowing addition of C_5 and C_4 alkanes/alkenes, respectively, to the product profiles of CO and CO_2 reduction while showing a compensating decrease in the percentages of C_1 products (CH_4 in CO reduction; CO and CH_4 in CO_2 reduction). Nevertheless, the C_1 products remained the predominant products in these SmI_2-driven, cofactor-based FT-type reactions. Overall, all three cofactor species show similar behaviors in these reactions, although there seem to be differences originating from the presence or absence of the organic acid ligand as well as a certain heterometal in the cofactor.

The FT-type reactivity was also observed when aldehyde was supplied as a substrate to the reaction catalyzed by the isolated M-cluster.[164] Driven by Eu(II)-DTPA in an aqueous buffer, the

M-cluster was able to reduce the C_1 aldehyde (formaldehyde, CH_2O) to C_1-C_4 hydrocarbons, and the C_2 aldehyde (acetaldehyde, CH_3CHO) to C_2 and C_4 (but no C_3) hydrocarbons, suggesting that aldehydes were either fully reduced or reductively coupled into hydrocarbons in these reactions. The isolated M-cluster achieved TON of 67 and 112, respectively, in C_1 and C_2 aldehyde reduction (**Table 4**).[164] Given the considerably lower TON values achieved by the M-cluster in CO and CN^- reduction under the same reaction conditions (also see above),[25,27] the C_1 aldehyde is a much better substrate than CO and CN^- in the cofactor-based FT-type reaction. However, the reduction of all these C_1 substrates by the isolated M-cluster yielded CH_4 as the predominant product, followed by C_2 products and minor amounts of C_3 and C_4 products; similarly, the reduction of C_2 aldehyde produced C_2H_6 as the primary product, followed by C_4H_8, C_2H_4 and C_4H_{10} in a decreasing rank (**Table 4**). This observation illustrates a general preference for the complete reduction of substrates over the reductive C-C coupling in cofactor-based FT-type reactions (**Table 4**). Perhaps more interestingly, the C_1 or C_2 aldehyde could be cross-coupled with CO or CN^- by the isolated M-cluster in the presence of Eu(II)-DTPA—an activity verified by isotope labeling—yielding C_1-C_4 hydrocarbons as products of these reactions.[164] The M-cluster achieved TON values of 42 and 64, respectively, for the reactions of the C_1 aldehyde with CO and CN^-; and a TON value of 84 for the reaction of the C_2 aldehyde with either CO or CN^-.[164] Addition of CO or CN^- to the reaction of the C_1 aldehyde resulted in a shift of product distribution from CH_4 formation to C-C coupling, particularly in the case of CN^-, where CH_4, C_2H_4 and C_2H_6 were generated at an approximate molar ratio of 1:1:1; whereas the C_2 aldehyde appeared less efficient than the C_1 aldehyde in reacting/coupling with CO or CN^-, as reflected by the formation of ~70% of C_2H_6 in this reaction that was similar to that formed in the reaction containing only the C_2 aldehyde.[164] These observations point to an aldehyde-derived intermediate in the cofactor-based reduction of C_1 substrates, which could account for an improved C-C coupling upon reaction of the C_1 aldehyde with CO or CN^-, as well as a reduced efficiency in chain extension beyond C_2 as represented by the reaction of C_2 aldehyde with CO or CN^-. The identity of an aldehyde-derived intermediate(s) was further explored by isotope labeling experiments, which led to the proposal of a mechanism involving a stepwise appearance of hydroxymethyl (C_1) and hydroxyethyl (C_2) species, followed by the release of C_2H_4 as a product of β-hydride elimination of the hydroxyethyl species (see section 4 below for detailed discussion).

3.2.2. Synthetic mimics of nitrogenase-associated metalloclusters

Two synthetic high-nuclearity mimics of nitrogenase cofactors were synthesized and examined for their reactivities with C_1 substrates.[162,163] One of them, designated the Fe_6-cluster, is a homometallic, $[Fe_6S_9(SEt)_2]^{4-}$ cluster with a $[Fe_6(\mu_2\text{–}S)_6(\mu_3\text{–}S)_2(\mu_4\text{–}S)]^{2-}$ core that is topologically similar to the homometallic L-cluster (**Figure 19A**).[163] The other, designated the Mo-cluster, is a $[Cp^*MoFe_5S_9(SH)]^{3-}$ cluster (Cp*, η^5-pentamethylcyclopentadienyl) with a $[MoFe_5(\mu_2\text{–}S)_6(\mu_3\text{–}S)_2(\mu_4\text{–}S)]^{3-}$ core that is topologically similar to the asymmetric, heterometallic M-cluster (**Figure 19C**).[162] Like the native M- and L-clusters (**Figure 19B and D**), both synthetic clusters (**Figure 19A and C**) have one 'face' where Fe atoms are coordinated by μ_3 S atoms and μ_2 S atoms; however, the lack of two additional faces renders them resemblant to a partially 'collapsed' cofactor, with the unique μ_4–S atom in these synthetic clusters occupying a position similar to that of the μ_6 C^{4-} atom in the native cofactor.

In the optimized reaction system with SmI_2 and $[Et_3NH(BF_4)]$ as the respective reductant and proton sources in an organic buffer, both Fe_6- and Mo-clusters were capable of reducing CO, CN^- and CO_2 to the same set of hydrocarbons as their respective native cofactor counterparts with comparable, but lower efficiencies. [162,163] The Fe_6-cluster achieved TON of 92 and 409, respectively, for the reduction of CO and CN^- to C_1-C_5 hydrocarbons; and these values were 53% and 67%, respectively, of those achieved by the L-cluster in these reactions (**Table 4**).[163] Similarly, the TON of the Fe_6-cluster was 14 for the reduction of CO_2 to CO and C_1-C_4 hydrocarbons, 47% of that achieved by the L-cluster in the same reaction (**Table 4**).[163] Compared to the free Fe_6-cluster, the free Mo-cluster displayed TON of 73, 282 and 24, respectively, for the reduction of CO, CN^- and CO_2; and these values were 32 %, 31% and 35%, respectively, of those achieved by the M-cluster in these reactions (**Table 4**).[162] The lower C_1 reactivities of the synthetic clusters relative to those of their native cofactor counterparts could be explained by the lack of an additional μ_2 'belt sulfide'-bridged Fe pair, consequently, the absence of two Fe–S faces, the activation of which has been shown to be crucial for substrate binding and activation (also see section 4 for more discussion). Nevertheless, the synthetic clusters demonstrate a stronger preference for C-C coupling over C_1 reduction, as reflected by a higher ratio of $\geq C_2$ products to C_1 products, than the native cofactors. Moreover, the Mo-cluster was less reactive than the Fe_6-cluster with CO and CN^-, but more reactive with CO_2, despite sharing the same products and similar product profiles with its Fe_6-counterpart in all reactions. Taken together, these results point to a distinct fine-tuning

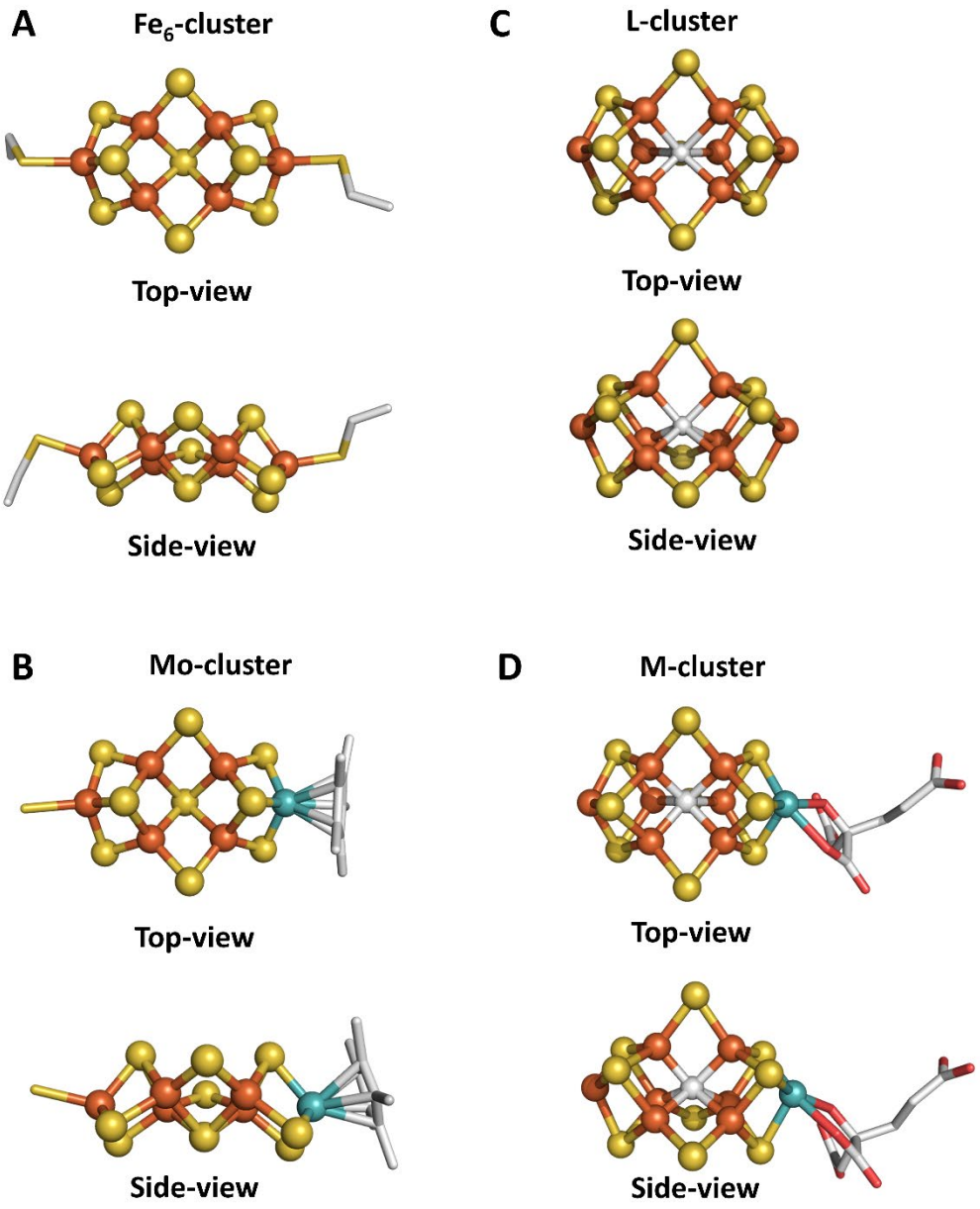

Figure 19. Comparison of the synthetic Fe_6- and Mo-clusters with the native L- and M-clusters. Shown are the top- and side-views of the crystal structures of (A) the Fe_6-cluster ($[Fe_6S_9(SEt)_2]^{4-}$); (B) the Mo-cluster ($[Cp^*MoFe_5S_9(SH)]^{3-}$; Cp*, η^5-pentamethylcyclopentadienyl); (C) the L-cluster ($[Fe_8S_9C]$; and (D) the M-cluster ([(*R*-homocitrate)$MoFe_7S_9C$]).

effect of the structure and composition of these high-nuclearity FeS clusters on their FT-type reactivities.

The observation that the FT-type chemistry can be performed without the structural elements unique to the nitrogenase cofactors, such as the interstitial C^{4-}, suggested the potential of simpler

FeS clusters to react similarly with C_1 substrates. Consistent with this suggestion, the FT-type chemistry was first observed for the biogenic $[Fe_4S_4]$ cluster associated with the nitrogenase Fe protein. Subsequently, it was demonstrated that a synthetic compound, $[PPh_4]_2[Fe_4S_4(SCH_2CH_2OH)_4]$ (**Figure 18F**), was also capable of reducing CO to hydrocarbons, and CO_2 to CO and hydrocarbons (**Table 4**).[21] Designated $[Fe_4S_4]^{Syn}$, this synthetic compound achieved noncatalytic TON of 0.3 and 0.4, respectively, in CO and CO_2 reduction when Eu(II)-DTPA was supplied as a reductant in an aqueous buffer system, and hydrocarbons of only up to C_2 in length were detected in both reactions (**Table 4**).[21] In the optimized, organic buffer system with SmI_2 and $[Et_3NH(BF_4)]$ as the electron and proton sources, however, the TON achieved by $[Fe_4S_4]^{Syn}$ increased dramatically to 90 and 16, respectively, in CO- and CO_2-reduction, and the increased activities were accompanied by an extension of the chain length of the hydrocarbon products to C_4 in both reactions (**Table 4**). Interestingly, the TON values of $[Fe_4S_4]^{Syn}$ in CO- and CO_2-reduction compare particularly well with those of the Fe_6-cluster in the same reaction systems, highlighting the similarities in the FT-type reactivities of these homometallic synthetic compounds (**Table 4**). Perhaps more importantly, theoretical calculations of the pathway of CO_2 reduction by $[Fe_4S_4]^{Syn}$ have led to the proposal of a reaction mechanism that involves an aldehyde intermediate *en route* to hydrocarbon formation (see section 4 for detailed discussion),[21] a characteristic that is shared by the cofactor-based FT-type reactions that likely routes via an aldehyde intermediate (see section 3.2.1 above for the FT-type reactivity of the isolated M-cluster with aldehyde substrates).

3.3. Whole-cell-based Fischer-Tropsch-type reactions

3.3.1. Whole-cell reactions catalyzed by the two-component nitrogenase

The ability of the two-component nitrogenase systems to reduce CO and CO_2 is not only limited to the *in vitro* conditions, but also extends to the whole-cell reactions. In the absence of ammonia, when expression of the V-nitrogenase in an *A. vinelandii* strain was upregulated, the cell culture generated C_2H_4, C_2H_6 and C_3H_8 as products of CO reduction at a TON of 750 over 8 h.[18] The whole-cell activity of CO reduction by the V-nitrogenase was further associated with nitrogenase through the observations of (*i*) predominant formation of C_2H_4, a characteristic feature of CO reduction by V-nitrogenase that was also observed under *in vitro* conditions;[15,17] (*ii*) a lack of CO-reducing activity when the cells expressing the V-nitrogenase were grown in the presence of ammonia, a condition that repressed nitrogenase expression; and (*iii*) an undetectable level of CO

reduction when the cells expressing the Mo-nitrogenase were grown in the absence of ammonia, consistent the substantially lower CO reactivity of Mo-nitrogenase relative to that of its V-counterpart under *in vitro* conditions (also see section 3.1 above). The activity of the V-nitrogenase-expressing culture to perform CO reduction could be further improved by intermittent aeration (for 20 min) between repeated intervals (4 h each) of incubation of 15% CO with the V-nitrogenase expressing culture of *A. vinelandii*—an effective measure to alleviate the cells from the inhibitory effect of CO on the respiratory chain and other key metabolic pathways—yielding a TON of 7500 after 20 repetitions of this procedure.[18] Importantly, while GC-MS experiments with ^{13}CO confirmed the origin of C in the hydrocarbon products as that from CO, nanoscale secondary ion MS analysis revealed identical $^{13}C/^{12}C$ ratios of the V-nitrogenase expressing cultures incubated with ^{13}CO and ^{12}CO. Moreover, a comparative LC-MS analysis of cultures incubated without CO and with ^{13}CO or ^{12}CO showed no incorporation of the ^{13}C label into acetyl-CoA, the central metabolite, during cell growth.[18] These observations collectively point to the whole-cell reduction of CO by nitrogenase as a secondary metabolic pathway with potential evolutionary relevance (see section 4 for detailed discussion) while suggesting a biotechnological adaptability of this process for whole-cell production of hydrocarbons from CO reduction.

Recently, an interesting strategy of whole-cell conversion of CO to C_2H_4 by *A. vinelandii* was developed on the basis of a continuous two-stage open system.[19] The first stage, conducted in a 'seed tank', involved the continuous generation of a large amount of biomass with a maximum content in V-nitrogenase. The biomass generated in the seed tank was then transferred to a 'reaction vessel', where the second stage took place upon exposure of the cells to air enriched with 5% CO, yielding 302 μg C_2H_4 per g of consumed glucose from the whole-cell reduction of CO by V-nitrogenase. This study demonstrated the necessity to overcome critical O_2 limitations for cell growth while negating the detrimental impact of respiration on the O_2-labile nitrogenase enzyme. Moreover, it illustrated an impact of excess intracellular CO as a limiting factor for cell growth and nitrogenase-based reactivity. These results provide useful parameters for further optimization of the whole-cell CO reduction by the two-component nitrogenase in the future.

Apart from the V-nitrogenase, the *in vivo* reactivity was explored for the Fe-only nitrogenase with CO_2 as the C_1 substrate. It was reported that an *R. palustris* strain expressing the Fe-only nitrogenase reduced CO_2 to CH_4 at approximately one order of magnitude higher efficiency than

the corresponding V-nitrogenase expressing strain from the same phototrophic organism, and that formation of CH_4 correlated positively with the intensity of light.[29] Isotopic labeling experiments with $H^{13}CO_3^-$ verified CO_2 as the source of C in CH_4, and the absence of CH_4 formation when the cell culture was grown in the presence of Mo—when expression of the Fe-only nitrogenase was repressed—provided support for the argument that the Fe-only nitrogenase was the origin of the whole-cell CO_2 reduction by *R. palustris*.[29] Interestingly, the cell cultures of the phototrophic *R. palustris*, *R. rubrum* and *R. capsulatus* generated 400-500 nmol CH_4 mg^{-1} total protein in the absence of ammonia and Mo, whereas the cell culture of the non-phototrophic *A. vinelandii* produced only ~6 nmol CH_4 mg^{-1} total protein under the same conditions.[29] This observation could be attributed to a general ability of the photosynthetic organisms to 'process' CO_2 better than the non-photosynthetic organisms, given the metabolic necessity of the photosynthetic organisms to perform carbon fixation—another process involving the reduction of CO_2 and incorporation of reduced C into sugars—via Calvin Cycle.

3.3.2. Whole-cell reactions catalyzed by the reductase component of nitrogenase

Conversion of CO_2 to CO was also achieved *in vivo* by *A. vinelandii* strains in which the genes encoding the catalytic component of Mo- or V-nitrogenases were deleted, thereby allowing the sole expression of their respective reductase components (NifH and VnfH) under ammonia-depleted, N_2-fixing conditions.[22] Growth of these *A. vinelandii* strains with 40% CO_2 in the absence of ammonia resulted in TON values of 140 and 110, respectively, for the strains expressing NifH and VnfH, concomitant with the observation of an upregulated expression level of the respective Fe protein.[22] In contrast, CO_2 reduction was hardly detectable when these strains were grown in the presence of ammonia, when expression of NifH or VnfH was suppressed. Interestingly, the *in vivo* activities of NifH and VnfH (up to an average TON of 10 h^{-1}) were substantially higher than those of NifH and VnfH in the *in vitro* assays (up to an average TON of 0.2 h^{-1}), likely reflecting a protective effect conferred by the reducing intracellular environment of *A. vinelandii* to the O_2-labile nitrogenase proteins, as well as the high efficiency of the physiological electron donors (*i.e.*, ferredoxins and flavodoxins) to enable the *in vivo* reduction of CO_2 to CO by the Fe protein.[22] Whether these *in vivo* electron donors support one-electron (via a $[Fe_4S_4]^{2+/1+}$ redox couple) or two-electron (via a $[Fe_4S_4]^{2+/0}$ redox couple) reduction of CO_2 to CO is an interesting topic that is worthy of further investigation.

3.4. Summary of the nitrogenase-derived Fischer-Tropsch-type reaction systems

Of all nitrogenase-derived FT-type reaction systems (**Figure 20**; **Tables 1-4**; also see sections 3.1-3.3 above), the two-component V-nitrogenase from *A. vinelandii* is the most reactive with CO (**Figure 20**; **Table 1)**; whereas the isolated cofactors (M-, V- and L-clusters) and synthetic cofactor mimics (Mo- and Fe_6-clusters) display strong reactivity with CO or CN^- in reactions driven by SmI_2 (**Figure 20; Table 4)**. For the cluster-based reactions of CO and CN^- reduction, a switch from the Eu(II)-DTPA/H_2O system to the SmI_2/solvent system results in a substantial increase in product yield, but there is a clear shift from the formation of $\geq C_2$ products toward the production of CH_4 (**Figure 20**; **Table 4)**, suggesting an overall increase in efficiency at the expense of C–C coupling and chain extension. Moreover, the efficiencies of isolated cofactors are higher than, albeit within the same order of magnitude of, those of synthetic clusters in the SmI_2-driven reactions of CO and CN^- reduction (**Figure 20**; **Table 4)**, implying the presence of more reaction sites in the structurally/compositionally more complex cofactor species than their synthetic mimics. For all systems involved, CN^- is a better substrate than CO (**Figure 20**; **Table 4)**, likely due to a higher affinity of the CN^- ion than CO to the cluster; whereas CO_2 is a considerably poorer substrate than both CN^- and CO (**Figure 20**; **Table 4)**, consistent with an increased difficulty to reduce a more oxidized C_1 substrate. The protein-based systems mainly produce CO as the product of CO_2 reduction (**Figure 20**; **Table 4)** in a reaction analogous to the water-gas-shift reaction (equation 2), though some systems are capable of producing hydrocarbons with or without CO; in comparison, the cluster-based systems demonstrate an improvement of product yield and chain extension upon optimization of the SmI_2-driven reaction system, with the isolated cofactors showing better product yield than their synthetic mimics with a compensating decrease in the production of $\geq C_2$ hydrocarbons (**Figure 20**; **Table 4)**. Collectively, these observations point to a possibility to tune the FT-type reactivity of these systems through modification of the various reaction parameters.

One such parameter is the heterometal/homocitrate 'end' of the nitrogenase cofactor (**Figures 18A and B)**. Application of the Anderson-Schulz-Flory (ASF) equation, which depicts the product distribution of FT synthesis as a plot of the logarithmic molar fraction *vs.* the carbon number, to data derived from the reactions of CO and CN^- reduction by the isolated M-, V- and L-clusters revealed a clear deviation (or decrease) of CH_4 formation from the predicted behavior in the cases

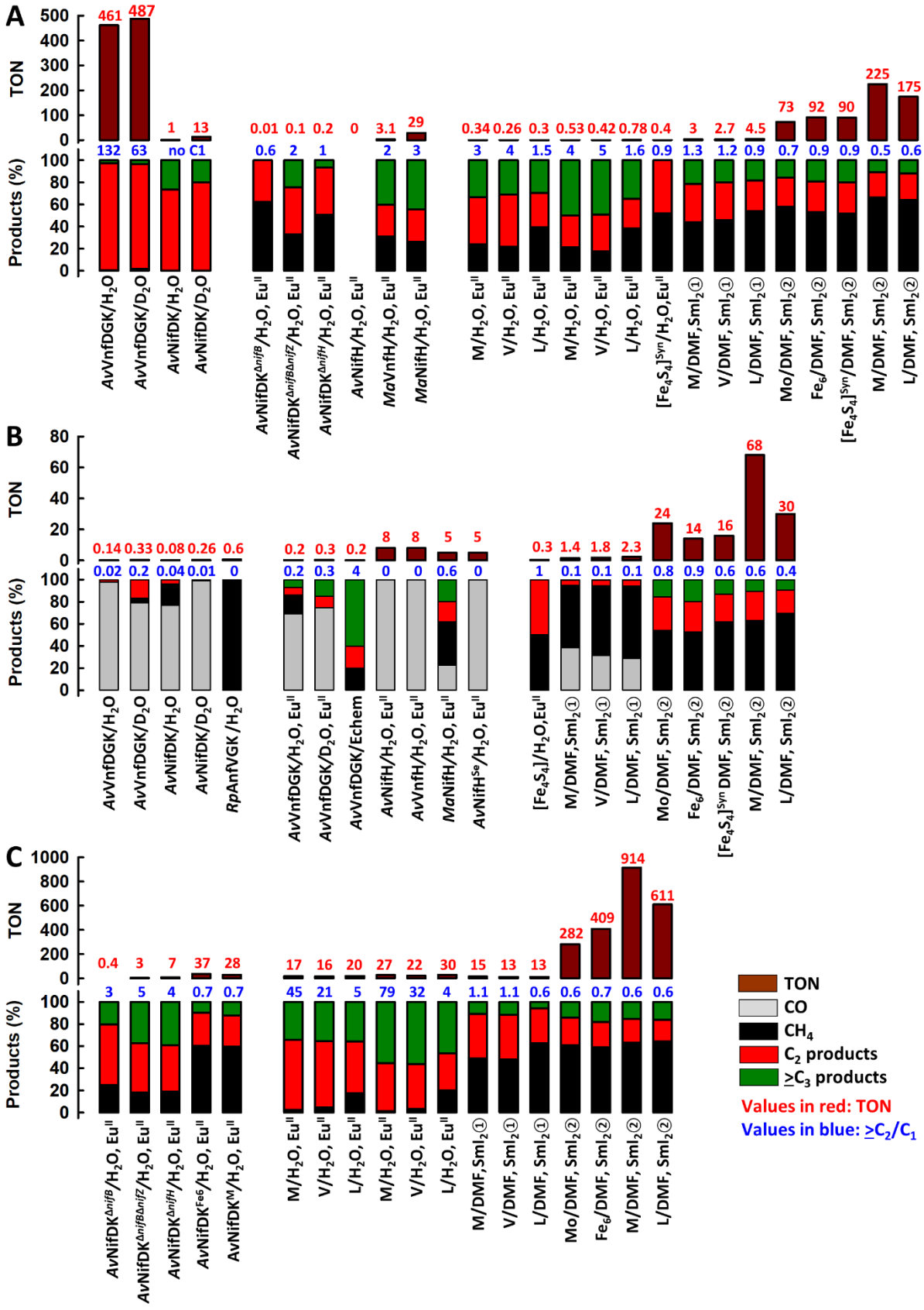
A
TON
Products (%)
461 487 1 13 0.01 0.1 0.2 0 3.1 29 0.34 0.26 0.3 0.53 0.42 0.78 0.4 3 2.7 4.5 73 92 90 225 175
132 63 no C1 0.6 2 1 2 3 3 4 1.5 4 5 1.6 0.9 1.3 1.2 0.9 0.7 0.9 0.9 0.5 0.6
AvVnfDGK/H2O
AvVnfDGK/D2O
AvNifDK/H2O
AvNifDK/D2O
AvNifDKΔnifB/H2O, EuII
AvNifDKΔnifBΔnifZ/H2O, EuII
AvNifDKΔnifH/H2O, EuII
AvNifH/H2O, EuII
MaVnfH/H2O, EuII
MaNifH/H2O, EuII
M/H2O, EuII
V/H2O, EuII
L/H2O, EuII
M/H2O, EuII
V/H2O, EuII
L/H2O, EuII
[Fe4S4]Syn/H2O,EuII
M/DMF,SmI2①
V/DMF, SmI2①
L/DMF, SmI2①
Mo/DMF, SmI2②
Fe6/DMF, SmI2②
[Fe4S4]Syn/DMF, SmI2②
M/DMF, SmI2②
L/DMF, SmI2②
B
TON
Products (%)
0.14 0.33 0.08 0.26 0.6 0.2 0.3 0.2 8 8 5 5 0.3 1.4 1.8 2.3 24 14 16 68 30
0.02 0.2 0.04 0.01 0 0.2 0.3 4 0 0 0.6 0 1 0.1 0.1 0.1 0.8 0.9 0.6 0.6 0.4
AvVnfDGK/H2O
AvVnfDGK/D2O
AvNifDK/H2O
AvNifDK/D2O
RpAnfVGK /H2O
AvVnfDGK/H2O, EuII
AvVnfDGK/D2O, EuII
AvVnfDGK/Echem
AvNifH/H2O, EuII
AvVnfH/H2O, EuII
MaNifH/H2O, EuII
AvNifHSe/H2O, EuII
[Fe4S4]/H2O,EuII
M/DMF,SmI2①
V/DMF, SmI2①
L/DMF, SmI2①
Mo/DMF, SmI2②
Fe6/DMF, SmI2②
[Fe4S4]Syn DMF, SmI2②
M/DMF, SmI2②
L/DMF, SmI2②
C
TON
Products (%)
0.4 3 7 37 28 17 16 20 27 22 30 15 13 13 282 409 914 611
3 5 4 0.7 0.7 45 21 5 79 32 4 1.1 1.1 0.6 0.6 0.7 0.6 0.6
AvNifDKΔnifB/H2O, EuII
AvNifDKΔnifBΔnifZ/H2O, EuII
AvNifDKΔnifH/H2O, EuII
AvNifDKFe6/H2O, EuII
AvNifDKM/H2O, EuII
M/H2O, EuII
V/H2O, EuII
L/H2O, EuII
M/H2O, EuII
V/H2O, EuII
L/H2O, EuII
M/DMF,SmI2①
V/DMF, SmI2①
L/DMF, SmI2①
Mo/DMF, SmI2②
Fe6/DMF, SmI2②
M/DMF, SmI2②
L/DMF, SmI2②
TON
CO
CH4
C2 products
≥C3 products
Values in red: TON
Values in blue: ≥C2/C1

Figure 20. Summary of product formation by various FT-type systems. Shown are the turnover number (TON) and product distribution (%) of hydrocarbon formed from reduction of (A) CO, (B) CO_2 and (C) CN^- by various FT-type systems (indicated at the bottom of each bar). TONs are presented in red font; the ratios between $\geq C_2$ and C_1 products are presented in blue font. Eu^{II}, Eu(II)-DTPA; $SmI_2$①, reaction with 2,6-lutidinium triflate as proton source; $SmI_2$②, reaction with $Et_3NH(BF_4)$ as proton source; Echem, electrochemically driven reaction.

of the M- and V-clusters, but a relatively minor or no deviation in the case of the L-cluster (**Figure 21**).[25] Given the structural conservation among the M-, V- and L-clusters, the notable decrease of CH_4 formation in reactions catalyzed by the M- and V-clusters relative to that in reactions

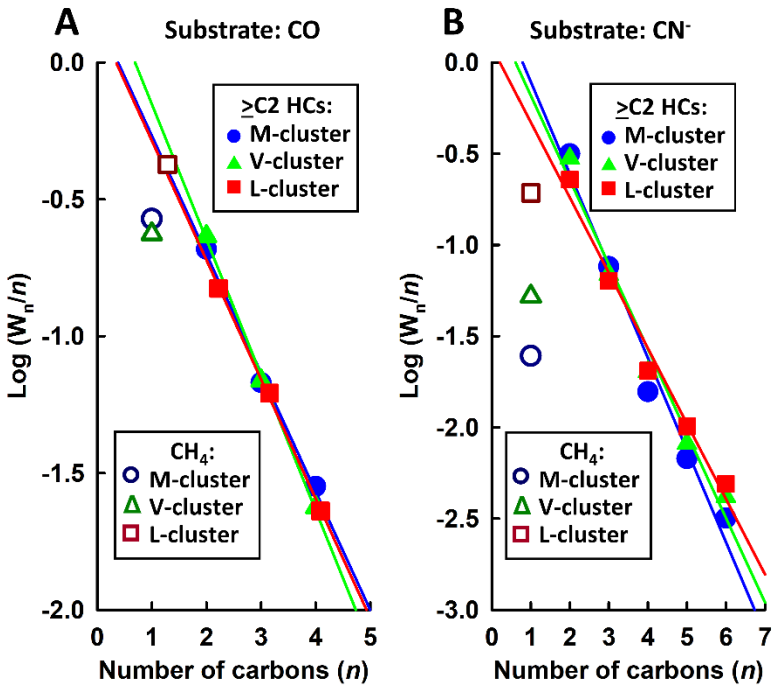

Figure 21. The Anderson-Schulz-Flory (ASF) plots of hydrocarbon formation by isolated nitrogenase cofactors. Reduction of (A) CO and (B) CN^- by the solvent-extracted M-cluster (circle), V-cluster (triangle) and L-cluster (square). There is a clear deviation in C_1-product (CH_4) formation from the linear plot in the reactions of CO and CN^- reduction by the M-cluster (open blue circle) and the V-cluster (open green triangle) (A, B); whereas there is either no deviation (A) or a relatively minor deviation (B) in CH_4 formation from the plot in the reactions of CO and CN^- reduction by the L-cluster (open brown square). The plots were generated upon a logarithmic treatment of the ASF equation: $W_n = n\alpha^n(ln_2\alpha)$, where n=number of carbons in each product, α=chain growth probability constant, and W_n=weight fraction of each product.

catalyzed by the L-cluster, concomitant with a shift toward the formation of $\geq C_2$ hydrocarbons, suggests a modulating effect of the heterometal (Mo or V) and/or the organic homocitrate ligand on the FT-type reactivity. However, the exact mechanistic differences that account for the differential FT reactivities of the M-/V-clusters and the L-cluster require further exploration.

4. Mechanism of nitrogenase-based Fischer-Tropsch-type reactions

4.1. Mechanism of the enzymatic CO reduction

The mechanism of the nitrogenase-catalyzed reduction of CO has been probed by investigating the initial binding and activation of CO at the cofactor site (section 4.1.1) and identifying the pathway and intermediates of CO reduction (section 4.1.2). A comparison of CO reduction with N_2 reduction has provided useful mechanistic insights into the FT-type reactivity of nitrogenase, which will be discussed in detail below.

4.1.1. Binding and activation of CO at the nitrogenase cofactor

4.1.1.1. Mo-nitrogenase vs. V-nitrogenase in CO binding

Several CO-bound conformations were generated for the Mo-nitrogenase from *A. vinelandii* with various CO concentrations under turnover conditions, where the reductase component (*Av*NifH) served as an obligate electron donor for its catalytic partner (*Av*NifDK) in an ATP-dependent manner.[12] Two CO-bound forms of *Av*NifDK were generated under low electron flux conditions (*e.g.*, at a NifH:NifDK ratio of 1:5): one of them, designated lo-CO, was generated with low CO concentrations (*e.g.*, <1%–8% CO in Ar); the other, designated hi-CO, was generated at high CO concentrations (*e.g.*, ≥50% CO in Ar). Incubation of NifDK with high concentrations of CO under high electron flux conditions (*e.g.*, at a *Av*NifH: *Av*NifDK ratio of 1:1) resulted in a third CO-bound species, hi(5)-CO, which was distinct from both lo-CO and hi-CO states the *Av*NifDK protein. EPR studies[165,166] revealed the characteristic features of the various CO-bound Mo-nitrogenase species, with (*i*) the lo-CO state displaying an $S = 1/2$ signal at $g = 2.10$, 1.98 and 1.92 (**Figure 22A**); (*ii*) the hi-CO state displaying an $S = 1/2$ signal at $g = 2.17$ and 2.05 (**Figure 22A**); and (*iii*) the hi(5)-CO state displaying some unique features at $g = 5.78$, 5.15 and 2.7. ^{57}Fe and ^{13}C ENDOR studies of the lo- and hi-CO states of the Mo-nitrogenase led to the proposal of one CO moiety bridged between a pair of cofactor Fe atoms in the lo-CO conformation, and two CO

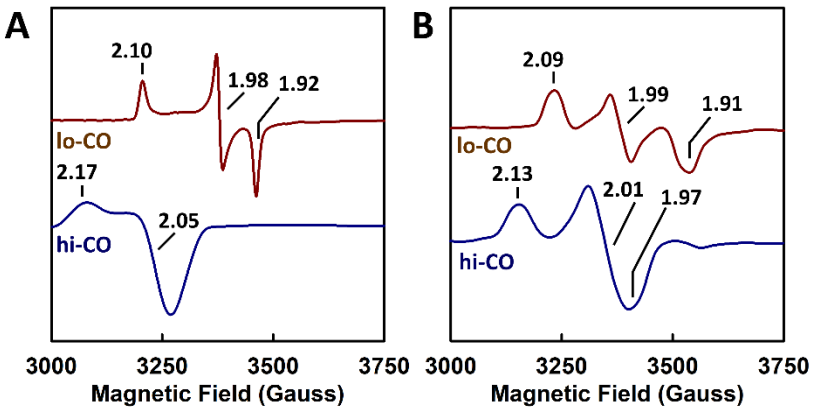

Figure 22. EPR features of the CO-bound Mo- and V-nitrogenases. EPR spectra of the lo-CO (one CO) and hi-CO (two CO) signals of (A) *Av*NifDK and (B) *Av*VnfDGK, showing certain analogy between the respective CO-bound states of the Mo- and V-nitrogenases. The *g* values are indicated.

molecules bound end-on to two different cofactor Fe atoms in the hi-CO conformation.[167-169] FTIR experiments provided further support for the proposed patterns of CO binding, revealing the presence of a single band (1904 cm^{-1}) and four bands (1904, 1906, 1936, 1958 cm^{-1}), respectively, in the spectra of the lo-CO and hi-CO states of the Mo-nitrogenase, which corresponded to binding of one and four CO molecules to the cofactor.[170] In addition, EPR and FTIR studies demonstrated an interconvertibility between the lo-CO and hi-CO states of the Mo-nitrogenase, as well as a photolytic dissociation of the CO ligands from its active-site cofactor.[166,170-173]

The lo- and hi-CO conformations could also be generated for the V-nitrogenase of *A. vinelandii*, albeit at higher CO concentrations and with limited electron fluxes, a condition generated by (*i*) using Eu(II)-DTPA instead of the reductase component (*Av*VnfH) as an ATP-independent reductant for the catalytic component (*Av*VnfDGK),[174-176] or (*ii*) pairing the catalytic component from *A. vinelandii* (*Av*VnfDGK) with a 'mismatched' reductase component from *M. acetivorans* (*Ma*VnfH).[56] When 1 atm CO (or 100% CO) was supplied to the Eu(II)-DTPA-based reaction, *Av*VnfDGK displayed an $S = 1/2$ EPR signal (g = 2.09, 1.99, 1.91) (**Figure 22B**) that was highly similar to that observed for the lo-CO signal of *Av*NifDK (**Figure 22A**).[174] When the CO concentration was increased to 2.6 atm CO, however, additional features appeared in the EPR spectrum of VnfDGK.[175] Subtraction of the lo-CO spectrum from this spectrum led to the identification of a new CO-derived species, which displayed EPR features (g = 2.13, 2.01, 1.97) (**Figure 22B**) loosely analogous to those of the lo-CO state of *Av*NifDK (**Figure 22A**).[175]

Quantification of CO released from the lo-CO and hi-CO states of *Av*VnfDGK upon acid quench yielded approximately one and four bound CO molecules per protein,[175] consistent with a previous stopped-flow FTIR study that reported 1 and 3-4 absorptions, respectively, for the lo-CO and hi-CO states of NifDK.[170] Interestingly, the same multi-CO bound form of *Av*VnfDGK could also be generated under turnover conditions at a lower CO concentration (1 atm CO) when the electron flux was substantially reduced (by 94%) by pairing *Av*VnfDGK with the 'mismatched' *Ma*VnfH in an ATP-dependent reaction, where *Av*VnfDGK displayed an indistinguishable EPR spectrum from that of the hi-CO state generated with Eu(II)-DTPA at a much higher concentration of CO (2.6 atm CO). Such an observation could be explained by the low binding affinity of the 'extra' CO molecules and an improved efficiency in the binding of these CO moieties upon reduction of the electron flux, which stalls the reaction and allows trapping of more CO molecules on the cofactor.

Despite major progress in the spectroscopic characterization of CO binding to nitrogenase, structural information of the lo-CO and hi-CO states of the *A. vinelandii* Mo-nitrogenase only became available in the recent years.[120,121] Generated under turnover conditions at 1 atm CO, the one-CO bound *Av*NifDK (designated *Av*NifDK-CO) has the CO moiety bridged symmetrically as a μ_2 ligand between Fe2 and Fe6 of the M-cluster, assuming Fe–CO distances of 1.86 Å to both Fe atoms and displacing the μ_2 belt sulfide (S2B) that normally occupies this position in the resting-state enzyme (**Figure 23A**).[121] The O atom of CO is located at distances of 2.8 and 3.4 Å, respectively, to the side chains of $His^{\alpha 195}$ and $Val^{\alpha 70}$, two key residues implicated in nitrogenase catalysis,[121] permitting hydrogen-bonding interactions between CO and $His^{\alpha 195}$ while providing added stability of CO binding via nonbonding interactions from $Val^{\alpha 70}$. The crystallographically derived binding mode of CO in *Av*NifDK-CO is highly similar to that proposed for the lo-CO state of *Av*NifDK on the basis of spectroscopic data except for the crucial observation of a missing belt sulfur (S2B) that only came to light with the structural analysis of *Av*NifDK-CO. EPR analysis of the *Av*NifDK-CO crystals dissolved in solutions provided further support for the assignment of *Av*NifDK-CO as the lo-CO species, showing the characteristic $S = 1/2$ signal of the lo-CO conformation of *Av*NifDK. Interestingly, treatment of the *Av*NifDK-CO crystals with an overpressure of CO at 5.4 atm resulted in a two-CO bound form of *Av*NifDK (designated *Av*NifDK-2CO). Consistent with the previous EPR and FTIR observations of a combination of both lo-CO features and additional features derived from the 'extra' CO moieties in the hi-CO

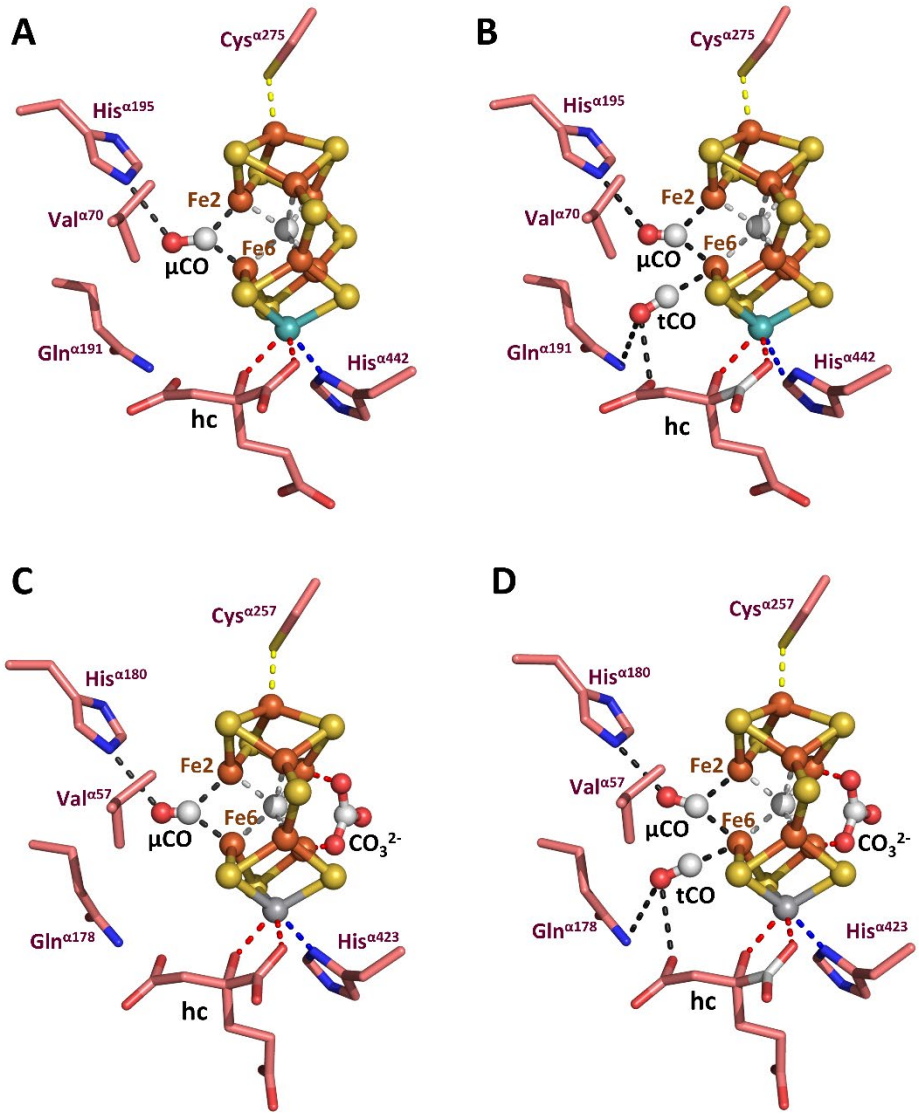

Figure 23. Crystal structures of the CO-bound cofactors in Mo- and V-nitrogenases. The one-CO (A, C) and two-CO (B, D) bound M-clusters in *Av*NifDK (A, B) and V-cluster in *Av*VnfDGK (C, D). For both *Av*NifDK and *Av*VnfDGK, binding of CO is accomplished via displacement of one belt-sulfur atom (S2B), with one CO (μCO) bridged between Fe2 and Fe6 in both one-CO and two-CO bound structures and a second CO (tCO) bound end-on to Fe6 in the two-CO bound structures. Note the displacement of another belt-sulfur (S3A) in the one-CO and two-CO bound *Av*VnfDGK structures by a carbonate (CO_3^{2-}) moiety of unknown origin. PDB entries: one-CO bound *Av*NifDK, 4TKV; two-CO bound *Av*NifDK, 7JRF; one-CO bound *Av*VnfDGK, 7ADR; two-CO bound *Av*VnfDGK, 7AIZ. The relevant protein residues are shown as sticks. The CO ligands and the clusters are shown in ball-and-stick presentation, with the atoms colored as those in Figures 3 and 11. hc, homocitrate

state, crystallographic analysis of *Av*NifDK-2CO revealed binding of one CO (designated μCO) as a μ_2 bridging ligand between Fe2 and Fe6 upon displacement of the μ_2 belt sufide (S2B), as well as binding of a second CO (designated tCO) as a terminal ligand to Fe6 (**Figure 23B**).[120] The two CO species in *Av*NifDK-2CO were subsequently correlated with the lo-CO and hi-CO states of *Av*NifDK based on the EPR spectra of the solution-state and crystal slurry of *Av*NifDK-2CO. However, the occupancies of the two CO species differ from each, with μCO and tCO modeled with 100% and 50% occupancy, respectively, in the structure, consistent with a lower binding affinity of the 'extra' CO moieties in the hi-CO state. Similar to that observed for the CO moiety in *Av*NifDK-CO, the μCO moiety in *Av*NifDK-2CO is placed at Fe–CO distances of 1.93 and 1.94 Å, respectively, to Fe2 and Fe6, and it is located in close proximity to $His^{\alpha 195}$ and $Val^{\alpha 70}$ to allow hydrogen-bonding and non-bonding interactions with the respective side chains of these residues. The tCO moiety in *Av*NifDK-2CO, on the other hand, has its C atom located at distance of 2.03 Å to Fe6, and its O atom located at approximately 3.3 and 2.7 Å, respectively, to the amide N of $Gln^{\alpha 191}$ and a carboxylic acid group of *R*-homocitrate. Binding of this 'extra' CO causes a slight elongation of the distance between μCO and Fe6 from 2.01 Å in *Av*NifDK-CO to 2.06 Å in *Av*NifDK-2CO.

Consistent with the biochemical and spectroscopic observations of analogous CO-bound states of the Mo- and V-nitrogenases, the crystal structures of the one-CO and two-CO-bound forms of the V-nitrogenase from *A. vinelandii* (**Figures 23C and D**)[122,123] are highly analogous to their respective counterparts of the Mo-nitrogenase from the same organism (**Figure 23A and B**).[120,121] Like the one-CO-bound *Av*NifDK (*Av*NifDK-CO), the one-CO *Av*VnfDGK (designated *Av*VnfDGK-CO) has a CO molecule bound as a μ_2 bridging ligand between Fe2 and Fe6; however, unlike the symmetric binding of CO in its *Av*NifDK-CO counterpart, the CO moiety in *Av*VnfDGK-CO is slightly asymmetric, with CO located at Fe-CO distances of 2.03 and 1.94 Å, respectively, to Fe2 and Fe6 (**Figure 23C**). Additionally, CO interacts with $His^{\alpha 180}$ and $Val^{\alpha 57}$ at Fe–CO distances of 2.9 and 3.6 Å, respectively, in *Av*VnfDGK-CO, analogous to the interactions of CO with $His^{\alpha 195}$ and $Val^{\alpha 70}$ in *Av*NifDK-CO. Application of an overpressure of CO to the crystals of *Av*VnfDGK-CO, like that to the crystals of *Av*NifDK-CO, resulted in a two-CO-bound form of *Av*VnfDGK (designated *Av*VnfDGK-2CO); only in the case of *Av*VnfDGK-2CO, a lower overpressure of CO (1.5 atm) was applied than that used to generate *Av*NifDK-2CO (5.4 atm CO). As observed for its *Av*NifDK-2CO counterpart, *Av*VnfDGK-2CO has one CO (μCO; modeled at

100% occupancy) bound as a μ_2 bridging ligand between Fe2 and Fe6, and a second CO (tCO; modeled at 50% occupancy) bound terminally to Fe6, with the O atm of tCO positioned at approximately 3.1 and 2.9 Å, respectively, to the amide N of $Gln^{\alpha 176}$ and a carboxylic acid group of *R*-homocitrate (**Figure 23D**). Notably, the Fe6-C distance of tCO in *Av*VnfDGK-2CO (1.89 Å) is shorter than that of tCO in *Av*NifDK-2CO (2.03 Å), indicating a stronger binding of the second CO in *Av*VnfDGK-2CO.

The observation of nearly identical CO-bound conformations of the Mo- and V-nitrogenases and, particularly, the catalytically relevant lo-CO conformations (see section 4.1.1.2 for more discussion), is interesting given that these structurally high similar species differ drastically in their abilities to reduce CO to hydrocarbons (see section 3.1.1 above). As the immediate protein surroundings of the bound CO moieties are highly similar in the Mo- and V-nitrogenases, it is likely that other factors contribute primarily to their differential FT-type reactivities. One factor to consider is the impact of different heterometals (Mo *vs.* V) on the catalytic properties of the respective cofactors (M-cluster *vs.* V-cluster) in the two homologous nitrogenases. This argument is supported by a parallelism between the abilities of Mo/V nitrogenases to reduce CO to hydrocarbons and the abilities of synthetic Mo/V compounds to reductively couple two CO moieties into functionalized acetylene ligands, and a better efficiency of V (a group VB transition metal) than Mo (a group VIB transition metal)—as suggested in the latter case—in C_1 substrate activation. Another factor that could contribute to the differential CO reactivities is the presence of distinct P-cluster species in the two homologous enzymes, with the P-cluster in Mo-nitrogenase having a fused, $[Fe_8S_7]$ architecture and its counterpart in V-nitrogenase adopting a more modular, paired $[Fe_4S_4]$-like conformation. Such a difference could impact the efficiency of electron transfer to the cofactor and, consequently, poise the cofactors of the Mo- and V-nitrogenases at different redox states for substrate reduction. Recently, a crystallographic study of an N_2-bound form of Mo-nitrogenase revealed an asymmetric displacement of all three belt sulfurs in the two cofactors of *Av*NifDK,[88] leading to the proposal of a mechanism that involves stepwise reduction of N_2 at the three belt-sulfur sites via an asynchronous cluster rotation of the two cofactors (see section 4.1.1.3 below for more discussion).[88,89,177] The observation of CO binding at a single belt-sulfur (S2B) displaced site in both cofactors of *Av*NifDK, therefore, points to the possibility that CO is 'stuck' at the S2B site and, consequently, the CO-bound conformation is 'synchronized' in the two cofactors, an argument consistent with the relative ease to trap CO compared to N_2 at the cofactor.

In this context, it is plausible that the cofactors in Mo- and V-nitrogenases differ in their abilities to rotate past the S2B site and, as a result, they differ in their overall activity and product distribution in the reaction of CO reduction (see section 4.1.1.3 below for more discussion). More work is required to test this hypothesis.

4.1.1.2. lo-CO versus hi-CO

The spectroscopic and structural observations of various CO-bound species in both Mo- and V-nitrogenases led to the question of which species was catalytically competent for the reduction and coupling of CO into hydrocarbon products of various chain lengths. In particular, the lo-CO and hi-CO states seem to be the perfect candidates for initiating a full reduction of CO to CH_4 (lo-CO) and enabling a reductive C-C coupling between two CO moieties into $\geq C_2$ hydrocarbons (hi-CO). The possibility to generate the lo-CO state of *Av*VnfDGK with a chemical reductant, Eu(II)-DTPA, in the absence of *Av*VnfH, provided a unique platform to uncouple binding of CO from its subsequent turnover with or without externally supplied CO, thereby allowing assessment of the catalytically relevant CO species on the basis of the origin of C in the hydrocarbon products.[175] When the lo-^{13}CO state of *Av*VnfDGK was prepared by re-isolating the protein after incubation with ^{13}CO in Eu(II)-DTPA, and subsequently subjecting the re-isolated protein to turnover (*i.e.*, with VnfH, ATP and reductant) in the absence of CO, $^{13}CH_4$ was detected as the sole product of this reaction (**Figure 24A**).[175] Incubation of the lo-^{13}CO state of *Av*VnfDGK with additional ^{12}CO under turnover conditions, on the other hand, resulted in the formation of C_2 hydrocarbons with mixed labels (*i.e.*, $^{12}CH_2{=}^{13}CH_2$, $^{12}CH_3$-$^{13}CH_3$) (**Figure 24B**).[175] These observations establish the catalytic relevance of the lo-CO state in CO reduction and coupling. In contrast, no C_2 products were detected when the two-^{13}CO bound, hi-^{13}CO state of *Av*VnfDGK was subjected to turnover in the absence of CO (**Figure 24C**).[175] Incubation of the hi-^{13}CO state of *Av*VnfDGK with additional equivalents of ^{12}CO yielded C_2 hydrocarbons with mixed labels (*i.e.*, $^{12}CH_2{=}^{13}CH_2$, $^{12}CH_3$-$^{13}CH_3$), but not with uniform ^{13}C labels (*i.e.*, $^{13}CH_2{=}^{13}CH_2$, $^{13}CH_3$-$^{13}CH_3$) (**Figure 24D**),[175] like that observed when the lo-^{13}CO state of *Av*VnfDGK was incubated with additional ^{12}CO (**Figure 24B**). These results exclude the two adjacent CO moieties in the hi-CO state from being catalytically relevant for C-C bond formation, a conclusion that is consistent with the theoretical suggestions and experimental observations that an aldehyde-derived intermediate—possibly

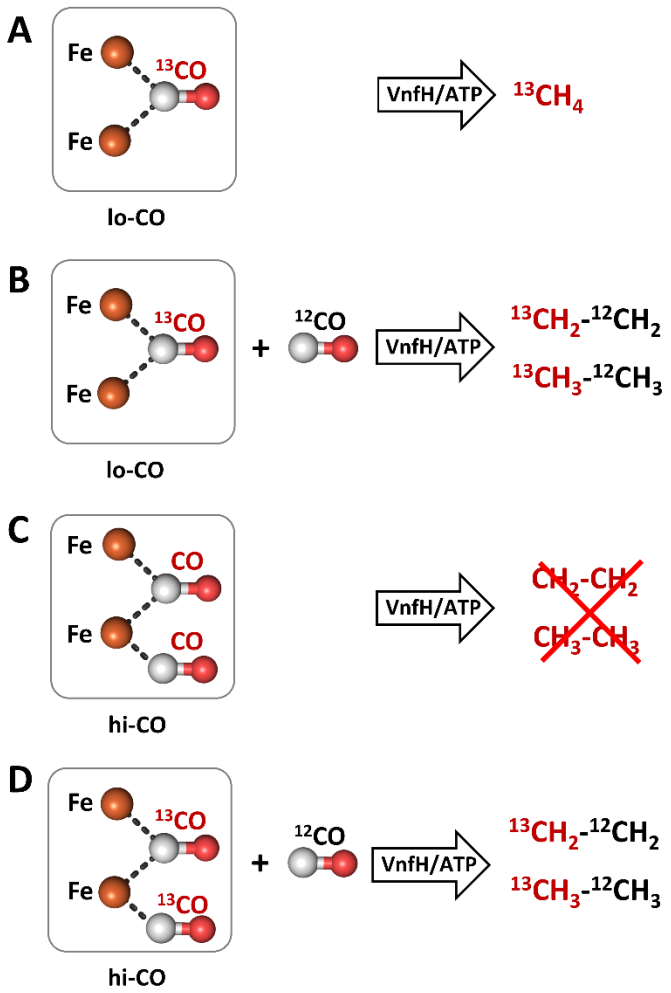

Figure 24. Catalytic relevance of the lo-CO and hi-CO states. Schematic illustration of C_2 product formation when lo-^{13}CO *Av*VnfDGK is subjected to turnover in the absence (A) or presence (B) of ^{12}CO; and (C) when hi-^{12}CO *Av*VnfDGK is subjected to turnover in the absence of ^{12}CO, or (D) when hi-^{13}CO *Av*VnfDGK is subjected to turnover in the presence of ^{12}CO.

derived from C-C coupling between CO and a more reduced C moiety than CO—is responsible for the formation of C_2 hydrocarbon along the pathway of CO reduction (see section 4.1.2 below).

The catalytic competence of the lo-CO state is particularly intriguing given the unprecedented structural observation of CO binding via displacement of a μ_2 belt sulfide (S2B). It was proposed that release of S2B would open up a reactive diiron face of the cofactor for the binding and activation of CO, and that the same mechanism could be extended to the binding and activation of N_2.[121] Such a concept, alongside DFT calculations[178] and structural observations of belt-sulfur displacement in both Mo- and V-nitrogenases upon binding of CO (**Figure 23**)[120-123] or N_2 (**Figure**

25)[88,89] under turnover conditions,[88,89,120-123,179] provided a new perspective on the mechanistic thinking of nitrogenase. Moreover, based on the close proximity of His$^{\alpha195}$ to the CO moiety at the

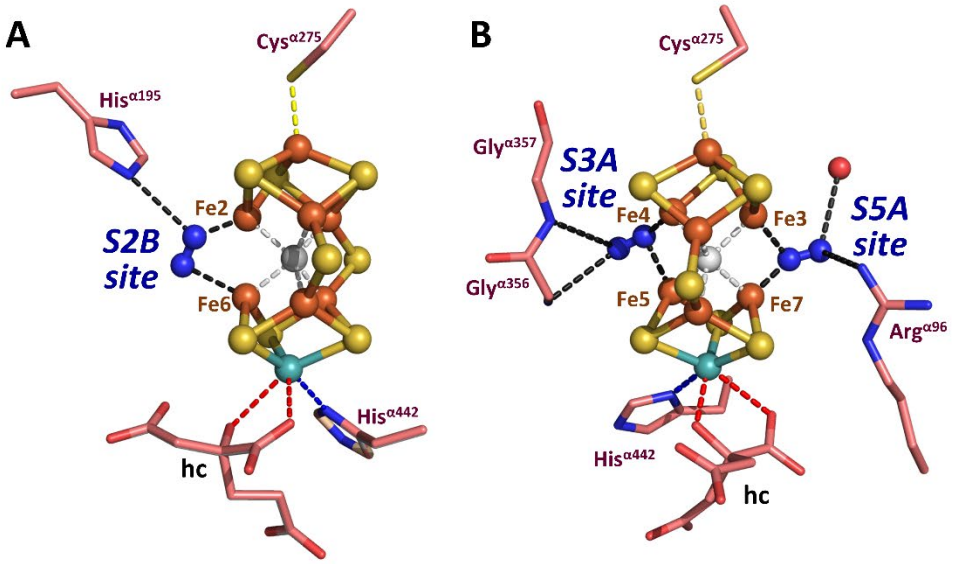

Figure 25. Crystal structures of the two cofactors of Mo-nitrogenase with asymmetric N_2 binding. (A) The M-cluster in one αβ-dimer of the N_2-bound *Av*NifDK (*Av*NifDK-N_2) has a dinitrogen species displacing one belt-sulfur (S2B) and bound in a pseudo $\mu_{1,2}$-bridging mode between Fe2 and Fe6; and (B) the M-cluster in the other αβ-dimer of *Av*NifDK-N_2 has two dinitrogen species displacing two belt-sulfurs (S3A and S5A) and bound as asymmetric $\mu_{1,1}$-ligands bridged between Fe4 and Fe5 (at the S3A site) and between Fe7 and Fe3 (at the S5A site), respectively (PDB entry 6UG0). Accompanying the asymmetric N2 binding is the asymmetric elongation of (A) Mo–O5 (carboxyl) or (B) Mo–O7 (hydroxyl) distance to 2.7 Å that switches Mo–homocitrate ligation from bidentate to monodentate. The relevant protein residues are shown as sticks. The N_2 ligands and the clusters are shown in ball-and-stick presentation, with the atoms colored as those in Figures 3 and 11. hc, homocitrate

S2B site of *Av*NifDK-CO and the reappearance of S2B upon turnover of *Av*NifDK-CO in the absence of CO, further argument was made for the generation of an HS^- leaving group via protonation of S2B by the nearby His$^{\alpha195}$, which allowed binding of CO at the vacant S2B site concomitant with 'migration' of the HS^- group to a distant sulfur binding pocket (situated ~22 Å away from the S2B location), followed by 'return' of the same sulfur species to the S2B site upon dissociation of CO under turnover conditions.[121] A similar mechanism was proposed for *Av*VnfDGK, with binding of CO facilitated by displacement of S2B via protonation by a nearby His$^{\alpha180}$ residue, and release of CO accompanied by return of sulfur from a putative binding pocket (located ~7 Å away) back to the S2B site.[123] The lability of the cofactor belt region during catalysis was further verified by crystallographic[124] and XAS/EXAFS[89] pulse-chase experiments wherein

the Mo-nitrogenase was first labeled with Se at the cofactor belt sulfur site(s) and subsequently subjected to turnover with substrates; however, using the more efficient substrates than CO (*i.e.*, C_2H_2 and N_2), these experiments demonstrated an exchangeability and involvement of all three belt sulfurs during catalysis[89,124] while pointing to the use of a general sulfur 'pool' for the restoration of a belt-sulfur-replete cofactor conformation instead of having the same sulfur tunneling back to the belt sulfur site from the putative sulfur binding pocket (see section 4.1.1.3 below for more discission).[89]

4.1.1.3. CO binding versus N_2 binding

Given the isoelectronic nature of CO and N_2, a comparison of the binding and activation of CO and N_2 by nitrogenase is particularly relevant to the mechanistic consideration of nitrogenase. Recently, an N_2-bound form of Mo-nitrogenase was obtained by isolating NifDK from an N_2-fixing culture of *A. vinelandii* under strict anaerobic conditions, but in the absence dithionite, which allowed capture of dinitrogen species at the cofactors of *Av*NifDK upon exhaustion of the electron supply. Contrary to the observation of CO binding at a singular belt sulfur (S2B) site in both cofactors of *Av*NifDK-CO, crystallographic analysis of this N_2-bound *Av*NifDK (designated *Av*NifDK-N_2) revealed an asymmetric binding of three N_2-derived species to the two cofactors via belt-sulfur displacement, with one of them bound at the S2B site of the M-cluster in one αβ-dimer (**Figure 25A**)[88] and the other two bound at the S3A and S5A sites of the M-cluster in the second αβ-dimer (**Figure 25B**).[88] The displacement of belt sulfurs at the S2B, S3A and S5A sites of *Av*NifDK-N_2 was verified by the absence or substantial decrease of anomalous electron densities at these positions, as well as a 'return' of sulfurs to these locations upon turnover of *Av*NifDK-N_2 in the presence of *Av*NifH, ATP and dithionite (a sulfur-containing reductant); yet, electron densities were clearly detected at these belt sites in the native electron density map, and best fits of the structural data led to the assignment of three N_2 units displacing the respective belt sulfurs in the two different cofactors of *Av*NifDK-N_2.

At the S2B site, the N_2 moiety adopts a pseudo $\mu_{1,2}$-bridging mode between Fe2 and Fe6, with one N atom (N6A) placed at a distance of 1.8 Å from Fe2, and the other N atom (N6B) located at a distance of 2.3 Å from Fe6. Notably, N6A is positioned at a distance of 2.9 Å to $His^{\alpha 195}$ (**Figure 25A**), thereby permitting a hydrogen-bonding interaction between N_2 and $His^{\alpha 195}$ in *Av*NifDK-N_2 that is similar to that between CO and $His^{\alpha 195}$ in *Av*NifDK-CO. At the S3A and S5A sites of

*Av*NifDK-N_2, where CO binding was not observed in *Av*NifDK-CO, two N_2 moieties could be modeled as asymmetric $\mu_{1,1}$-ligands bridged between Fe4 and Fe5 (at S3A) and between Fe7 and Fe3 (at S5A), respectively (**Figure 25B**). In both cases, the proximal N atoms are positioned at a distance of 1.8 Å to one Fe atom (Fe4 at S3A; Fe7 at S5A) and a distance of 2.1 Å from the other Fe atom (Fe5 at S3A; Fe3 at S5A); whereas the distal N atoms interact with the respective backbone amide groups of $Gly^{\alpha 356}$ and $Gly^{\alpha 357}$ at 2.9 and 3.4 Å (at S3A) and with the side chain of $Arg^{\alpha 96}$ and a nearby water molecule at 3.2 and 3.0 Å (at S5A). Interestingly, the asymmetric binding of N_2 in the two cofactors is accompanied by the elongation of either the Mo–O5 (carboxyl) or Mo–O7 (hydroxyl) distance to 2.7 Å that switches Mo–homocitrate ligation from bidentate (in *Av*NifDK-CO and the resting-state *Av*NifDK) to monodentate (in *Av*NifDK-N_2). Such an elongation of Mo–O distances could result from protonation, an argument supported by the previous proposal that the homocitrate ligand of the cofactor is involved in proton transfer during catalysis.[180-182]

Consistent with the presence of bound N_2 species, acid quench of *Av*NifDK-$^{15}N_2$ isolated from an $^{15}N_2$-grown culture resulted in the release of $^{15}N_2$.[88,89] Moreover, the C_2H_2-reduction assay catalyzed by *Av*NifDK-N_2 in the presence of D_2, but not N_2, resulted in the formation of C_2H_3D.[89] Given that formation of deuterated C_2H_4 could only have occurred via displacement of the cofactor-bound/activated N_2 species by D_2-derived deuterides (D^-), followed by incorporation of the D label into the product of C_2H_2 reduction,[89,183-187] this observation provides compelling evidence for the binding of N_2 in a catalytically competent state in *Av*NifDK-N_2. In agreement with this assessment, frequency-selective NMR analysis demonstrated formation of $^{15}NH_4^+$ upon single turnover of *Av*NifDK-$^{15}N_2$, firmly establishing the catalytic relevance of the N_2-bound conformation in this NifDK species. [89] Additionally, EPR characterization of *Av*NifDK-N_2 revealed a decrease in the intensity of the characteristic $S = 3/2$ signal of the resting-state cofactor (**Figure 26A**)[89] by ~50% concomitant with a slight broadening of the lineshape of this signal to yield g values of 4.32 and 3.66 in the $S = 3/2$ region of the spectrum (**Figure 26B**).[89] Perhaps more interestingly, three new EPR features appeared in the $S = 1/2$ region of the spectrum of *Av*NifDK-N_2 at $g = 2.22$, 2.01 and 1.88, with the features at $g = 2.22$ and 1.88 showing a different temperature dependency than that at $g = 2.01$ (**Figure 26B**).[89] These results have lent additional support to the structural observation of binding of multiple N_2 species to the cofactors in *Av*NifDK-N_2. Interestingly, an analogous conversion of the EPR signal was also observed upon binding of CO

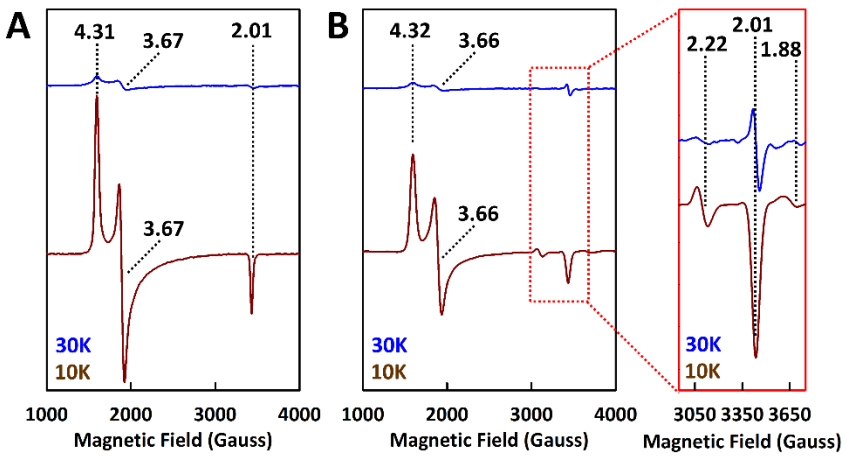

Figure 26. EPR spectra of the N_2-free and N_2-bound Mo-nitrogenase. Shown are the EPR spectra of (A) the resting-state *Av*NifDK and (B) the N_2-bound *Av*NifDK, showing a reduction in the magnitude of the $S = 3/2$ signal of the resting-state cofactor by ~50% concomitant with the appearance of three new features at $g = 2.22$, 2.01 and 1.88 upon binding of N_2 (inset). Note that the feature at $g = 2.01$ has a different temperature dependency than those at $g = 2.22$ and 1.88.

to NifDK (see section 4.1.1.1 above), consistent with a broad similarity in the binding of CO and N_2 via displacement of belt sulfur(s).

Surprisingly, while substrate turnover was successfully accomplished upon incubation of *Av*NifDK-N_2 with NifH, ATP and dithionite, no product could be detected when dithionite was replaced by Eu(II)-EGTA, a sulfur-free reductant, in the same reaction.[89] This observation points to a dual role of dithionite in supplying electrons and sulfurs that are required for nitrogenase catalysis. Consistent with this suggestion, turnover of *Av*NifDK-N_2 with dithionite in the absence of any substrate other than H^+ resulted in a restoration of all belt sulfurs at the respective sulfur-displaced sites, [89] suggesting a connection between belt-sulfur insertion and product release. Subsequent biochemical analysis led to the identification of sulfite (SO_3^{2-})—a breakdown product of the *in vitro* reductant, dithionite, as well as a central 'hub' of *in vivo* sulfur metabolism[89]—as a competent sulfur source to drive product formation by *Av*NifDK-N_2 when in the presence of a sulfur-free reductant, Eu(II)-EGTA; whereas crystallographic and EPR analyses supplied further evidence for the incorporation of SO_3^{2-} as belt S^{2-} upon turnover *Av*NifDK-N_2 with SO_3^{2-} and Eu(II)-EGTA, rendering a belt-sulfur-replete conformation that was indistinguishable from generated upon turnover of *Av*NifDK-N_2 in the presence of dithionite. [89] Subsequent Fe and Se

XAS/EXAFS experiments revealed a dynamic mobilization of belt-sulfurs during catalysis, showing incorporation of SeO_3^{2-} as Se^{2-} into the cofactor belt region upon turnover of *Av*NifDK in the presence of NifH, ATP, SeO_3^{2-} and Eu(II)-EGTA, and the subsequent displacement of belt-Se by belt-S upon turnover of Se-labeled *Av*NifDK upon substitution of SO_3^{2-} for SeO_3^{2-}.[89] A similar observation was made in a previous crystallographic pulse-chase study, wherein a selenocyanate ($CNSe^-$) label was first incorporated at the S2B position of *Av*NifDK and subsequently chased off upon turnover in the presence of dithionite.[124]

The observation of an asymmetric binding of N_2 via belt-sulfur displacements in the two cofactors, coupled with that of a dynamic mobilization of all belt sulfurs during catalysis, led to the proposal of a mechanism involving an asynchronous rotation of the two cofactors that permits the same, stepwise reduction of N_2 at the three belt-sulfur sites to occur a step apart in the two αβ-dimers of *Av*NifDK (**Figure. 27**).[88,89] In this model, the stepwise reduction of N_2 begins with binding of N_2 at the S3A site via belt-sulfur displacement, followed by cluster rotation that brings N_2 to the S2B site for the initial reduction to a diazene-level species. Subsequent cluster rotation brings the diazene-level intermediate to the S5A site for further reduction to ammonia, which signals binding of the next N_2 to the S3A site via belt-sulfur displacement, followed by release of ammonia from the S5A site via a refill of the belt-sulfur, and continued cluster rotation that brings the next N_2 from the S3A site to the S2B site for the next round of N_2 reduction. The asynchronous rotation of the two cofactors, on the other hand, could be facilitated by alternate docking of NifH on the two αβ-dimers of NifDK. Docking of NifH on one αβ-half supplies ATP-derived energy for the rotation of the cofactor, which is facilitated by the breakage of one Mo–O bond; whereas in the αβ-half that is free of NifH, the cofactor is 'idling' in one place, which allows a certain reduction step to occur at a particular belt site (**Figure 7**).[88,89] Excitingly, a recent cryo-EM study of the Mo-nitrogenase from *A. vinelandii* revealed formation of a 1:1 complex between *Av*NifH and *Av*NifDK under turnover conditions, as well as unresolved electron density at the Mo/homocitrate end of the cofactor structure.[110] These observations provide strong support for the proposed alternate binding of *Av*NifH to the two αβ-halves of *Av*NifDK that would result in a 1:1 complex between *Av*NifH and *Av*NifDK at all times, as well as a rotation of the cofactor during catalysis via a dynamic change of the Mo–O distances that could contribute to the unresolved electron densities at the Mo/homocitrate end of the cofactor.

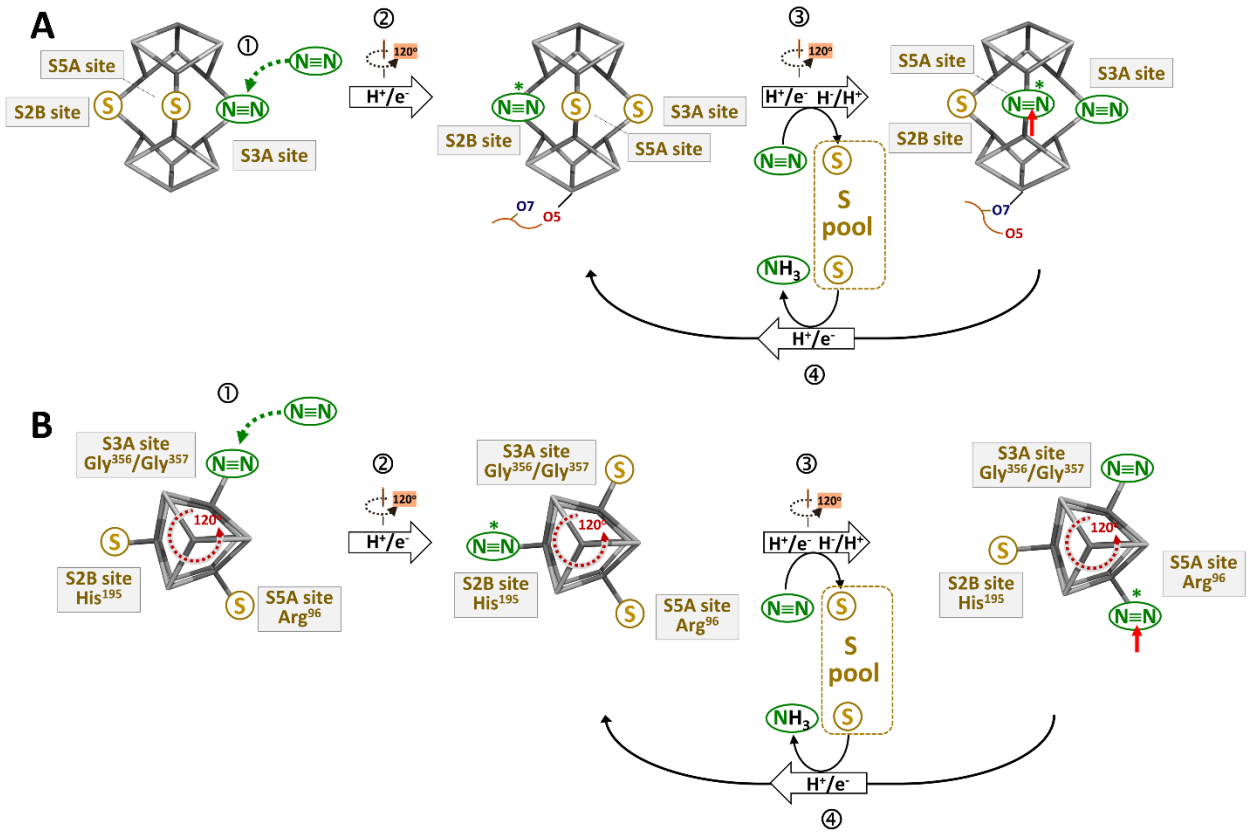

Figure 27. Proposed mechanism of stepwise reduction of N_2 via cofactor rotation. (A) Side view and (B) top view of binding of N_2 at the S3A site via sulfur displacement (①), followed by cluster rotation and reduction of N_2 at the S2B site to a diazene-level species (②), prior to cluster rotation and reduction of the diazene-level species at the S5A site to ammonia (③). The final reduction step at S5A signals binding of the next N_2 to the S3A site via sulfur displacement (④), followed by release of ammonia from the S5A site via a refill of the belt-sulfur, as well as cluster rotation, which brings the next N_2 from the S3A site to the S2B site for the next rounds of N_2 reduction.

While displacement of belt sulfurs at positions other than S2B was not observed in the structure of *Av*NifDK-CO or *Av*VnfDK-CO (**Figure 23**), a similar mechanism of CO reduction could be contextualized in light of a potential involvement of all belt sulfur sites in substrate reduction. It is plausible that CO reduction begins with binding of CO at the S3A site, followed by rotation of the cofactor and subsequent reduction of CO and release of product at the S2B and S5A sites; however, the reaction is largely stalled at the S2B site, which appears to be a thermodynamic sink for CO binding and, consequently, the lo-CO conformation is accumulated and 'synchronized' at the two cofactor sites at the expense of the catalytic efficiency that relies on continued cofactor rotation past the S2B site. While this hypothesis requires experimental support, the observation of binding

of CO_3^{2-} moiety at the S3A site in the CO-bound V-nitrogenase implies the feasibility to have CO bound at the S3A site as the entry point into the reaction, similar to that proposed for the initial binding of substrate at the S3A site in N_2 reduction. Moreover, the differential abilities of Mo- and V-nitrogenases in CO reduction could be explained by CO being more 'stuck' at the S2B site of the M-cluster than that at the S2B site in the V-cluster, which could account for the lower activity and different product profile of Mo-nitrogenase than its V-counterpart in CO reduction. The experimentally observed lack of a switch between the C_2 and C_3 stages of CO reduction from an alkene:alkane ratio of >1 to one that is <1 upon substitution of the reductase component of V- or Mo-nitrogenase with a chemical reductant further implies a mechanistic difference between the two-component system and the one-component/cluster-based system, with the former potentially utilizing (at least in part) the cluster rotation mechanism for CO reduction and the latter likely working independently of such a mechanism. Clearly, the mechanistic details of the nitrogenase-based FT-type reactions require further exploration by biochemical, structural, spectroscopic, and theoretical approaches.

Recently, a study was conducted with a nitrogenase hybrid containing *Av*VnfDGK and *Ma*VnfH (also see section 4.1.1.1 above), which established a correlation between the inhibition of N_2 reduction and the lo-CO state of VnfDGK. Activity analyses revealed a drastic decrease of NH_3 formation (by ~80%) concomitant with a sharp increase of the EPR feature of the lo-CO state (to >50% of the maximum intensity) upon an increase of the CO concentration to 0.1 atm, as well as a further decrease in the activity of N_2 reduction that was accompanied by a continued increase in the intensity of the lo-CO signal with increasing concentrations of CO.[176] Such a correlation was not observed between the N_2-reducing activity and the hi-CO state, as the intensity of the hi-CO signal only started to increase beyond 0.5 atm CO, where the production of NH_3 was already completely abolished. [176] These observations once again highlight the catalytic relevance of the lo-CO state, but more importantly, they point to a competition between N_2 and lo-CO species for the reactive diiron site of the cofactor—most likely that located at the S2B site—which is consistent with the structural observation of a shared binding site and, by extrapolation, a shared mechanism, between nitrogenase-catalyzed CO and N_2 reduction.

4.1.2. Pathway and intermediates of the enzymatic CO reduction

The pathway of the enzymatic CO reduction by nitrogenase was explored by DFT calculations, which led to the proposal of sequential reduction and protonation of a bound CO moiety in a series of events analogous to those proposed for the reduction of N_2.[188,189] The most energetically demanding step in the DFT models is the first reduction step, which involves formation of a metal-formyl species (M–CHO) via reduction of an activated, metal-bound CO ligand (M–CO). The formation of C–C bonds in C_2 and C_3 hydrocarbons, on the other hand, presumably routes via a methylene intermediate. Additionally, formation of longer hydrocarbon chains likely involves more steps than that proposed for N_2 reduction, consistent with a difference in the nature of the reactions of CO and N_2 reduction by nitrogenase. These theoretical studies provided an important foundation for further exploring the mechanistic details of the enzymatic CO reduction by nitrogenase.

The experimental platform for the mechanistic investigation of CO reduction by nitrogenase was supplied by the observation of a novel FT-type reactivity of the isolated M-cluster with aldehydes (see section 3.2.1 above).[164] Isotope labeling experiments were conducted with deuterated aldehydes to identify intermediates that appeared along the reaction pathway of C_1 substrate reduction. [164] Driven by Eu(II)-DTPA, the isolated M-cluster generated the same product, CH_2D_2, upon reduction of formaldehyde (CH_2O) in a D_2O-based reaction, or upon reduction of D_2-labeled formaldehyde (CD_2O) in an H_2O-based reaction. The observation that both substrate-derived hydrogen atoms (*i.e.*, 2 H in CH_2O, or 2 D in CD_2O) were retained in the product suggested that activation of the C_1 aldehyde resulted in a metal-bound hydroxymethyl intermediate, which could undergo further reduction to yield CH_4 (**Figures 28A and B**).[164] By analogy, activation of acetaldehyde would lead to the formation of a metal-bound hydroxyethyl intermediate, which could be further reduced to yield C_2 hydrocarbons. Interestingly, in the presence of Eu(II)-DTPA, the isolated M-cluster generated CD_2=CDH and CD_2=CH_2, respectively, as the predominant products from the reduction of D_3- and D_4-labeled acetaldehyde, CD_3CHO and CD_3CDO, in H_2O-based reactions. The observation that only one β-hydrogen was replaced in both cases would be consistent with a mechanism involving the release of the alkene product, C_2H_4, via β-hydride elimination (**Figures 28C and D**).[164]

The appearance of hydroxymethyl and hydroxyethyl intermediates in these reactions *en route* to hydrocarbon formation points to a relevance of these species to the cofactor-based CO reduction.

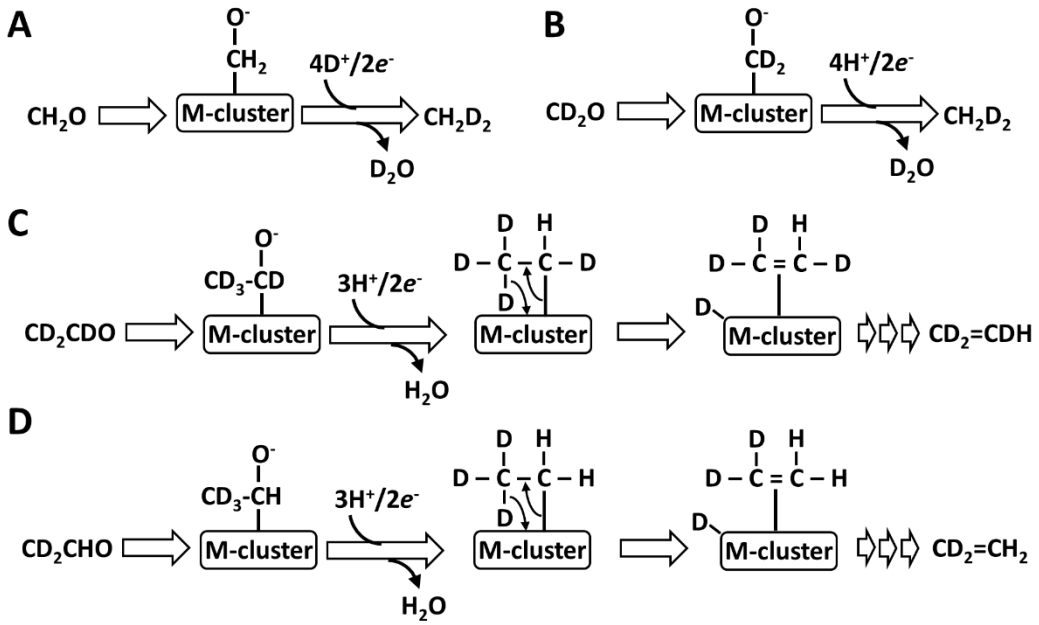

Figure 28. Activation of C_1 and C_2 aldehydes by the extracted M-cluster. Generation of methane from (A) the reduction of CH_2O in an H_2O-based reaction or (B) the reduction of CD_2O in a D_2O-based reaction; and generation of ethylene from the reduction of (C) CD_3CDO or (D) CD_3CHO in H_2O-based reactions.

In support of this suggestion, both C_1 and C_2 aldehydes could be coupled with CO to yield hydrocarbons. The cross coupling between aldehydes and other C_1 substrates was verified by isotope labeling experiments, and the preference of cross-species coupling over same-species coupling—as reflected by product distribution—provided further support for aldehyde-derived species being the relevant intermediates of CO reduction. In this context, one plausible route to the aldehyde-derived C_2 intermediate (containing one O atom) could involve C–C coupling between a fully reduced, oxygen-free C moiety (such as an M–CH_3 species derived from the 'first' CO) and a partially reduced, oxygen-containing C moiety (such as an activated M–C≡O moiety derived from the 'second' CO) via migratory insertion of CO into the metal-alkyl bond. Interestingly, DFT calculations led to the proposal of C-C coupling between an M–CH_3 species and an M–C≡O species as part of the C_2 branch of the pathway of CO_2 reduction by the [Fe_4S_4] cluster (see section 4.2.2 below). Given the similarity between the FT-type reactivities of the complex nitrogenase cofactor and the 'simpler' [Fe_4S_4] cluster, it is plausible that these clusters share common intermediates in C_1 substrate reduction. More importantly, while a migratory insertion mechanism involving metal-bound CO and alkyl groups is favored based on the

experimental observation of an oxygen-containing C_2 intermediate, other candidates, such as metal-bound alcohol (M–ROH) and allyl (M–RCH_2) species, cannot be excluded as intermediates involved in C-C coupling. Further experiments are required to elucidate the reaction pathway of the cofactor-based C_1 substrate reduction.

4.2. Mechanism of enzymatic CO_2 reduction

4.2.1. Binding and activation of CO_2 at the [Fe_4S_4] cluster of Fe protein

Insights into the binding and activation of CO_2 at the [Fe_4S_4] cluster of Fe protein were gleaned through combined crystallographic and DFT studies of *Av*NifH and *Ma*NifH, which led to the proposal of a sequential appearance of CO_2-free, CO_2-captured and CO_2-activated conformations upon binding and activation of CO_2 by the Fe protein (**Figure 29**).[190,191]

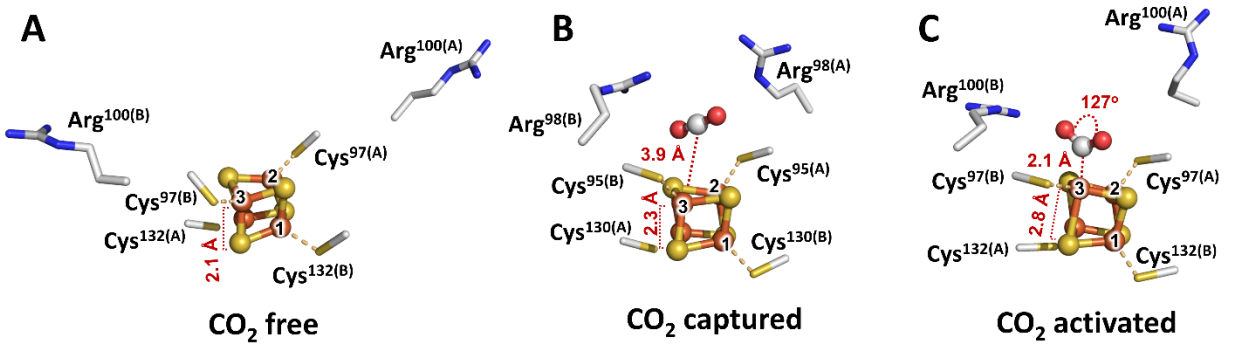

Figure 29. Activation of CO_2 by the Fe protein. Three possible conformations represented by (A) *Av*NifH^1 (PDB entry 2NIP), (B) *Ma*NifH^{1C} (PDB entry 6NZJ) and (C) *Av*NifH^{0C} (DFT-optimized structure of PDB entry 6O0B) that depict the CO_2-free, CO_2-captured and CO_2-activated states of the Fe protein during the process of CO_2 activation. The [Fe_4S_4] cluster of the Fe protein is presented and colored as that in Figure 1.

Crystallization of dithionite-reduced *Ma*NifH in the presence of bicarbonate resulted in a CO_2-bound, but unactivated conformation (**Figure 29B**).[191] The 2.4 Å crystal structure of the dithionite- and bicarbonate-treated *Ma*NifH (designated *Ma*NifH^{1C}) adopts the typical conformation observed in all reported Fe protein structures, including that of the dithionite-reduced *Av*NifH (designated *Av*NifH^1) (**Figure 29A**);[44] however, there is some 'extra' electron density at the [Fe_4S_4] cluster of *Ma*NifH^{1C} that could be modeled as a linear, unactivated CO_2 ligand 'held' by a conserved Arg residues ($Arg^{98(A)}$, $Arg^{98(B)}$). However, the identity of this ligand could not be conclusively

assigned given its location near the crystallographic symmetry axis. To circumvent this problem, binding of CO_2 to the dithionite-reduced *Ma*NifH protein was evaluated by DFT calculations, which demonstrated the capture of a linear, unactivated CO_2 moiety near the $[Fe_4S_4]^{1+}$ cluster by the conserved Arg pair in a cage-like configuration, despite the tendency of CO_2 to dissociate from the $[Fe_4S_4]^{1+}$ cluster. Such a low binding affinity of CO_2 is consistent with the low activity of NifH to reduce CO_2 in the presence of dithionite.[22] Strikingly, the CO_2 moiety in the DFT-optimized structure occupies a position that overlaps with the extra electron density in the crystal structure of *Ma*NifH^{1C}. In both crystallographically-determined and DFT-optimized structures of *Ma*NifH^{1C}, the C atom of CO_2 is ~4 Å from the Fe3 atom of the $[Fe_4S_4]$ cluster, with the guanidinium groups of the Arg$^{98(B)}$ and Arg$^{98(A)}$ taking the proximal and distal positions, respectively, to C and Fe3. Such a conformation signifies a role of C and Fe3 in the subsequent events leading to the activation of CO_2 (see below).[191]

While the crystal structure of a CO_2-activated conformation of Fe protein has yet to be obtained, a 1.6 Å crystal structure of the substrate-free, all-ferrous *Av*NifH (designated *Av*NifH^0) provided the initial insights into the activation of CO_2 by the all-ferrous Fe protein[190] Generated in the presence of excess Eu(II) compound, the *Av*NifH crystals had a pink hue that was characteristic of the all-ferrous $[Fe_4S_4]^0$ cluster, a competent state for CO_2 reduction.[21,22] While there is an overall conservation in structure between the all-ferrous *Av*NifH^0 and its dithionite-reduced *Av*NifH^1 counterpart, the helices C^A and C^B become substantially more linearly aligned in *Av*NifH^0 as compared to those in *Av*NifH^1.[190] Such a change causes a significant, yet asymmetric 'swing' of a conserved Arg pair (Arg$^{100(A)}$ and Arg$^{100(B)}$, which correspond to Arg$^{98(A)}$ and Arg$^{98(B)}$ in *Ma*NifH) that is terminally located in helices C^A and C^B, with Arg$^{100(B)}$ moving a lot closer to Fe3 of the cluster and Arg$^{100(A)}$ remaining similarly distanced from Fe2 of the cluster. Subsequent DFT modeling of CO_2 into the crystal structure of *Av*NifH^0 led to the proposal of a CO_2-activated conformation (designated *Av*NifH^{0C}), with the CO_2 moiety adopting a 'bent', carboxylate-like form with an O–C–O angle of 127° in this structure (**Figure 29C**).[190] Strikingly, in the CO_2-activated *Av*NifH^{0C}, Fe3 of the $[Fe_4S_4]^0$ cluster is 'lifted' out of plane to allow binding of the C atom of CO_2 at an Fe–C distance of 2.1 Å; whereas the 'proximal' Arg$^{100(B)}$ forms a hydrogen bond with one O atom of CO_2. The observation derived from the DFT-optimized structure of *Av*NifH^{0C} is consistent with that derived from the crystal structure of *Av*NifH^0, both of which point to Fe3

and $R100^{B}$ as the key elements to enable an asymmetric binding and activation of CO_2 by the seemingly symmetric structural elements of the Fe protein and its associated $[Fe_4S_4]$ cluster.

Three snapshots represented by *Av*NifH[1], *Ma*NifH[1C] and *Av*NifH[0C] could be pieced together into a plausible sequence of events that occur upon binding and activation of CO_2 by the all-ferrous Fe protein. This process begins with a substrate-free conformation (*Av*NifH[1]), followed by capture of an unactivated CO_2 molecule by the Arg pair that renders the C atom of CO_2 at a distance of ~4 Å to Fe3 of the $[Fe_4S_4]$ cluster (*Ma*NifH[1C]), and the subsequent activation of CO_2 via binding of its C atom to Fe3 of the $[Fe_4S_4]$ cluster at a distance of 2.1 Å and hydrogen-bonding of one O atom of CO_2 by the proximal Arg residue (*Av*NifH[0C]) (**Figure 29**). Importantly, the movement of the conserved Arg pair toward the all-ferrous $[Fe_4S_4]$ cluster of the Fe protein is analogous to the movement of a flexible Arg pair upon reduction of the ADP-bound activator (HgdC) of 2-hydroxyglutaryl-CoA dehydratase.[192,193] This observation is particularly relevant given that HgdC (an ASKHA class ATPase) is the only enzyme other than the Fe protein that contains a $[Fe_4S_4]$ cluster that is capable of adopting the all-ferrous state.[194] The proposal of an asymmetric functionality of the Arg pair of the Fe protein, on the other hand, is supported indirectly by an earlier report that regulation of nitrogenase activity was accomplished via an asymmetric ADP ribosylation of one of the same conserved Arg pair.[195] Likewise, the potential involvement of a unique Fe site of the all-ferrous Fe protein is consistent with the previous Mössbauer observation of a distinctive Fe site in the all-ferrous $[Fe_4S_4]$ cluster of this protein.[70] Introduction of such an asymmetry to the seemingly equivalent elements in the Fe protein could be key to the CO_2 reactivity of the Fe protein, with its proximal/distal Arg pair and the unique Fe3 site of its $[Fe_4S_4]^0$ cluster being the respective mimics of the 'asymmetric' His/Lys pair (which coordinates the O atoms of CO_2) and the 'asymmetric' Fe/Ni pair of the C-cluster (which functions as Lewis acid/base) in CODH, both of which are crucial for the initial activation of CO_2 and the subsequent scission of one of its C–O bonds.[8-12]

4.2.2. Pathway of CO_2 reduction at the $[Fe_4S_4]$ cluster

The pathway of CO_2 reduction by the 'simpler' FeS clusters was explored by DFT calculations for both protein-bound (**Figure 30**)[190] and synthetic $[Fe_4S_4]$ clusters (**Figures 31 and 32**).[21] DFT calculations of the reaction catalyzed by the biogenic $[Fe_4S_4]$ cluster was performed on the all-ferrous *Av*NifH protein, wherein an activated CO_2 moiety is asymmetrically 'held' between a

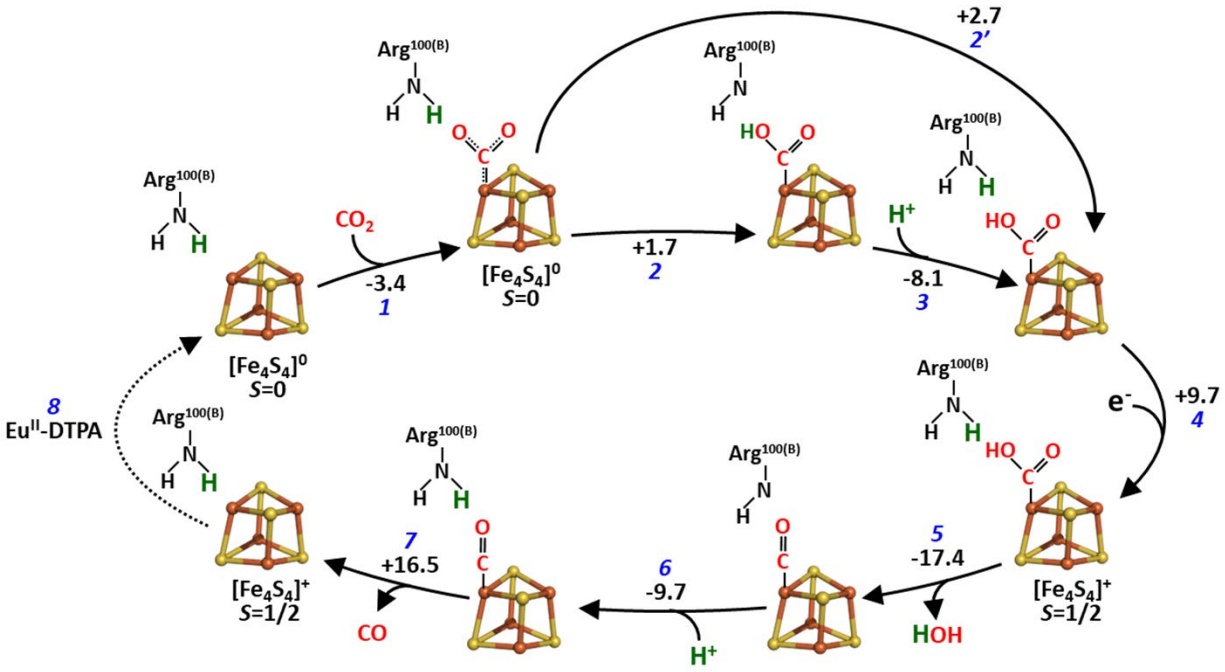

Figure 30. Proposed pathway of CO_2 reduction by the Fe protein. The energetically plausible pathway was derived from DFT calculations of CO_2 activation by *Av*NifH^0.

conserved Arg^{100} pair and coordinated via its C atom to an Fe atom of the $[Fe_4S_4]^0$ cluster concomitant with a charge redistribution to its O atoms (**Figure 29C**).[190] Transfer of a proton from the guanidinium group of the proximal Arg^{100}, which is slightly endothermic, followed by exothermic re-protonation of the proximal Arg^{100}, yields an Fe-hydroxycarbonyl (COOH) species. Subsequent electron transfer from the proximal Arg^{100} to hydroxycarbonyl moiety is endothermic, but assisted by excess reductant, leading to exothermic C-O(H) bond scission and removal of the oxygen atom as water (**Figure 30**). This event is followed by exothermic proton transfer to the proximal Arg$^{100(B)}$, endothermic dissociation of CO, and regeneration of the all-ferrous $[Fe_4S_4]^0$ cluster in excess reductant (**Figure 30**). Overall, the reaction is only moderately exothermic, which is consistent with the experimental observation of low activity of *Av*NifH in CO_2 reduction. Moreover, the proposed function of Arg as a proton donor aligns well with the observation of a substantially reduced activity of CO_2 reduction by *Ma*NifH upon mutation of Arg^{98} (corresponding to Arg^{100} in *Av*NifH) to Gly, or a largely unchanged activity upon mutation of to His, which either preserves or eliminates the hydrogen bonding capability at this position.[191]

DFT calculations of CO_2 reduction by the free, synthetic $[Fe_4S_4]$ clusters led to the proposal of two energetically plausible pathways (**Figures 31 and 32**).[21] Both pathways begin with binding of CO_2 to the all-ferrous $[Fe_4S_4]^0$ cluster ($S = 0$) in a slightly exothermic step, followed by protonation of the bound CO_2, and proton-coupled electron transfer to the protonated CO_2 moiety. These events initiate the removal of one O atom of CO_2 as water, which result in a CO-bound $[Fe_4S_4]^{1+}$ cluster. The two pathways branch at this point, with one of them (Pathway I) involving dissociation/association of a thiolate ligand and the other (Pathway II) having the thiolate ligand intact. In Pathway I (**Figure 31**), [21] the CO-bound $[Fe_4S_4]^{1+}$ cluster either undergoes energetically unfavorable CO dissociation and re-reduction of the cluster to the all-ferrous state, or is transformed into an aldehyde-like, Fe-formyl intermediate via exothermic dissociation of the thiolate ligand of the CO-coordinating Fe atom, and proton-coupled electron transfer to the bound CO moiety. Subsequently, the Fe-formyl species undergoes several exothermic steps of proton-coupled electron transfer concomitant with removal of O as water to yield a reactive Fe-methyl species. Such a species is either responsible for the release of CH_4 upon electron- and proton-transfer from a free thiol, followed by reassociation of a thiolate ligand to the $[Fe_4S_4]$ cluster; or it is poised for C-C coupling upon exothermic binding of a second CO moiety to the same, methyl-coordinating Fe atom. Migratory insertion of CO into the Fe-methyl bond results in an Fe-acetyl intermediate, which then undergoes a series of exothermic steps of proton-coupled electron transfer concomitant with removal of O as water to yield an Fe-ethyl species. Subsequent electron- and proton-transfer from a free thiol to the Fe-ethyl intermediates results in the release of C_2H_6, and this event is accompanied by re-reduction of the $[Fe_4S_4]$ cluster and re-association of the thiol group to the cluster. In Pathway II (**Figure 32**),[21] the CO-bound $[Fe_4S_4]^{1+}$ cluster undergoes analogous steps to those in Pathway I to yield CH_4. However, contrary to the migratory insertion of CO into the Fe-methyl bond in Pathway I, the second CO is attached to a different Fe atom than that coordinating the methyl group. Such a difference results in transformation of the second Fe-bound CO moiety into a reactive Fe-methylene species via proton- and electron-transfer steps, followed by coupling between the Fe-methylene species (derived from the second CO) and the Fe-methyl species (derived from the first CO) to yield an Fe-ethyl species.

Despite their distinct mechanistic features, the two pathways derived from DFT calculations on the synthetic $[Fe_4S_4]$ clusters are principally similar to each other, both involving aldehyde-like intermediates along the reaction pathway and both suggesting a shift from CO release to CO

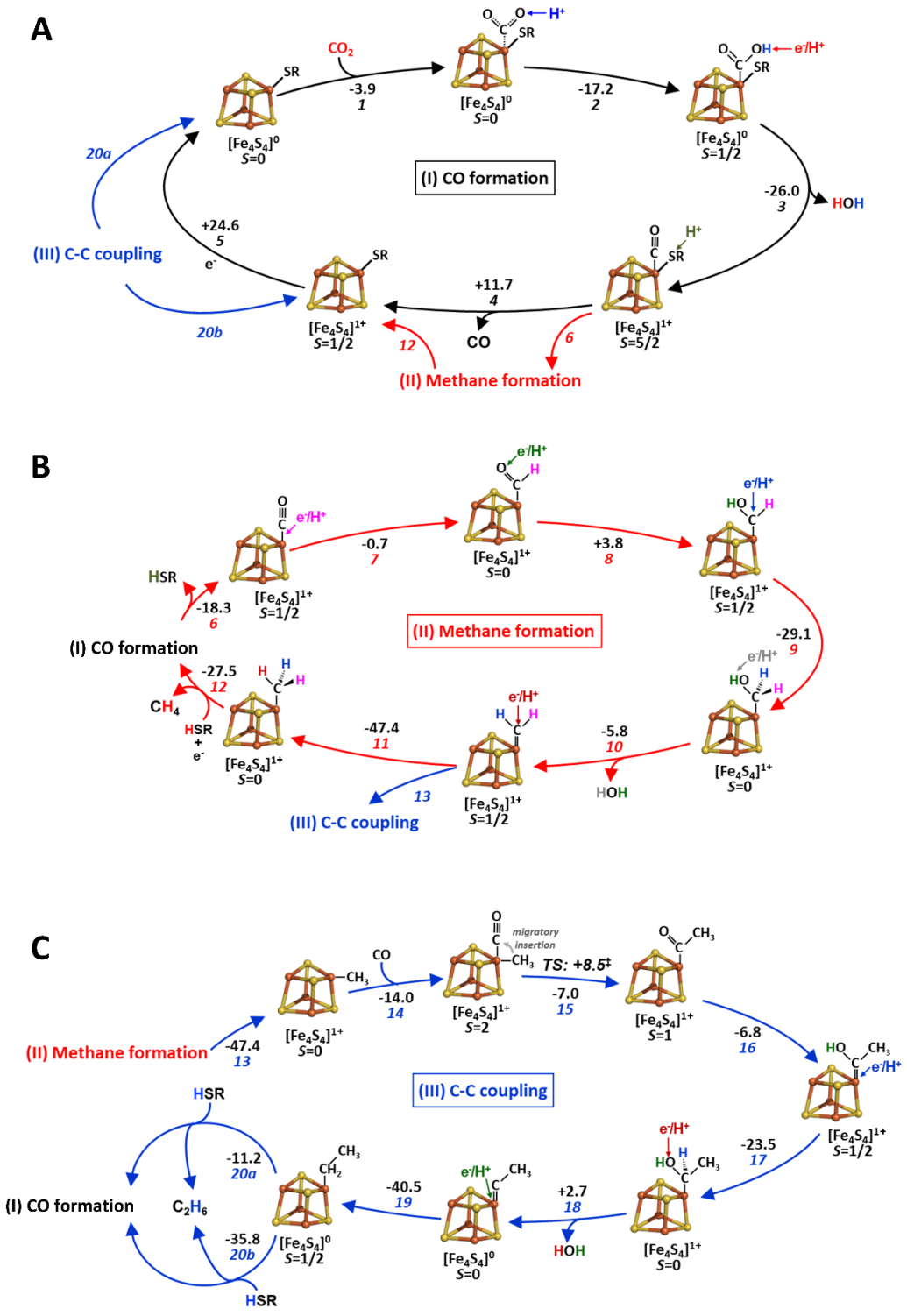

Figure 31. Proposed pathway (Pathway I) of CO_2 reduction by the [Fe4S4] cluster. Shown are the proposed events for (A) CO formation; (B) CH_4 formation; and (C) C-C bond formation. The energetically plausible pathway was derived from DFT calculations of CO_2 activation by $[Fe_4S_4]^{Syn}$ and is characterized by dissociation and re-association of a thiolate ligand of the cluster and proceeds with migratory insertion of CO into an Fe-methyl bond for C-C coupling.

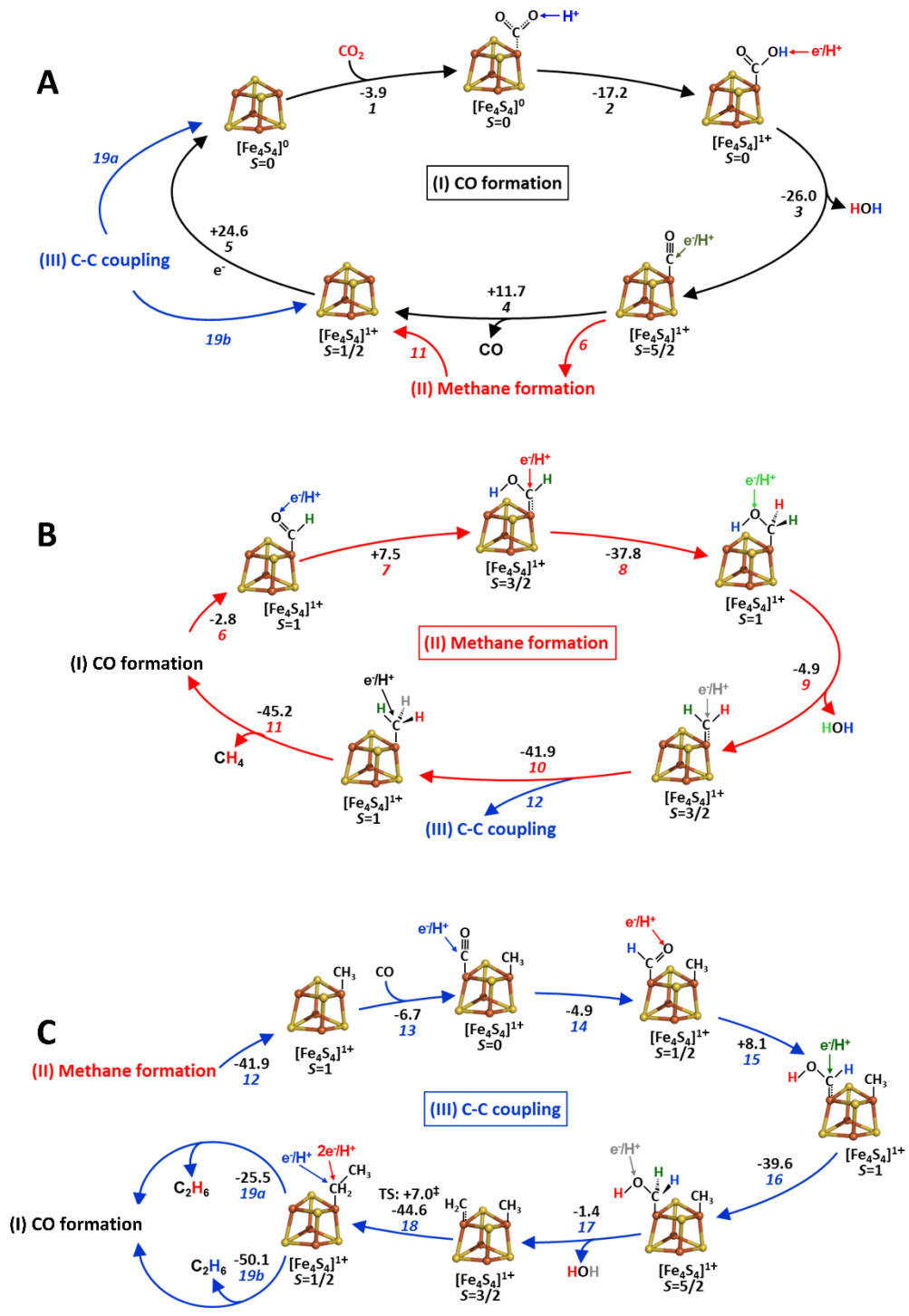

Figure 32. Alternative pathway (Pathway II) of CO_2 reduction by the [Fe4S4] cluster. Shown are the proposed events for (A) CO formation; (B) CH_4 formation; and (C) C-C bond formation. The energetically plausible pathway was derived from DFT calculations of CO_2 activation by $[Fe_4S_4]^{Syn}$, but differs from the pathway shown in Fig. 32 in that it does not involve dissociation of a thiolate ligand of the cluster and proceeds with coordination events at two neighboring Fe centers for C-C coupling.

reduction in the presence of excess electrons. Consistent with these theoretical predictions, the synthetic [Fe_4S_4] cluster was experimentally verified for its ability to reduce formaldehyde to CH_4, and the protein-bound [Fe_4S_4] cluster was shown to generate products with an increased ratio between hydrocarbons and CO in the presence of higher concentrations of reductant.[21] Interestingly, the mechanistic features of C_1 substrate reduction are not only shared between biogenic and synthetic [Fe_4S_4] clusters, but also with complex nitrogenase cofactors, pointing to a similar mechanism that is employed by the various nitrogenae-associated metalloclusters in the FT-type reactions. Moreover, certain mechanistic aspects concerning C-C coupling (*e.g.*, migratory insertion of CO) and alkene formation (*e.g.*, β-elimination) and the identities of potential intermediates (e.g., hydroxymethyl) that are either proposed or observed for the nitrogenase-derived FT reactions are also shared by the chemical FT reaction,[1,2] highlighting a broad mechanistic similarity between the enzymatic and chemical FT systems.

5. Potential applications and evolutionary relevance

5.1. Potential applications

The ability of nitrogenase-derived systems to convert CO and CO_2 at ambient temperature and pressure, coupled with the utilization of protons/electrons by these systems as the reducing equivalents, make them attractive platforms for the future development of biotechnological applications for the carbon-neutral production of hydrocarbon products.

The protein-based system is amenable to the development of both *in vitro* and *in vivo* applications for the conversion of C_1 substrates to hydrocarbons, with the required components being the reductase component and/or the catalytic component of nitrogenase and a suitable electron source, which allow the nitrogenase protein to function either in the presence or absence of ATP. The *in vitro* applications are cumbersome in that purified enzymes, which are highly sensitive to O_2, need to be prepared and handled properly. However, supplementation with excess reductant (such as dithionite) could mitigate this problem and protect nitrogenase from O_2 damage. Additionally, substitution of the sacrificial reductant with an electrode, as demonstrated for *Av*VnfDGK,[28] could present a solution to sustain the reactivity. The *in vivo* whole-cell applications, on the other hand, could benefit from the high respiration rates and the electrons supplied by ferredoxins and flavodoxins in the host organisms (such as *A. vinelandii*) that allow nitrogenase to express and

function properly in a reducing environment, well protected from O_2 damage. The V-nitrogenase from *A. vinelandii*, in particular, is an interesting candidate to be considered for a two-step, whole-cell strategy of C_1 substrate conversion. Taking advantage of the ability of *Av*VnfH to enable the *in vivo* reduction of CO_2 to CO, and the fact that the *in vivo* reduction of CO to hydrocarbons by the complete *Av* V-nitrogenase (*i.e.*, *Av*VnfH/*Av*VnfDGK) is a secondary metabolic pathway that expels hydrocarbons as waste products, a coupling of these two whole-cell reactions could produce a system for the stepwise conversion of the greenhouse CO_2 into the useful hydrocarbon products. Moreover, exploration of the C_1 reactivity in photoautotrophic organisms, as illustrated in the case of the *R. palustris* Fe-only nitrogenase,[29] could provide a sustainable solution to the high energy demand that is one major drawback of this type of applications.

Compared to the protein-based system, the cluster-based system is limited to *in vitro* applications, although it can catalyze the reductive C-C coupling of substrates like CN^- and aldehydes in reactions inaccessible to the nitrogenase enzymes. The fact that synthetic cofactor mimics and $[Fe_4S_4]$ clusters can perform the same C_1 chemistry as their native counterpart points to the possibility to use these clusters as templates for the future development of efficient FeS-based catalysts for hydrocarbon production from C_1 substrates. As is with the protein-based systems, the cluster-based systems are limited in their applicability by the O_2 sensitivity, the reaction scale and the consumable reductant. Moreover, both protein- and cluster-based applications have relatively low product yields. Nevertheless, optimizing these factors and extending this unique reactivity to an electrochemical or light-driven context may present an effective route to hydrocarbon production in the future.

5.2. Evolutionary relevance

The ability of nitrogenase proteins to reduce the green-house gas CO_2 is not only interesting from the perspective of environment and energy, but could also have relevance to the origin of life (OOL) on Earth. The early Earth's atmosphere was mainly influenced by volcanic outgassing and, consequently, it was rich in CO_2 but contained N_2 and O_2 only in trace amounts.[196] This thick CO_2 atmosphere remained over the first two billion years until the O_2-generating bacteria appeared and paved the way for the evolution of the Earth's atmosphere to its current composition.[197] As most of the available carbon was present in the form of CO_2, the processes leading to the first emergence of life on Earth were inevitably connected to those capable of performing C-C bond formation

from CO_2. It is exciting, therefore, to realize that the isolated M-, V- and L-clusters of nitrogenases, as well as their synthetic mimics, can effect the transformation of CO_2 into short-chain hydrocarbons.[24,25] Of particular primordial relevance are the observations that an all-iron synthetic mimic of the cofactor (*i.e.*, the Fe_6 cluster, see section 3.2.2 above) can reduce CO_2 to hydrocarbons independent of the interstitial C^{4-} ion[163] and that both the biogenic and synthetic $[Fe_4S_4]$ clusters can perform the same reaction without the input of ATP,[22,67,191] both of which demonstrate the FT-type reactivity of the 'simpler' FeS clusters in the presence of a sufficient supply of electrons.

While FeS clusters can be generated upon reaction of Fe^{II} and S^{-II} in aqueous media under experimental conditions, they typically agglomerate into bigger aggregates and precipitate in the form of iron sulfide minerals under natural conditions.[198] Mackinawite ($Fe^{II}S^{-II}$) is the first iron sulfide mineral formed during precipitation and probably the natural precursor to other iron sulfide minerals like greigite ($[Fe^{II}Fe^{III}_2]S^{-II}_4$) and pyrite ($Fe^{II}S^{-I}_2$), and iron oxides like magnetite ($[Fe^{II}Fe^{III}_2]O^{-II}_4$) and hematite ($Fe^{III}_2O^{-II}_3$).[199,200] It has a layered structure wherein each Fe atom is surrounded by four equidistant S atoms in a tetragonal geometry. The individual layers of mackinawite are connected by van der Waals forces and consist of Fe atoms in planar coordination, with an Fe–Fe distance of 2.5967 Å like that observed in the metallic Fe (**Figure 33**).[201] Once dried, mackinawite is known to readily react with O_2 to generate greigite, sulfur (S^0), magnetite

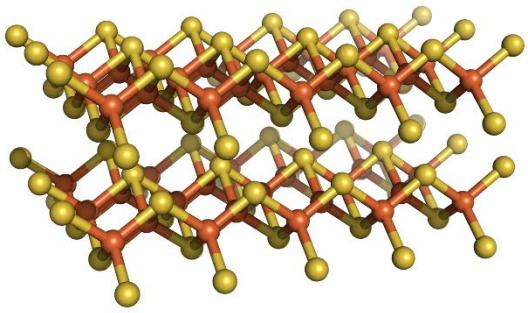

Figure 33. Structure of mackinawite. Shown is the typical layered structure of mackinawite in which each Fe atom is surrounded by four equidistant S atoms in a tetragonal geometry. Atoms are colored as those in Figure 1.

and iron(oxo)hydrates.[202]These oxidized compounds also bear prebiotic importance, with greigite compared with iron sulfur clusters for structural similarities[203,204] and magnetite implicated as a catalytic surface for the reduction of CO_2.[205-207]

Because of their omnipresence on early Earth, metal sulfide minerals have long been suggested to have played an important role during the OOL. Mackinawite is of particular interest as formation of the more stable, oxidized iron sulfide minerals like pyrite can provide electrons for the prebiotic reduction reactions. The 'pyrite-pulled' reaction was first proposed by Wächtershäuser and later supported by the experimentally observed formation of H_2 and pyrite in reactions containing mackinawite and H_2S.[208-210] Like the reaction system based on the M-cluster, the reaction system based on mackinawite and H_2S was also shown to reduce C_2H_2 into C_2H_4 and even N_2 into NH_3 under prebiotically plausible conditions.[211,212] Additionally, CO_2 and FeS were shown to react under acidic conditions and generate C_1 to C_5 thiols as the main products of the reaction,[213] analogous to the formation of C_1 to C_4 hydrocarbons upon reduction of CO_2 by nitrogenase cofactors, synthetic cofactor mimics and $[Fe_4S_4]$ clusters.

In addition to their catalytic properties in C_1 substrate reduction, iron sulfide minerals are also known for their ability to bind charged compounds, such as metal ions or functionalized organic molecules. It has been demonstrated that highly toxic metals, such as Cd^{II}, $As^{III/IV}$ and Cr^{VI}, can bind to nano-particulate mackinawite.[214-218] Such an ability is of particular interest for the treatment of wastewater. Additionally, for a highly chaotic habitat like early Earth, this ability could be highly beneficial in creating environments with lower toxicity and, consequently, conditions suitable for the first life to emerge. The ability of iron sulfide minerals to bind organic molecules, on the other hand, bears direct significance for the OOL, as concentrating the organic precursor molecules on the surface of iron sulfide minerals would be the prerequisite for the formation of essential macromolecules like proteins or lipids. The scenario of surface-bound/concentrated organic molecules was initially proposed for pyrite, which could supply a negatively charged particle surface for the attachment of organic molecules; later, such a scenario was also applied to mackinawite, which was shown to bind nucleic acids in aqueous solutions.[210,219]

The prebiotic processes related to iron sulfides have long been associated solely with hydrothermal conditions, where H_2S—emerging from cracks in the seafloor—could react with the Fe^{II} ions

dissolved in early oceans to form black clouds of mackinawite.[220-222] However, although these black smokers would have provided a hostile habitat that protected the first organisms from the Late Heavy Bombardment (LHB), they prevented other elementary processes, such as wet-dry cycles, from happening.[223] Additionally, the location of these black smokers on the seafloor would not have allowed for an efficient exchange with a wide range of substrates formed in the primordial atmosphere. In this context, HCN has been brought to the foreground as a candidate to enable prebiotic events at the surface of early Earth. As one of the most anticipated prebiotic precursors, HCN is well known for its base-catalyzed condensation into adenine and its appearance as an intermediate in the famous Miller-Urey experiment.[224,225] While the availability of HCN on early Earth is still a topic of debate, it is known to be formed photochemically upon reaction between a sufficient amount of CH_4 and N_2[226] via lightning[227] and meteor impacts.[228] Another proposed origin of HCN are comets that hit early Earth with low-angle impacts, and it has been demonstrated that the survival rate of HCN under such circumstances is high enough to provide at least locally elevated HCN concentrations.[229] In a recent study, HCN was shown to react in a UV-driven metabolic cycle powered by the redox chemistry of hexacyanoferrates to form precursors for amino acids, ribonucleotides and lipids.[230] Such conditions would have only been accessible on the surface of the early Earth and might have been realized in the form of multiple ponds feeding each other through flow chemistry.[231] Additionally, it was suggested that the presence of highly reducing surface hydrothermal vents could have built a bridge between the two major OOL scenarios involving hydrothermal vents and photochemistry.[232] Further complementing these scenarios was the earlier report of a synthetic route to mackinawite that involved reaction between iron and sulfur powders, two abundant elements on the surface of early Earth.[233] With this suggestion in mind, most of the previously discussed functionalities of metal sulfides can now be considered under conditions that allowed H_2O to be frequently absent, which opened up new avenues for studies of additional substrates that could emerge from photochemistry in the early atmosphere. Along this line of investigation, HCN was shown to be reduced by mackinawite to a number of prebiotically relevant compounds, including greigite, CH_4, C_1–C_4 thiols, NH_3 and CH_3CHO.[234] The observation of CH_3CHO formation is especially promising, as this organic C_2 compound was previously used for the synthesis of deoxyribonucleotides from purine/pyrimidine bases and sugar-forming precursors.[235]

Taken together, the terrestrial OOL most likely followed an initial chemical evolution of biologically relevant precursors from small substrates, such as minerals and reduced volcanic exhalations, and natural energy sources, such as photochemistry and lightning. While geological evidence points to the appearance of life on Earth 3.5 Ga ago, more recent findings of organic structures conserved in hydrothermal precipitates of the earliest vent systems suggest that this event could have occurred as early as 4.25 Ga ago.[236] Though these findings indicate that replicating organisms once populated the hydrothermal systems, there is no definitive answer as to how and where exactly the first life emerged. One of the key transition points from an inanimate system to a living one, however, is the evolution of stabilized metal sulfide clusters that allow for efficient electron transport and substrate reduction. It was previously reported that stabilized iron sulfur clusters, including $[Fe_4S_4]$ clusters, $[Fe_2S_2]$ clusters and mononuclear species, were generated spontaneously when Fe^{II}/Fe^{III} were reacted with S^{-II} in the presence of micromolar amounts of cysteine in an alkaline solution. An early involvement of primitive enzymes containing these simple FeS clusters during the OOL would be a beneficial step for the evolution of more complex metalloclusters like the ones still in used by the nitrogenase enzyme and could account for their FT-type reactivity with C_1 substrates as a possible evolutionary relic.

6. Concluding remarks

The discovery that nitrogenase is capable of catalyzing FT-type reactions at ambient conditions is exciting because of its implications for nitrogenase mechanism, prebiotic chemistry and biotechnological applications. Mechanistically, the observation of a shared binding mode via belt-sulfur displacement and, at least in part, the binding site(s) between CO and N_2 points to certain common mechanistic aspects shared by the reactions of CO- and N_2-reduction; whereas DFT calculations and experimental data suggest aldehyde-derived species as the intermediates of CO reduction and a plausible migratory insertion mechanism for C-C coupling. From the perspective of evolution, the FT-type reactivities of the nitrogenase-associated metalloclusters, synthetic cofactor mimics and even simpler FeS clusters tie in with the ability of iron sulfide minerals to reduce C_1 substrates, thereby establishing a primordial relevance of nitrogenase to the origin of life on Earth. In a practical vein, the ability of various nitrogenase-derived systems to effect ambient reduction of C_1 substrates to hydrocarbons suggests the utility of these systems in the future development of biotechnological applications for the carbon-neutral production of

hydrocarbon products. Further research is needed to explore the many facets of the C_1 reduction chemistry of nitrogenase to advance our knowledge and harness the full potential of the enzymatic FT-type reactions.

Author Information

Corresponding Author

Yilin Hu

https://orcid.org/0000-0002-9088-2865; E-mail: yilinh@uci.edu

Markus W. Ribbe

https://orcid.org/0000-0002-7366-1526; E-mail: mribbe@uci.edu

Complete contact information is available at: https://pubs.acs.org/10.1021/acs.chemrev.xxxxxxx

Notes

The author declare no conflict of interest.

Biographies

Yilin Hu received her B.S. degree in Genetic Engineering from FuDan University, P. R. China and her Ph.D. in Biochemistry from Loma Linda University, USA. She was a postdoctoral fellow at the University of California, Irvine, and is currently Professor at the same institute. She focuses on studies related to nitrogenase mechanism and assembly, with an emphasis on the genetic manipulation of nitrogenase systems.

ORCID 0000-0002-9088-2865

Chi Chung Lee received his B.S. degree in Molecular Biology from the University of California, San Diego, and his Ph.D. degree in Molecular Biology and Biochemistry from the University of California, Irvine (UCI). He was a postdoctoral fellow at UCI for several years and is currently a Project Scientist at the same institute. During the last 15 years, his research interests have centered on the assembly of the nitrogenase cofactors as well as the mechanisms of substrate reduction.

Mario Grosch received his B.S. and M.S. degrees in Chemistry from the Friedrich-Schiller-University Jena, Germany. He remained at the same institute to study the reduction of C_1 substrates by mackinawite under primordial conditions under the supervision of Prof. Dr. Wolfgang Weigand, receiving his Ph.D. degree in 2022. He is currently working at the University of California, Irvine in the groups of Professors Yilin Hu and Markus Ribbe on the biochemistry and spectroscopy of nitrogenase.

Joseph B. Solomon received his B.S. degrees in Biological Chemistry and Chemistry, and his M.S. degree in Inorganic Chemistry from the University of Chicago. He then moved to the University of California, Irvine, and is currently a Ph.D. student in the Chemistry program of UCI, working on the heterologous expression of nitrogenase in the groups of Professors Markus Ribbe and Yilin Hu.

Wolfgang Weigand received his B.S. degree in Chemistry and his Ph.D. degree in Inorganic Chemistry from the Ludwig-Maximilians-University Munich, Germany. He was a postdoctoral fellow at the ETH Zurich, Switzerland, working with Prof. Dr. Dieter Seebach on Ti(IV)-mediated peptide synthesis. He is now Professor of inorganic chemistry at the Friedrich-Schiller-University Jena, Germany. His current research interests include bioorganometallic chemistry that specifically aims at electrocatalytic and photocatalytic hydrogen evolution reaction and the synthesis of platinum anticancer prodrugs, as well as the open questions of prebiotic chemistry.

Markus W. Ribbe received his B.S in Biology and M.S. and Ph.D. degrees in Microbiology from University of Bayreuth, Germany. He was a postdoctoral fellow at the University of California, Irvine, and is now Chancellor's Professor at the same institute. He focuses on the mechanistic investigation of nitrogenase catalysis and assembly by combined biochemical, spectroscopic, and structural approaches.

ORCID 0000-0002-7366-1526

Acknowledgements

Yilin Hu and Markus W. Ribbe were supported by NIH-NIGMS grants GM67626 (to MWR and YH) and GM141046 (to YH and MWR), which funded research related to nitrogenase assembly and catalysis, respectively. The authors were also supported by the Department of Energy grants DOE (BES) DE-SC0016510 (to YH and MWR) and DE-SC0014470 (to MWR and YH), which funded work related to the mechanistic investigation of ammonia formation by nitrogenase engineering and hydrocarbon formation by nitrogenase hybrid systems, respectively. In addition, the authors were supported by NSF grants CHE-1904131 (to MWR and YH) and CHE-1651398 (to YH) that supported work related to CO activation by nitrogenase and CO_2 reduction by nitrogenase Fe proteins, respectively.

References

(1) Bukur, D.B.; Todic, B.; Elbashir, N. Role of water-gas-shift reaction in Fischer–Tropsch synthesis on iron catalysts: A review. *Catal. Today* **2016**, *275*, 66 –75.

(2) Rofer-DePoorter, C.K. A comprehensive mechanism for the Fischer-Tropsch synthesis. *Chem. Rev.* **1981**, *81*, 447– 474.

(3) Sickerman, N.S.; Hu, Y.; Ribbe, M.W. Activation of CO_2 by vanadium nitrogenase. *Chem. Asian J.* **2017**, *12*, 1985–1996.

(4) Xu, L.; Bao, S.; Houpt, D.J.; Lambert, S.H.; Davis, B.H. Role of CO_2 in the initiation of chain growth and alcohol formation during the Fischer-Tropsch synthesis. *Catal. Today* **1997**, *36*, 347–355.

(5) Yao, Y.; Hildebrandt, D.; Glasser, D.; Liu, X. Fischer−Tropsch synthesis using $H_2/CO/CO_2$ syngas mixtures over a cobalt catalyst. *Ind. Eng. Chem. Res.* **2010**, *49*, 11061–11066.

(6) Sultana, S.; Chandra Sahoo, P.; Martha, S.; Parida, K. A review of harvesting clean fuels from enzymatic CO_2 reduction. *RSC Adv.* **2016**, *6*, 44170–44194.

(7) Spreitzer, R.J.; Salvucci, M.E. Rubisco: structure, regulatory interactions, and possibilities for a better enzyme. *Annu. Rev. Plant Biol.* **2002**, *53*, 449–475.

(8) Ensign, S.A. Reactivity of carbon monoxide dehydrogenase from *Rhodospirillum rubrum* with carbon dioxide, carbonyl sulfide, and carbon disulfide. *Biochemistry* **1995**, *34*, 5372–5381.

(9) Kung, Y.; Drennan, C.L. A role for nickel–iron cofactors in biological carbon monoxide and carbon dioxide utilization. *Curr. Opin. Chem. Biol.* **2011**, *15*, 276–283.

(10) Fesseler, J.; Jeoung, J.-H.; Dobbek, H. How the $[NiFe_4S_4]$ cluster of CO dehydrogenase activates CO_2 and NCO^-. *Angew. Chem. Int. Ed.* **2015**, *54*, 8560–8564.

(11) Jeoung, J.H.; Fesseler, J.; Goetzl, S.; Dobbek, H. Carbon monoxide. Toxic gas and fuel for anaerobes and aerobes: carbon monoxide dehydrogenases. *Met. Ions Life Sci.* **2014**, *14*, 37–69.

(12) Stripp, S.T.; Duffus, B.R.; Fourmond, V.; Léger, C.; Leimkühler, S.; Hirota, S.; Hu, Y.; Jasniewski, A.; Ogata, H.; Ribbe, M.W. Second and outer coordination sphere effects in nitrogenase, hydrogenase, formate dehydrogenase, and CO dehydrogenase. *Chem. Rev.* **2022**, *122*, 11900–11973.

(13) Can, M.; Armstrong, F.A.; Ragsdale, S.W. Structure, function, and mechanism of the nickel metalloenzymes, CO dehydrogenase, and acetyl-CoA synthase. *Chem. Rev.* **2014**, *114*, 4149–4174.

(14) Maia, L.B.; Moura, I.; Moura, J.J.G. Molybdenum and tungsten-containing formate dehydrogenases: Aiming to inspire a catalyst for carbon dioxide utilization. *Inorg. Chim. Acta* **2017**, *455*, 350–363.

(15) Lee, C.C.; Hu, Y.; Ribbe, M.W. Vanadium nitrogenase reduces CO. *Science* **2010**, *329*, 642.

(16) Lee, C.C.; Hu, Y.; Ribbe, M.W. Tracing the hydrogen source of hydrocarbons formed by vanadium nitrogenase. *Angew. Chem. Int. Ed. Engl.* **2011**, *50*, 5545–5547.

(17) Hu, Y.; Lee, C.C.; Ribbe, M.W. Extending the carbon chain: hydrocarbon formation catalyzed by vanadium/molybdenum nitrogenases. *Science* **2011**, *333*, 753–755.

(18) Rebelein, J.G.; Lee, C.C.; Hu, Y.; Ribbe, M.W. The *in vivo* hydrocarbon formation by vanadium nitrogenase follows a secondary metabolic pathway. *Nat. Commun.* **2016**, *7*, 13641.

(19) Natzke, J.; Bruno-Bárcena, J.M. Two-stage continuous conversion of carbon monoxide to ethylene by whole cells of *Azotobacter vinelandii*. *Appl. Environ. Microbiol.* **2020**, *86*, e00446-20.

(20) Lee, C.C.; Stiebritz, M.T.; Hu, Y. Reactivity of [Fe_4S_4] clusters toward C_1 substrates: mechanism, implications, and potential applications. *Acc. Chem. Res.* ***2019****, 52*, 1168–1176.

(21) Stiebritz, M.T.; Hiller, C.J.; Sickerman, N.S.; Lee, C.C.; Tanifuji, K.; Ohki, Y.; Hu, Y. Ambient conversion of CO_2 to hydrocarbons by biogenic and synthetic [Fe_4S_4] clusters. *Nat. Catal.* **2018**, *1*, 444–451.

(22) Rebelein, J.G.; Stiebritz, M.T.; Lee, C.C.; Hu, Y. Activation and reduction of carbon dioxide by nitrogenase iron proteins. *Nat. Chem. Biol.* **2017**, *13*, 147–149.

(23) Rebelein, J.G.; Hu, Y.; Ribbe, M.W. Widening the product profile of carbon dioxide reduction by vanadium nitrogenase. *Chembiochem* **2015**, *16*, 1993–1996.

(24) Lee, C.C.; Hu, Y.; Ribbe, M.W. ATP-independent substrate reduction by nitrogenase P-cluster variant. *Proc. Natl. Acad. Sci. U.S.A.* **2012**, *109*, 6922–6926.

(25) Lee, C.C.; Hu, Y.; Ribbe, M.W. Insights into hydrocarbon formation by nitrogenase cofactor homologs. *mBio* **2015**, *6*, e00307-15.

(26) Lee, C.C.; Hu, Y.; Ribbe, M.W. Catalytic reduction of CN^-, CO, and CO_2 by nitrogenase cofactors in lanthanide-driven reactions. *Angew. Chem. Int. Ed. Engl.* **2015**, *54*, 1219–1222.

(27) Lee, C.C.; Hu, Y.; Ribbe, M.W. ATP-independent formation of hydrocarbons catalyzed by isolated nitrogenase cofactors. *Angew. Chem. Int. Ed. Engl.* **2012**, *51*, 1947–1949.

(28) Cai, R.; Milton, R.D.; Abdellaoui, S.; Park, T.; Patel, J.; Alkotaini, B.; Minteer, S.D. Electroenzymatic C-C bond formation from CO_2. *J. Am. Chem. Soc.* **2018**, *140*, 5041–5044.

(29) Zheng, Y.; Harris, D.F.; Yu, Z.; Fu, Y.; Poudel, S.; Ledbetter, R.N.; Fixen, K.R.; Yang, Z.Y.; Boyd, E.S.; Lidstrom, M.E. *et al.* A pathway for biological methane production using bacterial iron-only nitrogenase. *Nat. Microbiol.* **2018**, *3*, 281–286.

(30) Gerlach, D.L.; Lehnert, N. Fischer-Tropsch chemistry at room temperature? *Angew. Chem. Int. Ed. Engl.* **2011**, *50*, 7984–7986.

(31) Burgess, B.K.; Lowe, D.J. Mechanism of molybdenum nitrogenase. *Chem. Rev.* **1996**, *9*, 2983–3012.

(32) Buscagan, T.M.; Rees, D.C. Rethinking the nitrogenase mechanism: activating the active site. *Joule* **2019**, *3*, 2662–2678.

(33) Jasniewski, A.J.; Lee, C.C.; Ribbe, M.W.; Hu; Y. Reactivity, mechanism, and assembly of the alternative nitrogenases. *Chem. Rev*. **2020**, *120*, 5107–5157.

(34) Rutledge, H.L.; Tezcan, F.A. Electron transfer in nitrogenase. *Chem. Rev.* **2020**, *120*, 5158–5193.

(35) Smith, C.; Hill, A.K.; Torrente-Murciano, L. Current and future role of Haber–Bosch ammonia in a carbon-free energy landscape. *Energy Environ. Sci.* **2020**, *13*, 331–344.

(36) Erisman, J.W.; Sutton, M.A.; Galloway, J.; Klimont, Z.; Winiwarter, W. How a century of ammonia synthesis changed the world. *Nat. Geosci.* **2008**, *1*, 636–639.

(37) Hu, Y.; Ribbe, M.W. Special issue on nitrogenases and homologous systems. *Chembiochem* **2020**, *21*, 1668–1670.

(38) Hu, Y.; Ribbe, M.W. Nitrogenase and homologs. *J. Biol. Inorg. Chem.* **2015**, *20*, 435–445.

(39) Eady, R.R. Structure-function relationships of alternative nitrogenases. *Chem. Rev.* **1996**, *96*, 3013–3030.

(40) Harwood, C.S. Iron-only and vanadium nitrogenases: fail-safe enzymes or something more? *Annu. Rev. Microbiol.* **2020**, *74*, 247–266.

(41) Hu, Y.; Ribbe, M.W. Nitrogenases-A tale of carbon atom(s). *Angew. Chem. Int. Ed. Engl.* **2016**, *55*, 8216–8226.

(42) Hu, Y.; Lee, C.C.; Ribbe, M.W. Vanadium nitrogenase: a two-hit wonder? *Dalton Trans.* **2012**, *41*, 1118–1127.

(43) Hales, B.J. Alternative nitrogenase. *Adv. Inorg. Biochem.* **1990**, *8*, 165–198.

(44) Georgiadis, M.M.; Komiya, H.; Chakrabarti, P.; Woo, D; Kornuc, J.J.; Rees, D.C. Crystallographic structure of the nitrogenase iron protein from *Azotobacter vinelandii. Science* **1992**, *257*, 1653–1659.

(45) Wenke, B.B.; Spatzal, T.; Rees, D.C. Site-specific oxidation state assignments of the iron atoms in the $[4Fe:4S]^{2+/1+/0}$ states of the nitrogenase Fe-protein. *Angew. Chem. Int. Ed. Engl.* **2019**, *58*, 3894–3897.

(46) Walker, J.E.; Saraste, M.; Runswick, M.J.; Gay, N.J. Distantly related sequences in the alpha- and beta-Subunits of ATP synthase, myosin, kinases and other ATP-requiring enzymes and a common nucleotide binding fold. *EMBO J.* **1982**, *1*, 945−951.

(47) Walker, G.A.; Mortenson, L.E. Effect of magnesium adenosine 5′-triphosphate on the accessibility of the iron of Clostridial azoferredoxin, a component of nitrogenase. *Biochemistry* **1974**, *13*, 2382−2388.

(48) Ljones, T.; Burris, R.H. Nitrogenase: The reaction between iron protein and bathophenanthrolinedisulfonate as a probe for interactions with MgATP. *Biochemistry* **1978**, *17*, 1866−1872.

(49) Deits, T.L.; Howard, J.B. Kinetics of MgATP-dependent iron chelation from the Fe-protein of the *Azotobacter vinelandii* nitrogenase complex. Evidence for two states. *J. Biol. Chem.* **1989**, *264*, 6619−6628.

(50) Chen, L.; Gavini, N.; Tsuruta, H.; Eliezer, D.; Burgess, B.K.; Doniach, S.; Hodgson, K.O. MgATP-induced conformational changes in the iron protein from *Azotobacter vinelandii*, as studied by small-angle X-ray scattering. *J. Biol. Chem.* **1994**, *269*, 3290−3294.

(51) Jang, S.B.; Seefeldt, L.C.; Peters, J.W. Insights into nucleotide signal transduction in nitrogenase: structure of an iron protein with MgADP bound. *Biochemistry* **2000**, *39*, 14745−14752.

(52) Sen, S.; Krishnakumar, A.; McClead, J.; Johnson, M.K.; Seefeldt, L.C.; Szilagyi, R.K.; Peters, J.W. Insights into the role of nucleotide dependent conformational change in nitrogenase catalysis: structural characterization of the nitrogenase Fe protein Leu127 deletion variant with bound MgATP. *J. Inorg. Biochem.* **2006**, *100*, 1041−1052.

(53) Lindahl, P.A.; Day, E.P.; Kent, T.A.; Orme-Johnson, W.H.; Münck, E. Mössbauer, EPR, and magnetization studies of the *Azotobacter vinelandii* Fe protein. Evidence for a [4Fe-4S]$^{1+}$ cluster with spin $S = 3/2$. *J. Biol. Chem.* **1985**, *260*, 11160–11173.

(54) Angove, H.C.; Yoo, S.J.; Münck, E.; Burgess, B.K. An all-ferrous state of the Fe protein of nitrogenase. Interaction with nucleotides and electron transfer to the MoFe protein. *J. Biol. Chem.* **1998**, *273*, 26330–26337.

(55) Angove, H.C.; Yoo, S.J.; Burgess, B.K.; Münck, E. Mössbauer and EPR evidence for an all-ferrous Fe_4S_4 cluster with $S = 4$ in the Fe protein of nitrogenase. *J. Am. Chem. Soc.* **1997**, *119*, 8730–8731.

(56) Hiller, C.J.; Stiebritz, M.T.; Lee, C.C.; Liedtke, J.; Hu, Y. Tuning electron flux through nitrogenase with methanogen iron protein homologues. *Chemistry* **2017**, *23*, 16152–16156.

(57) Martin, A.E.; Burgess, B.K.; Iismaa, S.E.; Smartt, C.T.; Jacobson, M.R.; Dean, D.R. Construction and characterization of an *Azotobacter vinelandii* strain with mutations in the genes encoding flavodoxin and ferredoxin I. *J. Bacteriol.* **1989**, *171*, 3162–3167.

(58) Thorneley, R.N.; Deistung, J. Electron-transfer studies involving flavodoxin and a natural redox partner, the iron protein of nitrogenase. Conformational constraints on protein-protein interactions and the kinetics of electron transfer within the protein complex. *Biochem. J.* **1988**, *253*, 587–595.

(59) Duyvis, M.G.; Wassink, H.; Haaker, H. Nitrogenase of *Azotobacter vinelandii*: kinetic analysis of the Fe protein redox cycle. *Biochemistry* **1998**, *37*, 17345–17354.

(60) Watt, G.D.; Wang, Z.C.; Knotts, R.R. Redox reactions of and nucleotide binding to the iron protein of *Azotobacter vinelandii. Biochemistry* **1986**, *25*, 8156−8162.

(61) Lanzilotta, W.N.; Ryle, M.J.; Seefeldt, L.C. Nucleotide hydrolysis and protein conformational changes in *Azotobacter vinelandii* nitrogenase iron protein: defining the function of aspartate 129. *Biochemistry* **1995**, *34*, 10713−10723.

(62) Erickson, J.A.; Nyborg, A.C.; Johnson, J.L.; Truscott, S.M.; Gunn, A.; Nordmeyer, F.R.; Watt, G.D. Enhanced efficiency of ATP hydrolysis during nitrogenase catalysis utilizing

reductants that form the all-ferrous redox state of the Fe protein. *Biochemistry* **1999**, *38*, 14279–14285.

(63) Lowery, T.J.; Wilson, P.E.; Zhang, B.; Bunker, J.; Harrison, R.G.; Nyborg, A.C.; Thiriot, D.; Watt, G.D. Flavodoxin hydroquinone reduces *Azotobacter vinelandii* Fe protein to the all-ferrous redox state with a $S = 0$ spin state. *Proc. Natl. Acad. Sci. U.S.A.* **2006**, *103*, 17131–17136.

(64) Guo, M.; Sulc, F.; Ribbe, M.W.; Farmer, P.J.; Burgess, B.K. Direct assessment of the reduction potential of the $[4Fe\text{-}4S]^{1+/0}$ couple of the Fe protein from *Azotobacter vinelandii*. *J. Am. Chem. Soc.* **2002**, *124*, 12100–12101.

(65) Watt, G.D.; Reddy, K.R.N. Formation of an all ferrous Fe_4S_4 cluster in the iron protein component of *Azotobacter vinelandii* nitrogenase. *J. Inorg. Biochem.* **1994**, *53*, 281–294.

(66) Solomon, J.B.; Tanifuji, K.; Lee, C.C.; Jasniewski, A.J.; Hedman, B.; Hodgson, K.O.; Hu, Y.; Ribbe, M.W. Characterization of a nitrogenase iron protein substituted with a synthetic $[Fe_4Se_4]$ cluster. *Angew. Chem. Int. Ed. Engl.* **2022**, *61*, e202202271.

(67) Solomon, J.B.; Rasekh, M.F.; Hiller, C.J.; Lee, C.C.; Tanifuji, K.; Ribbe, M.W.; Hu, Y. Probing the all-ferrous states of methanogen nitrogenase iron proteins. *JACS Au* **2020**, *1*, 119–123.

(68) Chakrabarti, M.; Deng, L.; Holm, R.H.; Münck, E.; Bominaar, E.L. Mössbauer, electron paramagnetic resonance, and theoretical studies of a carbene-based all-ferrous Fe_4S_4 cluster: electronic origin and structural identification of the unique spectroscopic site. *Inorg. Chem.* **2009**, *48*, 2735−2747.

(69) Chakrabarti, M.; Münck, E.; Bominaar, E.L. Density functional theory study of an all ferrous 4Fe-4S cluster. *Inorg. Chem.* **2011**, *50*, 4322−4326.

(70) Yoo, S.J.; Angove, H.C.; Burgess, B.K.; Hendrich, M.P.; Münck, E. Mössbauer and integer-spin EPR studies and spin coupling analysis of the $[4Fe\text{-}4S]^0$ cluster of the Fe protein from *Azotobacter vinelandii* nitrogenase. *J. Am. Chem. Soc.* **1999**, *121*, 2534−2545.

(71) Howard, J.B.; Rees, D.C. Structural basis of biological nitrogen fixation. *Chem. Rev.* **1996**, *96*, 2965−2982.

(72) Rees, D.C.; Tezcan, F.A.; Haynes, C.A.; Walton, M.Y.; Andrade, S.; Einsle, O.; Howard, J.B. Structural basis of biological nitrogen fixation. *Philos. Trans. A Math. Phys. Eng. Sci.* **2005**, *363*, 971–984.

(73) Kim, J.; Rees, D.C. Crystallographic structure and functional implications of the nitrogenase molybdenum-iron protein from *Azotobacter vinelandii*. *Nature* **1992**, *360*, 553–560.

(74) Einsle, O.; Tezcan, F.A.; Andrade, S.L.; Schmid, B.; Yoshida, M.; Howard, J.B.; Rees, D.C. Nitrogenase MoFe-protein at 1.16 Å resolution: a central ligand in the FeMo-cofactor. *Science* **2002**, *297*, 1696–1700.

(75) Spatzal, T.; Aksoyoglu, M.; Zhang, L.; Andrade, S.L.; Schleicher, E.; Weber, S.; Rees, D.C.; Einsle, O. Evidence for interstitial carbon in nitrogenase FeMo cofactor. *Science* **2011**, *334*, 940.

(76) Lancaster, K.M.; Roemelt, M.; Ettenhuber, P.; Hu, Y.; Ribbe, M.W.; Neese, F.; Bergmann, U.; DeBeer, S. X-ray emission spectroscopy evidences a central carbon in the nitrogenase iron-molybdenum cofactor. *Science* **2011**, *334*, 974–977.

(77) Wiig, J.A.; Hu, Y.; Lee C.C.; Ribbe, M.W. Radical SAM-dependent carbon insertion into the nitrogenase M-cluster. *Science* **2012**, *337*, 1672–1675.

(78) Schindelin, H.; Kisker, C.; Schlessman, J.L.; Howard, J.B.; Rees, D.C. Structure of ADP x AlF_4^--stabilized nitrogenase complex and its implications for signal transduction. *Nature* **1997**, *387*, 370–376.

(79) Chan, M.K.; Kim, J.; Rees, D.C. The nitrogenase FeMo-cofactor and P-cluster pair: 2.2 Å resolution structures. *Science* **1993**, *260*, 792−794.

(80) Pierik, A.J.; Wassink, H.; Haaker, H.; Hagen, W.R. Redox properties and EPR spectroscopy of the P-clusters of *Azotobacter vinelandii* MoFe protein. *Eur. J. Biochem.* **1993**, *212*, 51−61.

(81) Huynh, B.H.; Henzl, M.T.; Christner, J.A.; Zimmermann, R.; Orme-Johnson, W.H.; Münck, E. Nitrogenase XII. Mössbauer studies of the MoFe protein from *Clostridium pasteurianum* W5. *Biochim. Biophys. Acta, Protein Struct.* **1980**, *623*, 124−138.

(82) Hagen, W.R.; Wassink, H.; Eady, R.R.; Smith, B.E.; Haaker, H. Quantitative EPR of an *S* = 7/2 system in thionine-oxidized MoFe proteins of nitrogenase. A redefinition of the P-cluster concept. *Eur. J. Biochem.* **1987**, *169*, 457–465.

(83) Hickey, D.P.; Cai, R.; Yang, Z.-Y.; Grunau, K.; Einsle, O.; Seefeldt, L.C.; Minteer, S.D. Establishing a thermodynamic landscape for the active site of Mo-dependent nitrogenase. *J. Am. Chem. Soc.* **2019**, *141*, 17150−17157.

(84) Hu, Y.; Fay, A.W.; Lee, C.C.; Ribbe, M.W. P-cluster maturation on nitrogenase MoFe protein. *Proc. Natl. Acad. Sci. U.S.A.* **2007**, *104*, 10424–10429.

(85) Lee, C.C.; Blank, M.A.; Fay, A.W.; Yoshizawa, J.M.; Hu, Y.; Hodgson, K.O.; Hedman, B.; Ribbe, M.W. Stepwise formation of P-cluster in nitrogenase MoFe protein. *Proc. Natl. Acad. Sci. U.S.A.* **2009**, *106*, 18474–18478.

(86) Ribbe, M.W.; Hu, Y.; Guo, M.; Schmid, B.; Burgess, B.K. The FeMoco-deficient MoFe protein produced by a *nifH* deletion strain of *Azotobacter vinelandii* shows unusual P-cluster features. *J. Biol. Chem.* **2002**, *277*, 23469–23476.

(87) Peters, J.W.; Stowell, M.H.B.; Soltis, S.M.; Finnegan, M.G.; Johnson, M.K.; Rees, D.C. Redox-dependent structural changes in the nitrogenase P-cluster. *Biochemistry* **1997**, *36*, 1181–1187.

(88) Kang, W.; Lee, C.C.; Jasniewski, A.J.; Ribbe, M.W.; Hu, Y. Structural evidence for a dynamic metallocofactor during N_2 reduction by Mo-nitrogenase. *Science* **2020**, *368*, 1381–1385.

(89) Lee, C.C.; Kang, W.; Jasniewski, A.J.; Stiebritz, M.T.; Tanifuji, K.; Ribbe, M.W.; Hu, Y. Evidence of substrate binding and product release via belt-sulfur mobilization of the nitrogenase cofactor. *Nat. Catal.* **2022**, *5*, 443–454.

(90) Surerus, K.K.; Hendrich, M.P.; Christie, P.D.; Rottgardt, D.; Orme-Johnson, W.H.; Munck, E. Möessbauer and integer-spin EPR of the oxidized P-clusters of nitrogenase: P^{ox} Is a non-Kramers system with a nearly degenerate ground doublet. *J. Am. Chem. Soc.* **1992**, *114*, 8579−8590.

(91) Lanzilotta, W.N.; Christiansen, J.; Dean, D.R.; Seefeldt, L.C. Evidence for coupled electron and proton transfer in the [8Fe-7S] cluster of nitrogenase. *Biochemistry* **1998**, *37*, 11376−11384.

(92) Keable, S.M.; Zadvornyy, O.A.; Johnson, L.E; Ginovska, B.; Rasmussen, A.J.; Danyal, K.; Eilers, B.J.; Prussia, G.A.; LeVan, A.X.; Raugei, S. *et al.* Structural characterization of the P^{1+} intermediate state of the P-cluster of nitrogenase. *J. Biol. Chem.* **2018**, *293*, 9629−9635.

(93) Rupnik, K.; Hu, Y.; Lee, C.C.; Wiig, J.A.; Ribbe, M.W.; Hales, B.J. P^+ state of nitrogenase P-cluster exhibits electronic structure of a $[Fe_4S_4]^+$ cluster. *J. Am. Chem. Soc.* **2012**, *134*, 13749−13754.

(94) Mayer, S.M.; Lawson, D.M.; Gormal, C.A.; Roe, S.M.; Smith, B.E. New insights into structure-function relationships in nitrogenase: A 1.6 Å resolution X-ray crystallographic study of *Klebsiella pneumoniae* MoFe-protein. *J. Mol. Biol.* **1999**, *292*, 871−891.

(95) Morgan, T.V.; Mortenson, L.E.; McDonald, J.W.; Watt, G.D. Comparison of redox and EPR properties of the molybdenum iron proteins of *Clostridium pasteurianum* and *Azotobacter vinelandii* nitrogenases. *J. Inorg. Biochem.* **1988**, *33*, 111−120.

(96) Ribbe, M.W.; Hu, Y.; Hodgson, K.O.; Hedman, B. Biosynthesis of nitrogenase metalloclusters. *Chem. Rev.* **2014**, *114*, 4063−4080.

(97) Orme-Johnson, W.H.; Hamilton, W.D.; Jones, T.L.; Tso, M.Y.W.; Burris, R.H.; Shah, V.K.; Brill, W.J. Electron paramagnetic resonance of nitrogenase and nitrogenase components from *Clostridium pasteurianum* W5 and *Azotobacter vinelandii* Op. *Proc. Natl. Acad. Sci. U.S.A.* **1972**, *69*, 3142−3145.

(98) Smith, B.E.; Lowe, D.J.; Bray, R.C. Studies by electron paramagnetic resonance on the catalytic mechanism of nitrogenase of *Klebsiella pneumoniae. Biochem. J.* **1973**, *135*, 331−341.

(99) Siemann, S.; Schneider, K.; Dröttboom, M.; Müller, A. The Fe-only nitrogenase and the Mo nitrogenase from *Rhodobacter capsulatus. Eur. J. Biochem.* **2002**, *269*, 1650−1661.

(100) Watt, G.D.; Burns, A.; Lough, S.; Tennent, D.L. Redox and spectroscopic properties of oxidized MoFe protein from *Azotobacter vinelandii. Biochemistry* **1980**, *19*, 4926−4932.

(101) Watt, G.D.; Burns, A.; Tennent, D.L. Stoichiometry and spectral properties of the molybdenum-iron (MoFe) cofactor and noncofactor redox centers in the molybdenum-iron (MoFe) protein of nitrogenase from *Azotobacter vinelandii. Biochemistry* **1981**, *20*, 7272−7277.

(102) Lough, S.; Burns, A.; Watt, G.D. Redox reactions of the nitrogenase complex from *Azotobacter vinelandii. Biochemistry* **1983**, *22*, 4062−4066.

(103) Schultz, F.A.; Gheller, S.F.; Burgess, B.K.; Lough, S.; Newton, W.E. Electrochemical characterization of the iron-molybdenum cofactor from *Azotobacter vinelandii* nitrogenase. *J. Am. Chem. Soc.* **1985**, *107*, 5364−5368.

(104) Pickett, C.J.; Vincent, K.A.; Ibrahim, S.K.; Gormal, C.A.; Smith, B.E.; Fairhurst, S.A.; Best, S.P. Synergic binding of carbon monoxide and cyanide to the FeMo cofactor of nitrogenase: relic chemistry of an ancient enzyme? *Chemistry* **2004**, *10*, 4770−4776.

(105) Lydon, B.R.; Lee, C.C.; Tanifuji, K.; Sickerman, N.S.; Newcomb, M.P.; Hu, Y.; Ribbe, M.W.; Yang, J.Y. Electrochemical characterization of isolated nitrogenase cofactors from *Azotobacter vinelandii*. *Chembiochem* **2020**, *21*, 1773−1778.

(106) Rawlings, J.; Shah, V.K.; Chisnell, J.R.; Brill, W.J.; Zimmermann, R.; Münck, E.; Orme-Johnson, W.H. Novel metal cluster in the iron-molybdenum cofactor of nitrogenase. Spectroscopic evidence. *J. Biol. Chem.* **1978**, *253*, 1001−1004.

(107) Burgess, B.K. The iron-molybdenum cofactor of nitrogenase. *Chem. Rev.* **1990**, *90*, 1377−1406.

(108) Tezcan, F.A.; Kaiser, J.T.; Howard, J.B.; Rees, D.C. Structural evidence for asymmetrical nucleotide interactions in nitrogenase. *J. Am. Chem. Soc.* **2015**, *137*, 146−149.

(109) Tezcan, F.A.; Kaiser, J.T.; Mustafi, D.; Walton, M.Y.; Howard, J.B.; Rees, D.C. Nitrogenase complexes: multiple docking sites for a nucleotide switch protein. *Science* **2005**, *309*, 1377−1380.

(110) Rutledge, H.L.; Cook, B.D.; Nguyen, H.P.M.; Herzik, M.A. Jr.; Tezcan, F.A. Structures of the nitrogenase complex prepared under catalytic turnover conditions. *Science* **2022**, 377, 865−869.

(111) Hoffman, B.M.; Lukoyanov, D.; Yang, Z.Y.; Dean, D.R.; Seefeldt, L.C. Mechanism of nitrogen fixation by nitrogenase: the next stage. *Chem. Rev.* **2014**, *114*, 4041−4062.

(112) Rohde, M.; Sippel, D.; Trncik, C.; Andrade, S.L.A.; Einsle, O. The critical E4 state of nitrogenase catalysis. *Biochemistry* **2018**, *57*, 5497−5504.

(113) Lowe, D.J.; Thorneley, R.N. The mechanism of *Klebsiella pneumoniae* nitrogenase action. Pre-steady-state kinetics of H_2 formation. *Biochem. J.* **1984**, *224*, 877-886.

(114) Thorneley, R.N.; Lowe, D.J. The mechanism of *Klebsiella pneumoniae* nitrogenase action. Pre-steady-state kinetics of an enzyme-bound intermediate in N_2 reduction and of NH_3 formation. *Biochem. J.* **1984**, *224*, 887−894.

(115) Lowe, D.J.; Thorneley, R.N. The mechanism of *Klebsiella pneumoniae* nitrogenase action. The determination of rate constants required for the simulation of the kinetics of N_2 reduction and H_2 evolution. *Biochem. J.* **1984**, *224*, 895−901.

(116) Thorneley, R.N.; Lowe, D.J. The mechanism of *Klebsiella pneumoniae* nitrogenase action. Simulation of the dependences of H_2-evolution rate on component-protein concentration and ratio and sodium dithionite concentration. *Biochem. J.* **1984**, *224*, 903−909.

(117) Lukoyanov, D.; Khadka, N.; Yang, Z-Y.; Dean, D.R.; Seefeldt, L.C.; Hoffman, B.M. Reductive elimination of H_2 activates nitrogenase to reduce the N≡N triple bond: characterization of the E4(4H) Janus intermediate in wild-type enzyme. *J. Am. Chem. Soc.* **2016**, *138*, 10674−10683.

(118) Seefeldt, L.C.; Yang, Z.Y.; Lukoyanov, D.A.; Harris, D.F.; Dean, D.R.; Raugei, S.; Hoffman, B.M. Reduction of substrates by nitrogenases. *Chem. Rev.* **2020**, *120*, 5082−5106.

(119) Raugei, S.; Seefeldt, L.C.; Hoffman, B.M. Critical computational analysis illuminates the reductive-elimination mechanism that activates nitrogenase for N_2 reduction. *Proc. Natl. Acad. Sci. U.S.A.* **2018**, *115*, E10521−E10530.

(120) Buscagan, T.M.; Perez, K.A.; Maggiolo, A.O.; Rees, D.C.; Spatzal, T. Structural characterization of two CO molecules bound to the nitrogenase active site. *Angew. Chem. Int. Ed. Engl.* **2021**, *60*, 5704−5707.

(121) Spatzal, T.; Perez, K.A.; Einsle, O.; Howard, J.B.; Rees, D.C. Ligand binding to the FeMo-cofactor: structures of CO-bound and reactivated nitrogenase. *Science* **2014**, *345*, 1620−1623.

(122) Rohde, M.; Laun, K.; Zebger, I.; Stripp, S.T.; Einsle, O. Two ligand-binding sites in CO-reducing V nitrogenase reveal a general mechanistic principle. *Sci. Adv.* **2021**, *7*, eabg4474.

(123) Rohde, M.; Grunau, K.; Einsle, O. CO binding to the FeV cofactor of CO-reducing vanadium nitrogenase at atomic resolution. *Angew. Chem. Int. Ed. Engl.* **2020**, *59*, 23626−23630.

(124) Spatzal, T.; Perez, K.A.; Howard, J.B.; Rees, D.C. Catalysis-dependent selenium incorporation and migration in the nitrogenase active site iron-molybdenum cofactor. *Elife* **2015**, *4*, e11620.

(125) Wei, W.J.; Siegbahn, P.E.M. A mechanism for nitrogenase including loss of a sulfide. *Chemistry* **2022**, *28*, e202103745.

(126) Rohde, M.; Trncik, C.; Sippel, D.; Gerhardt, S.; Einsle, O. Crystal structure of VnfH, the iron protein component of vanadium nitrogenase. *J. Biol. Inorg. Chem.* **2018**, *23*, 1049−1056.

(127) Blank, M.A.; Lee, C.C.; Hu, Y.; Hodgson, K.O.; Hedman, B.; Ribbe, M.W. Structural models of the $[Fe_4S_4]$ clusters of homologous nitrogenase Fe proteins. *Inorg. Chem.* **2011**, *50*, 7123−7128.

(128) Eady, R.R.; Richardson, T.H.; Miller, R.W.; Hawkins, M.; Lowe, D.J. The vanadium nitrogenase of *Azotobacter chroococcum*. Purification and properties of the Fe protein. *Biochem. J.* **1988**, *256*, 189−196.

(129) Lindahl, P.A.; Gorelick, N.J.; Münck, E.; Orme-Johnson, W.H. EPR and Mössbauer studies of nucleotide-bound nitrogenase iron protein from *Azotobacter vinelandii. J. Biol. Chem.* **1987**, *262*, 14945−14953.

(130) Blanchard, C.Z.; Hales, B.J. Isolation of two forms of the nitrogenase VFe protein from *Azotobacter vinelandii. Biochemistry* **1996**, *35*, 472−478.

(131) Lee, C.C.; Hu, Y.; Ribbe, M.W. Unique features of the nitrogenase VFe protein from *Azotobacter vinelandii. Proc. Natl. Acad. Sci. U.S.A.* **2009**, *106*, 9209−9214.

(132) Sippel, D.; Einsle, O. The structure of vanadium nitrogenase reveals an unusual bridging ligand. *Nat. Chem. Biol.* **2017**, *13*, 956−960.

(133) Eady, R.R.; Robson, R.L.; Richardson, T.H.; Miller, R.W.; Hawkins, M. The vanadium nitrogenase of *Azotobacter chroococcum.* Purification and properties of the VFe protein. *Biochem. J.* **1987**, *244*, 197−207.

(134) Morningstar, J.E.; Hales, B.J. Electron paramagnetic resonance study of the vanadium-iron protein of nitrogenase from *Azotobacter vinelandii. J. Am. Chem. Soc.* **1987**, *109*, 6854−6855.

(135) Tittsworth, R.C.; Hales, B.J. Oxidative titration of the nitrogenase VFe protein from *Azotobacter vinelandii*: an Example of redox-gated electron flow. *Biochemistry* **1996**, *35*, 479−487.

(136) Ravi, N.; Moore, V.; Lloyd, S.G.; Hales, B.J.; Huynh, B.H. Mössbauer characterization of the metal clusters in *Azotobacter vinelandii* nitrogenase VFe protein. *J. Biol. Chem.* **1994**, *269*, 20920−20924.

(137) Hu, Y.; Corbett, M.C.; Fay, A.W.; Webber, J.A.; Hedman, B.; Hodgson, K.O.; Ribbe, M.W. Nitrogenase eeactivity with P-cluster variants. *Proc. Natl. Acad. Sci. U. S. A.* **2005**, *102*, 13825−13830.

(138) Newcomb, M.P.; Lee, C.C.; Tanifuji, K.; Jasniewski, A.J.; Liedtke, J.; Ribbe, M.W.; Hu, Y. A V-nitrogenase variant containing a citrate-substituted cofactor. *Chembiochem* **2020**, *21*, 1742−1748.

(139) Tittsworth, R.C.; Hales, B.J. Detection of EPR signals assigned to the 1-equiv-oxidized P-clusters of the nitrogenase MoFe-protein from *Azotobacter vinelandii. J. Am. Chem. Soc.* **1993**, *115*, 9763−9767.

(140) Eady, R.R. Current status of structure function relationships of vanadium nitrogenase. *Coord. Chem. Rev.* **2003**, *237*, 23–30.

(141) Smith, B.E.; Eady, R.R.; Lowe, D.J.; Gormal, C. The vanadium-iron protein of vanadium nitrogenase from *Azotobacter chroococcum* contains an iron-vanadium cofactor. *Biochem. J.* **1988**, *250*, 299−302.

(142) Harvey, I.; Arber, J.M.; Eady, R.R.; Smith, B.E.; Garner, C.D.; Hasnain, S.S. Iron K-edge X-ray-absorption spectroscopy of the iron-vanadium cofactor of the vanadium nitrogenase from *Azotobacter chroococcum. Biochem. J.* **1990**, *266*, 929−931.

(143) Fay, A.W.; Blank, M.A.; Lee, C.C.; Hu, Y.; Hodgson, K.O.; Hedman, B.; Ribbe, M.W. Characterization of isolated nitrogenase FeVco. *J. Am. Chem. Soc.* **2010**, *132*, 12612−12618.

(144) Chen, J.; Christiansen, J.; Tittsworth, R.C.; Hales, B.J.; George, S.J.; Coucouvanis, D.; Cramer, S.P. Iron EXAFS of *Azotobacter vinelandii* nitrogenase molybdenum-iron and vanadium-iron proteins. *J. Am. Chem. Soc.* **1993**, *115*, 5509−5515.

(145) Trncik, C.; Müller, T.; Franke, P.; Einsle, O. Structural analysis of the reductase component AnfH of iron-only nitrogenase from *Azotobacter vinelandii. J. Inorg. Biochem.* **2022**, *227*, 111690.

(146) Schneider, K.; Gollan, U.; Dröttboom, M.; Selsemeier-Voigt, S.; Müller, A. Comparative biochemical characterization of the iron-only nitrogenase and the molybdenum nitrogenase from *Rhodobacter capsulatus. Eur. J. Biochem.* **1997**, *244*, 789−800.

(147) Harris, D.F.; Lukoyanov, D.A.; Shaw, S.; Compton, P.; Tokmina-Lukaszewska, M.; Bothner, B.; Kelleher, N.; Dean, D.R.; Hoffman, B.M.; Seefeldt, L.C. Mechanism of N_2 reduction catalyzed by Fe-nitrogenase involves reductive elimination of H_2. *Biochemistry* **2018**, *57*, 701−710.

(148) Krahn, E.; Weiss, B.; Kröckel, M.; Groppe, J.; Henkel, G.; Cramer, S.; Trautwein, A.; Schneider, K.; Müller, A. The Fe-only nitrogenase from *Rhodobacter capsulatus*: identification of the cofactor, an unusual, high-nuclearity iron-sulfur cluster, by Fe K-edge EXAFS and ^{57}Fe Mössbauer spectroscopy. *J. Biol. Inorg. Chem.* **2002**, *7*, 37−45.

(149) Müller, A.; Schneider, K.; Knüttel, K.; Hagen, W.R. EPR spectroscopic characterization of an 'iron only' nitrogenase. $S = 3/2$ spectrum of component 1 isolated from *Rhodobacter capsulatus*. *FEBS Lett.* **1992**, *303*, 36−40.

(150) Rebelein, J.G.; Lee, C.C.; Newcomb, M.; Hu, Y.; Ribbe, M.W. Characterization of an M-cluster-substituted nitrogenase VFe protein. *mBio* **2018**, *9*, e00310−18.

(151) Lee, C.C.; Tanifuji, K.; Newcomb, M.; Liedtke, J.; Hu, Y.; Ribbe, M.W. A comparative analysis of the CO-eeducing activities of MoFe proteins containing Mo- and V-nitrogenase cofactors. *Chembiochem* **2018**, *1*, 649−653.

(152) Liedtke, J.; Lee, C.C.; Tanifuji, K.; Jasniewski, A.J.; Ribbe, M.W.; Hu, Y. Characterization of a Mo-nitrogenase variant containing a citrate-substituted cofactor. *Chembiochem* **2021**, *22*, 151−155.

(153) Yang, Z.Y.; Dean, D.R.; Seefeldt, L.C. Molybdenum nitrogenase catalyzes the reduction and coupling of CO to form hydrocarbons. *J. Biol. Chem.* **2011**, *286*, 19417−19421.

(154) Rebelein, J.G.; Hu, Y.; Ribbe, M.W. Differential reduction of CO_2 by molybdenum and vanadium nitrogenases. *Angew. Chem. Int. Ed. Engl.* **2014**, *53*, 11543−11546.

(155) Seefeldt, L.C.; Rasche, M.E.; Ensign, S.A. Carbonyl sulfide and carbon dioxide as new substrates, and carbon disulfide as a new inhibitor, of nitrogenase. *Biochemistry* **1995**, *34*, 5382−5389.

(156) Hu, B.; Harris, D.F.; Dean, D.R.; Liu, T.L.; Yang, Z.-Y.; Seefeldt, L.C. Electrocatalytic CO_2 reduction catalyzed by nitrogenase MoFe and FeFe proteins. *Bioelectrochemistry* **2018**, *120*, 104−109.

(157) Tanifuji, K.; Lee, C.C.; Ohki, Y.; Tatsumi, K.; Hu, Y.; Ribbe, M.W. Combining a nitrogenase scaffold and a synthetic compound into an artificial enzyme. *Angew. Chem. Int. Ed. Engl.* **2015**, *54*, 14022−14025.

(158) Tanifuji, K.; Jasniewski, A.J.; Lee, C.C.; Solomon, J.B.; Nagasawa, T.; Ohki, Y.; Tatsumi, K.; Hedman, B.; Hodgson, K.O.; Hu, Y. *et al.* Incorporation of an asymmetric Mo-Fe-S cluster as an artificial cofactor into nitrogenase. *Chembiochem* **2022**, Aug 4:e202200384.

(159) Shah, V.K.; Brill, W.J. Isolation of an iron-molybdenum cofactor from nitrogenase. *Proc. Natl. Acad. Sci. U. S. A.* **1977**, *74*, 3249−3253.

(160) Fay, A.W.; Lee, C.C.; Wiig, J.A.; Hu, Y.; Ribbe, M.W. In Nitrogen Fixation: Methods and Protocols; Ribbe, M.W., Ed.; Humana Press: Totowa, NJ, 2011; pp 239−248.

(161) Fay, A.W.; Blank, M.A.; Lee, C.C.; Hu, Y.; Hodgson, K.O.; Hedman, B.; Ribbe, M.W. Spectroscopic characterization of the isolated iron-molybdenum cofactor (FeMoco) precursor from the protein NifEN. *Angew. Chem. Int. Ed. Engl.* **2011**, *50*, 7787-7790.

(162) Tanifuji, K.; Sickerman, N.; Lee, C.C.; Nagasawa, T.; Miyazaki, K.; Ohki, Y.; Tatsumi, K.; Hu, Y.; Ribbe, M.W. Structure and reactivity of an asymmetric synthetic mimic of nitrogenase cofactor. *Angew. Chem. Int. Ed. Engl.* **2016**, *55*, 15633−15636.

(163) Sickerman, N.S.; Tanifuji, K.; Lee, C.C.; Ohki, Y.; Tatsumi, K.; Ribbe, M.W.; Hu, Y. Reduction of C_1 substrates to hydrocarbons by the homometallic precursor and synthetic mimic of the nitrogenase cofactor. *J. Am. Chem. Soc.* **2017**, *139*, 603−

(164) Lee, C.C.; Hu, Y.; Ribbe, M.W. Reduction and condensation of aldehydes by the isolated cofactor of nitrogenase. *ACS Cent. Sci.* **2018**, *4*, 1430−1435.

(165) Davis, L.C.; Henzl, M.T.; Burris, R.H.; Orme-Johnson, W.H. Iron-sulfur clusters in the molybdenum-iron protein component of nitrogenase. Electron paramagnetic resonance of the carbon monoxide inhibited state. *Biochemistry* **1979**, *18*, 4860−4869.

(166) Maskos, Z.; Hales, B.J. Photo-lability of CO bound to Mo-nitrogenase from *Azotobacter vinelandii*. *J. Inorg. Biochem.* **2003**, *93*, 11−17.

(167) Pollock, R.C.; Lee, H.-I.; Cameron, L.M.; DeRose, V.J.; Hales, B.J.; Orme-Johnson, W.H.; Hoffman, B.M. Investigation of CO bound to inhibited forms of nitrogenase MoFe protein by ^{13}C ENDOR. *J. Am. Chem. Soc.* **1995**, *117*, 8686−8687.

(168) Christie, P.D.; Lee, H.-I.; Cameron, L.M.; Hales, B.J.; OrmeJohnson, W.H.; Hoffman, B.M. Identification of the CO-binding cluster in nitrogenase MoFe protein by ENDOR of ^{57}Fe isotopomers. *J. Am. Chem. Soc.* **1996**, *118*, 8707−8709.

(169) Lee, H.-I.; Cameron, L.M.; Hales, B.J.; Hoffman, B.M. CO binding to the FeMo cofactor of CO-inhibited nitrogenase: ^{13}CO and ^{1}H Q-band ENDOR investigation. *J. Am. Chem. Soc.* **1997**, *119*, 10121−10126.

(170) George, S.J.; Ashby, G.A.; Wharton, C.W.; Thorneley, R.N.F. Time-resolved binding of carbon monoxide to nitrogenase monitored by stopped-flow infrared spectroscopy. *J. Am. Chem. Soc.* **1997**, *119*, 6450−6451.

(171) Yan, L.; Pelmenschikov, V.; Dapper, C.H.; Scott, A.D.; Newton, W.E.; Cramer, S.P. IR-monitored photolysis of CO-inhibited nitrogenase: a major EPR-silent species with coupled terminal CO ligands. *Chemistry* **2012**, *18*, 16349−16357.

(172) Yang, Z.-Y.; Seefeldt, L.C.; Dean, D.R.; Cramer, S.P.; George, S.J. Steric control of the hi-CO MoFe nitrogenase complex revealed by stopped-low infrared spectroscopy. *Angew. Chem. Int. Ed.* **2011**, *50*, 272−275.

(173) Yan, L.; Dapper, C.H.; George, S.J.; Wang, H.; Mitra, D.; Dong, W.; Newton, W.E.; Cramer, S.P. Photolysis of hi-CO nitrogenase − observation of a plethora of distinct CO species using infrared spectroscopy. *Eur. J. Inorg. Chem.* **2011**, *2011*, 2064−2074.

(174) Lee, C.C.; Fay, A.W.; Weng, T.-C.; Krest, C.M.; Hedman, B.; Hodgson, K.O.; Hu, Y.; Ribbe, M.W. Uncoupling binding of substrate CO from turnover by vanadium nitrogenase. *Proc. Natl. Acad. Sci. U.S. A.* **2015**, *112*, 13845−13849.

(175) Lee, C.C.; Wilcoxen, J.; Hiller, C.J.; Britt, R.D.; Hu, Y. Evaluation of the catalytic relevance of the CO-bound states of V-nitrogenase. *Angew. Chem., Int. Ed.* **2018**, *57*, 3411−3414.

(176) Hiller, C.J.; Lee, C.C.; Stiebritz, M.T.; Rettberg, L.A.; Hu, Y. Strategies towards capturing nitrogenase substrates and intermediates via controlled alteration of electron fluxes. *Chemistry* **2019**, *25*, 2389−2395.

(177) Milton, R.D. Nitrogenase loosens its belt to fix dinitrogen. *Nat. Catal.* **2022**, *5*, 361–362.

(178) Varley, J.B.; Wang, Y.; Chan, K.; Studt, F.; Nørskov, J.K. Mechanistic insights into nitrogen fixation by nitrogenase enzymes. *Phys. Chem. Chem. Phys.* **2015**, *17*, 29541−29547.

(179) Sippel, D.; Rohde, M.; Netzer, J.; Trncik, C.; Gies, J.; Grunau, K.; Djurdjevic, I.; Decamps, L.; Andrade, S.L.A.; Einsle, O. A bound reaction intermediate sheds light on the mechanism of nitrogenase. *Science* **2018**, *359*, 1484−1489.

(180) Dance, I. The chemical mechanism of nitrogenase: calculated details of the intramolecular mechanism for hydrogenation of η_2-N_2 on FeMo-co to NH_3. *Dalton Trans.* **2008**, *43*, 5977−5991.

(181) Dance, I. The chemical mechanism of nitrogenase: hydrogen tunneling and further aspects of the intramolecular mechanism for hydrogenation of η_2-N_2 on FeMo-co to NH_3. *Dalton Trans.* **2008**, *43*, 5992−5998.

(182) Durrant, M.C.; Francis, A.; Lowe, D.J.; Newton, W.E.; Fisher, K. Evidence for a dynamic role for homocitrate during nitrogen fixation: the effect of substitution at the alpha-Lys426 position in MoFe-protein of *Azotobacter vinelandii. Biochem. J.* **2006**, *397*, 261−270.

(183) Jensen, B.B.; Burris, R.H. Effect of high pN_2 and high pD_2 on NH_3 production, H_2 evolution, and HD formation by nitrogenases. *Biochemistry* **1985**, *24*, 1141–1147.

(184) Li, J.L.; Burris, R.H. Infuence of pN_2 and pD_2 on HD formation by various nitrogenases. *Biochemistry* **1983**, *22*, 4472–4480.

(185) Burgess, B.K.; Wherland, S.; Newton, W.E.; Stiefel, E.I. Nitrogenase reactivity: insight into the nitrogen-fixing process through hydrogen inhibition and HD-forming reactions. *Biochemistry* **1981**, *20*, 5140–5146.

(186) Wherland, S.; Burgess, B.K.; Stiefel, E.I.; Newton, W.E. Nitrogenase reactivity: effects of component ratio on electron flow and distribution during nitrogen fixation. *Biochemistry* **1981**, *20*, 5132–5140.

(187) Yang, Z.-Y.; Khadka, N.; Lukoyanov, D.; Hoffman, B.M.; Dean, D.R.; Seefeldt, L.C. On reversible H_2 loss upon N_2 binding to FeMo-cofactor of nitrogenase. *Proc. Natl. Acad. Sci. U. S. A.* **2013**, *110*, 16327–16332.

(188) Dance, I. How does vanadium nitrogenase reduce CO to hydrocarbons? *Dalton Trans.* **2011**, *40*, 5516−5527.

(189) Varley, J.B.; Nørskov, J.K. First-principles calculations of Fischer−Tropsch processes catalyzed by nitrogenase enzymes. *ChemCatChem* **2013**, *5*, 732−736.

(190) Rettberg, L.A.; Stiebritz, M.T.; Kang, W.; Lee, C.C.; Ribbe, M.W.; Hu, Y. Structural and mechanistic insights into CO_2 activation by nitrogenase iron protein. *Chemistry* **2019**, *25*, 13078−13082.

(191) Rettberg, L.A.; Kang, W.; Stiebritz, M.T.; Hiller, C.J.; Lee, C.C.; Liedtke, J.; Ribbe, M.W.; Hu, Y. Structural analysis of a nitrogenase iron protein from *Methanosarcina acetivorans*: implications for CO_2 capture by a surface-exposed $[Fe_4S_4]$ cluster. *mBio* **2019**, *10*, e01497−19.

(192) Locher, K.P.; Hans, M.; Yeh, A.P.; Schmid, B.; Buckel, W.; Rees, D.C. Crystal structure of the *Acidaminococcus fermentans* 2-hydroxyglutaryl-CoA dehydratase component A. *J. Mol. Biol.* **2001**, *307*, 297−308.

(193) Knauer, S.H.; Buckel, W.; Dobbek, H. On the ATP-dependent activation of the radical enzyme (*R*)-2-hydroxyisocaproyl-CoA dehydratase. *Biochemistry* **2012**, *51*, 6609−

(194) Hans, M.; Buckel, W.; Bill, E. Spectroscopic evidence for an all-ferrous $[4Fe\text{-}4S]^0$ cluster in the superreduced activator of 2-hydroxyglutaryl-CoA dehydratase from *Acidaminococcus fermentans. J. Biol. Inorg. Chem.* **2008**, *13*, 563−5 74.

(195) Nordlund, S.; Hçgbom, M. ADP-ribosylation, a mechanism regulating nitrogenase activity. *FEBS J.* **2013**, *280*, 3484−3490.

(196) Kasting, J.F. Earth's early atmosphere. *Science* **1993**, *259*, 920–926.

(197) Lammer, H.; Zerkle, A.L.; Gebauer, S.; Tosi, N.; Noack, L.; Scherf, M.; Pilat-Lohinger, E.; Güdel, M.; Grenfell, J.L.; Godolt, M. *et al.* Origin and evolution of the atmospheres of early Venus, Earth and Mars. *Astron. Astrophys. Rev.* **2018**, *26*, 1–72.

(198) Matamoros-Veloza, A.; Cespedes, O.; Johnson, B.R.G.; Stawski, T.M.; Terranova, U.; de Leeuw, N.H.; Benning, L.G.A. Highly reactive precursor in the iron sulfide system. *Nat. Commun.* **2018**, *9*, 3125.

(199) Wolthers, M.; van der Gaast, S.J.; Rickard, D. The structure of disordered mackinawite. *Am. Min.* **2003**, *88*, 2007–2015.

(200) Rickard, D.; Luther, G.W. Chemistry of iron sulfides. *Chem. Rev.* **2007**, *107*, 514–562.

(201) Lennie, A.R.; Redfern, S.A.T.; Schofield, P.F.; Vaughan, D.J. Synthesis and Rietveld crystal structure refinement of mackinawite, tetragonal FeS. *Mineral. Mag.* **1995**, *59*, 677–683.

(202) Mullet, M.; Boursiquot, S.; Abdelmoula, M.; Génin, J.M.; Ehrhardt, J.J. Surface chemistry and structural properties of mackinawite prepared by reaction of sulfide ions with metallic iron. *Geochim. Cosmochim. Acta* **2002**, *66*, 829–836.

(203) Russell, M.J.; Martin, W. The rocky roots of the acetyl-CoA pathway. *Trends Biochem. Sci.* **2004**, *29*, 358–363.

(204) Ferris, J.P.; Aubrey, R.H.J.; Liu, R.; Orgel, L.E. Synthesis of long prebiotic oligomers on mineral surfaces. *Nature* **1996**, *381*, 59–61.

(205) Santos-Carballal, D.; Roldan, A.; Dzade, N.Y.; de Leeuw, N.H. Reactivity of CO_2 on the surfaces of magnetite (Fe_3O_4), greigite (Fe_3S_4) and mackinawite (FeS). *Phil. Trans. R. Soc. A* **2017**, *376*, 20170065.

(206) Mirabella, F.; Zaki, E.; Ivars-Barcelo, F.; Schauermann, S.; Shaikhutdinov, S.; Freund, H.J. CO_2 adsorption on magnetite Fe_3O_4(111). *J. Phys. Chem. C* **2018**, *122*, 27433–27441.

(207) Tamaura, Y.; Tabata, M. Complete reduction of carbon dioxide to carbon using cation-excess magnetite. *Nature* **1990**, *346*, 255–256.

(208) Wächtershäuser, G. The case for the chemoautotrophic origin of life in an iron-sulfur world. *Orig. Life Evol. Biosph.* **1990**, *20*, 173–176.

(209) Drobner, E.; Huber, H.; Wächtershäuser, G.; Rose, D.; Stetter, K.O. Pyrite formation linked with hydrogen evolution under anaerobic conditions. *Nature* **1990**, *346*, 742–744.

(210) Wächtershäuser, G. Before enzymes and templates: theory of surface metabolism. *Microbiol. Rev.* **1988**, *52*, 452–484.

(211) Blochl, E.; Keller, M.; Wächtershäuser, G.; Stetter, K.O. Reactions depending on iron sulfide and linking geochemistry with biochemistry. *Proc. Natl. Acad. Sci. U. S. A.* **1992**, *89*, 8117–8120.

(212) Dörr, M.; Käßbohrer, J.; Grunert, R.; Kreisel, G.; Brand, W.A.; Werner, R.A.; Geilmann, H.; Apfel, C.; Robl, C.; Weigand, W.A. Possible prebiotic formation of ammonia from dinitrogen on iron sulfide surfaces. *Angew. Chem. Int. Ed.* **2003**, *42*, 1540–1543.

(213) Heinen, W.; Lauwers, A.M. Organic sulfur compounds resulting from the interaction of iron sulfide, hydrogen sulfide and carbon dioxide in an anaerobic aqueous environment. *Orig. Life Evol. Biosph.* **1996**, *26*, 131–150.

(214) Hyun, S.P.; Kim, B.A.; Son, S.; Kwon, K.D.; Kim, E.; Hayes, K.F. Cadmium(II) removal by mackinawite under anoxic conditions. *ACS Earth Space Chem.* **2021**, *5*, 1306–1315.

(215) Coles, C.A.; Rao, S.R.; Yong, R.N. Lead and cadmium interactions with mackinawite: retention mechanisms and the role of pH. *Environ. Sci. Technol.* **2000**, *34*, 996–1000.

(216) Wolthers, M.; Charlet, L.; van der Weijden, C.H.; van der Linde, P.R.; Rickard, D. Arsenic mobility in the ambient sulfidic environment: Sorption of arsenic(V) and arsenic(III) onto disordered mackinawite. *Geochim. Cosmochim. Acta* **2005**, *69*, 3483–3492.

(217) Farquhar, M.L.; Charnock, J.M.; Livens, F.R.; Vaughan, D.J. Mechanisms of arsenic uptake from aqueous solution by interaction with goethite, lepidocrocite, mackinawite, and pyrite: an X-ray absorption spectroscopy study. *Environ. Sci. Technol.* **2002**, *36*, 1757–1762.

(218) Mullet, M.; Boursiquot, S.; Ehrhardt, J.J. Removal of hexavalent chromium from solutions by mackinawite, tetragonal FeS. *Colloids Surf. A Physicochem. Eng. Asp.* **2004**, *244*, 77–85.

(219) Hatton, B.; Rickard, D. Nucleic acids bind to nanoparticulate iron (II) monosulphide in aqueous solutions. *Orig. Life Evol. Biosph.* **2008**, 38, 257–270.

(220) Waldrop, M.M. Goodbye to the warm little pond? *Science* **1990**, *250*, 1078–1080.

(221) Martin, W.; Baross, J.; Kelley, D.; Russell, M.J. Hydrothermal vents and the origin of life. *Nat. Rev. Microbiol.* **2008**, *6*, 805–814.

(222) Huber, C.; Wächtershäuser, G. Activated acetic acid by carbon fixation on (Fe,Ni)S under primordial conditions. *Science* **1997**, *276*, 245–247.

(223) Pearce, B.K.D.; Pudritz, R.E.; Semenov, D.A.; Henning, T.K. Origin of the RNA world: The fate of nucleobases in warm little ponds. *Proc. Natl. Acad. Sci. U. S. A.* **2017**, *114*, 11327–11332.

(224) Miller, S.L.; Urey, H.C. Organic compound synthesis on the primitive Earth. *Science* **1959**, *130*, 245–251.

(225) Oro, J. Synthesis of adenine from ammonium cyanide. *Biochem. Biophys. Res. Commun.* **1960**, *2*, 407–412.

(226) Zahnle, K.J. Photochemistry of methane and the formation of hydrocyanic acid (HCN) in the Earth's early atmosphere. J. Geophys. Res. **1986**, *91*, 2819–2834.

(227) Chameides, W.L.; Walker, J.C.G. Rates of fixation by lightning of carbon and nitrogen in possible primitive atmospheres. *Orig. Life Evol. Biosph.* **1981**, *11*, 291–302.

(228) Ferus, M.; Kubelík, P.; Knížek, A.; Pastorek, A.; Sutherland, J.; Civiš, S. High energy radical chemistry formation of HCN-rich atmospheres on early Earth. *Sci. Rep.* **2017**, *7*, 6275.

(229) Todd, Z.R.; Öberg, K.I. Cometary delivery of hydrogen cyanide to the early Earth. *Astrobiology* **2020**, *20*, 1109–1120.

(230) Ritson, D.J.; Battilocchio, C.; Ley, S.V.; Sutherland, J.D. Mimicking the surface and prebiotic chemistry of early Earth using flow chemistry. *Nat. Commun.* **2018**, *9*, 1821.

(231) Patel, B.H.; Percivalle, C.; Ritson, D.J.; Duffy, C.D.; Sutherland, J.D. Common origins of RNA, protein and lipid precursors in a cyanosulfidic protometabolism. *Nat. Chem.* **2015**, *7*, 301–307.

(232) Rimmer, P.B.; Shorttle, O. Origin of life's building blocks in carbon-and nitrogen-rich surface hydrothermal vents. *Life* **2019**, *9*, 12.

(233) Bolney, R.; Grosch, M.; Winkler, M.; van Slageren, J.; Weigand, W.; Robl, C. Mackinawite formation from elemental iron and sulfur. *RSC Adv.* **2021**, *11*, 32464–32475.

(234) Grosch, M.; Stiebritz, M.T.; Bolney, R.; Winkler, M.; Jückstock, E.; Busch, H.; Peters, S.; Siegle, A.F.; van Slageren, J.; Ribbe, M. *et al.* Mackinawite-supported reduction of C_1 substrates into prebiotically relevant precursors. *ChemSystemsChem* **2022**, e202200010.

(235) Teichert, J.S.; Kruse, F.M.; Trapp, O. Direct prebiotic pathway to DNA nucleosides. *Angew. Chem. Int. Ed.* **2019**, *58*, 9944–9947.

(236) Dodd, M.S.; Papineau, D.; Grenne, T.; Slack, J. F.; Rittner, M.; Pirajno, F.; O'Neil, J.; Little, C.T.S. Evidence for early life in Earth's oldest hydrothermal vent precipitates. *Nature* **2017**, *543*, 60–64.

Table of Contents